UNIVERSITÀ DEGLI STUDI DI PADOVA

Dipartimento di Fisica e Astronomia "Galileo Galilei"

Master Degree in Physics

Final Dissertation

Angular momentum and shapes of rotating quantum droplets

Thesis supervisor

Prof. Francesco Ancilotto

Candidate

Matteo Caldara

Academic Year 2020/2021

Abstract

Self-bound quantum droplets, resulting from the balance between attractive and repulsive forces between their atomic components, appear in different physical scenarios, the prototypes being liquid droplets made of superfluid ^{4}He. Recently, a new kind of quantum droplets have been found using a bosonic mixture of ultracold atoms, whose stability results from the interplay between the interspecies attractive mean field energy and the repulsive term representing a beyond mean field correction due to quantum fluctuations. Being a mixture of Bose-Einstein condensates, quantum droplets are likely superfluid. Thus, when they are set into rotation, the angular momentum can only be stored in the form of quantized vortices and/or capillary waves. In the case of superfluid ^{4}He, the interplay between vortices and capillary waves results in droplet shapes surprisingly close to those of classical liquid droplets rotating with the same angular velocity. In the case of quantum droplets made of bosonic mixtures, such interplay remains to be uncovered. The scope of this thesis is to theoretically study the stability and appearance of rotating self-bound nanodroplets made of bosonic binary mixtures using numerical simulations based on Density Functional Theory, to unveil the interplay between the superfluid nature of the system and their shapes.

Acknowledgments

This thesis project marks the end of a very important part of my life, so I think it is the good moment to stop for a while and acknowledge those people who spent their time accompanying me in this journey.

It's been five years since I left my home and moved to Padova to start my studies in Physics. At that time I didn't know exactly what to expect, but now I am really proud of that choice: in fact, during this period I learnt a lot and I grew up as a person, for sure.

The Physics Department was a sort of second home where I spent most of my time among lectures, long study sessions in the library and several exams. I feel very glad and lucky to have met professors who love teaching and give all their best to share their knowledge and let the students deeply appreciate all the wonders that Physics can give. There are few people, however, that deserve a special acknowledgment for how much they gave me and for the way they did it.
Firstly, I would like to thank Prof. Marco Mazzocco for his constant presence throughout these years: everything started with C++ (the shock of the first lectures is still hurting ...) and, passing through the clever and precise supervision of my Bachelor's thesis, he was there also a couple of months ago when it was time for me to think of the PhD. Our physical roads divided at a certain point, but I am happy we can always rely on each other for a good chat or a pleasant call.
A special thank you also to Prof. Luca Dell'Anna for his kindness and availability when I had to decide about my future: his suggestions and his support were extremely important and guided me towards the final choice. By the way, he has the merit of having introduced me to the beauties of the *theoretical condensed matter physics* and, in particular, to the amazing world of ultracold atomic gases
I sincerely thank Prof. Francesco Ancilotto for his gentle guidance during the last six months. I was always let my time to try, make errors, think of how to solve problems and make hypothesis for the interpretation of our results: then, he was present for useful discussions and sharp suggestions that made me improve as a physicist. Despite all the limitations due to Covid-19, he always found the time and the way to help and support me, from the very first day to the last one. Actually, he was a guide during the last two years of the Master's Degree since he let me discover my interests and find my way in the world of Physics.

I had also the opportunity to make new friends, in particular I refer to Rugiada, Gloria and Andrea and our *Lista dei desideri*: we followed different roads, we were spread all over Europe, we faced a pandemic ... but it takes only a moment to organize a delightful breakfast or an enjoyable lunch to relax, chat, laugh and have fun together.
Since last year a new friendship has been developing, gaining a special and important place in my life. Thank you, Daniele, for always challenging me and pushing me to do my best. You are one of the strongest people I have ever known: even if the life brought you the hardest obstacle, the way you try to get over is a fantastic example for me.

I cannot absolutely forget my two best friends, directly from Grumello del Monte.
I would like to thank Daniele F. for listening to me (even when I start endless discussions about boring *Physics stuff* ...) and for remembering me to believe in myself: you always transmit me the necessary calm and serenity to overcome any obstacle.

Thank you, Daniele B., for stimulating my mind and my fantasy to project and organize new memorable adventures and experiences: you are a reference point, inspiring me to always do better.
We are very different, but we share a lot of passions and goals: no matter where the future will bring us, everyone will be present for the others.

I would not be here without my family who supports my choices, celebrates my successes, is always there in the difficulties and bears my (sometimes) lunatic character.
Thank you to my brother, Paolo, and my sister, Silvia, for making me laugh and for helping living my life with lightness.
Thank you to my mum, Chiara, and my dad, Giorgio, for letting me build and follow my own way, encouraging my decisions: you are my sources of inspiration and I am who I am now thanks to you.

Last, but not least, I would like to thank Sofia: you are always by my side, you make me feel special and you inspire me to improve day by day.

Contents

Introduction

The formation of self-bound droplets is a well-known macroscopic phenomenon appearing often in nature in various physical systems: the stability and shape of a droplet of an ordinary liquid depend on the balance of effective forces among its constituent particles. The interplay between attractive interactions, that keep the system together, and repulsive ones, that prevent it from collapse, defines the droplets' surface tension: this is the key ingredient that stabilizes the system in a metastable state. Such droplets do not exist only at the macroscopic level, but they are present in the *quantum realm*, too: atomic nuclei [1] and superfluid ^{4}He droplets [2–4] are two outstanding examples. Apart from these dense and strongly interacting many-body systems, recently a completely novel type of quantum liquid was theoretically predicted and then experimentally verified: self-bound quantum droplets inside weakly interacting ultra cold atomic gases. In his seminal work [5], D. Petrov predicted the formation of self-bound quantum droplets from a binary Bose-Einstein condensate in the presence of different inter- and intraspecies interactions: this is the case of homonuclear atomic mixtures, like two different hyperfine states of ^{39}K [6, 7], or heteronuclear bosonic mixtures, like ^{41}K-^{87}Rb [8]. In these systems, the physical mechanism of droplet formation is based on tuning the interspecies interaction, by means of Feshbach resonances, in order to remain only with a weak effective attraction between the two components. While this represents an unstable region in the mean field viewpoint, where the system would be led to a collapse, a crucial role is played by a correction to the mean field energy, known as Lee-Huang-Yang (LHY) correction [9], that has an intrinsic quantum nature. In particular, the quantum LHY repulsion balances the mean field attraction and stabilizes the system against collapse: the mixture can then exist as a droplet in equilibrium with vacuum without any external trapping. These quantum droplets can be large, containing thousands of atoms, and they are very dilute: their characteristic densities are more than 8 orders of magnitude lower than liquid helium.

Since these self-bound systems form out of a Bose-Einstein condensate, it is then reasonable to truly consider them as superfluids. One of the features of superfluidity are vortices, nontrivial topological defects consisting of a depletion of density associated to a phase shift: it is interesting to study the rotational properties of the aforementioned self-bound systems and look at how vorticity comes into play. When classical drops are set into rotation, their spherical shape undergoes large deformations, evolving from oblate to prolate and two-lobed, eventually fissioning in the case of a large enough rotational velocity [10]. Several experimental studies were performed on rotating superfluid ^{4}He droplets, revealing the presence of vortex lattices through coherent x-ray scattering [11] and investigating the droplet shapes by means of coherent diffractive imaging experiments [12, 13]. The results show that the shape sequence followed by superfluid ^{4}He nanodroplets is surprisingly similar to the one of rotating droplets made of a viscous fluid. A detailed theoretical analysis, based on Density Functional Theory, was able to explain such a behaviour as the result of the interplay between quantized vortices and capillary waves that provides the superfluid droplet with the appearance of a classical rotating object [4, 14, 15]. The main goal of this thesis project is to investigate the rotational properties of self-bound quantum droplets made of a heteronuclear binary Bose mixture of ^{41}K and ^{87}Rb. More precisely, a great attention is focused on a systematic analysis of vorticity in a uniform system, both in the self-bound regime and out of it, where an external confinement instead is required to keep the system together. These results represent the starting point in the study of rotations in droplets. The analysis of the shapes of rotating droplets is performed by means of a phase diagram where the reduced angular velocity Ω is plotted as a function of the reduced angular

momentum Λ.

In the following we will provide some information about how this thesis work is organized.
Chapter 1 consists of a general review of bosonic systems and it starts with an analysis of the physics of non-interacting bosons that directly leads to the phenomenon of Bose-Einstein condensation. After that, restricting to the framework of ultracold dilute atomic gases, the Bogoliubov theory of weakly interacting bosonic systems will be summarized. The general properties of superfluidity will then be discussed, focusing on how the main equations describing superfluids are related to the theory of dilute gases and what are their important phenomenological consequences.
In **Chapter 2** one can find a description of the formation of self-bound configurations in Bose-Einstein condensates characterized by competing interactions. The ^{41}K-^{87}Rb bosonic mixture will then be described in greater detail within the Density Functional Theory framework: as anticipated above, the competition between the mean field attraction and the repulsive Lee-Huang-Yang term, encoding quantum fluctuations, may lead to the formation of self-bound liquid droplets. Some thermodynamic properties of the uniform system will be computed and the Gross-Pitaevskii equations governing the mixture will be derived.
Chapter 3 is devoted to the discussion of the surface properties of a ^{41}K-^{87}Rb self-bound droplet. First, the surface tension of a planar liquid-vacuum interface will be determined, denoted as σ_0. After that, curvature effects will be introduced through the Tolman's length, δ. The balance between the surface tension and the quantum kinetic energy of the droplet determines its stability: too small droplets will be unstable and evaporate. We will determine the minimum critical size for droplet stability as a function of the interspecies scattering length a_{12}.
In **Chapter 4** we will discuss the development of vorticity inside a binary Bose mixture. We will start with the uniform ^{41}K-^{87}Rb mixture in the self-bound regime and we will work with a cylindrical geometry that allows to reduce to less demanding 2D numerical calculations. We will present results for the kinetic energy associated to a vortex line and make comparisons with the predictions given by the hydrodynamic approximation. We will consider different possibilities, i.e. a singly quantized vortex in both species, or a vortex in only one species, and discuss the resulting density profiles and the vortex energetic properties.
With **Chapter 5** we will consider rotating ^{41}K-^{87}Rb quantum droplets. First, the minimal droplet size required to host a single vortex will be estimated. After that, a detailed analysis of the rotation of a trapped ^{41}K-^{87}Rb mixture in the not-self-bound regime will be presented: in particular, we will highlight analogies and differences with the very well known case of a ^{4}He rotating bucket. Finally, we will analyze how angular momentum is stored in these rotating systems (by nucleation of quantized vortices or through capillary waves associated to quadrupolar deformations).
In **Appendix A** we will give a brief presentation of the scattering theory at low energy, focusing on the relationship between the *s*-wave scattering length and the coupling constant defining the contact interaction between bosons.
Appendix B is devoted to a detailed explanation of the numerical methods that are employed during the realization of this thesis work. The system under study is described by the Gross-Pitaevskii equations: they are two coupled nonlinear equations that admits only numerical solutions. After a general overview of the simulation domain, two main algorithms will be presented: the so called *evolution in imaginary time* allows to determine the ground state of the system, while its dynamics is explored by means of a *real time evolution*.
In **Appendix C** one can find an explicit derivation of the density profile for a quantum droplet made of a binary Bose mixture. These computations belong to the Density Functional Theory framework that was developed in Chapter 2 and they restrict to the approximation of a planar liquid-vacuum interface.

Chapter 1

Bose-Einstein Condensation and Superfluidity

This first introductory chapter is devoted to a general review of bosonic systems. We will start by analyzing the physics of non-interacting bosons, introducing the phenomenon of Bose-Einstein condensation. After that, we will turn to the description of interacting bosons and, making use of the Bogoliubov theory, we will see how superfluidity comes into play and what are its main phenomenological consequences.
The whole treatment is based on the approach that L. Pitaevskii and S. Stringari developed in [16].

1.1 Non-interacting bosons

A system of non-interacting bosons is described by the Bose distribution function that gives the average number of particles occupying some specific states (labelled by the wave vector $\vec{k}$):

$$n_{\mathrm{B}} = \frac{1}{e^{\beta(\epsilon(\vec{k})-\mu)}-1} \tag{1.1}$$

with $\beta = 1/k_{\mathrm{B}}T$, μ the chemical potential and $\epsilon(\vec{k})$ the single-particle energy. In the following we will focus on free particles (in the absence of any external potential) with mass m, for which:

$$\epsilon(\vec{k}) = \frac{\hbar^2 k^2}{2m} \tag{1.2}$$

Being N the total number of particles and V the volume of the system, in the thermodynamic limit ($N, V \to \infty$, with N/V=constant) a summation over discrete wave vectors can be substituted by an integral in the reciprocal space, so that the total number of particles can be computed as:

$$N = \sum_{\vec{k}} n_{\mathrm{B}}(\vec{k}) \longrightarrow \frac{V}{(2\pi)^3}\int d\vec{k}\,\frac{1}{e^{\beta(\epsilon(\vec{k})-\mu)}-1} = V\int_0^\infty d\epsilon\,\frac{\rho(\epsilon)}{e^{\beta(\epsilon-\mu)}-1} \tag{1.3}$$

where the density of states was introduced

$$\rho(\epsilon) \equiv \frac{1}{V}\sum_{\vec{k}}\delta(\epsilon(\vec{k})-\epsilon) = \frac{m^{3/2}}{\sqrt{2}\pi^2\hbar^3}\sqrt{\epsilon} \tag{1.4}$$

Performing the integrations, the number density of the bosonic system is obtained:

$$\rho \equiv \frac{N}{V} = \left(\frac{m\,k_{\mathrm{B}}\,T}{2\,\pi\,\hbar^2}\right)^{3/2} g_{3/2}(z) \tag{1.5}$$

$z \equiv e^{\beta\mu}$ is the fugacity and $g_{3/2}(z) \equiv \sum_{p=1}^{\infty} z^p/p^{3/2}$ is a function that is convergent for $z \leq 1$ and it has the following properties:

$$g_{3/2}(z=1) = \sum_{p=1}^{\infty} \frac{1}{p^{3/2}} = \zeta(3/2) = 2.612... \qquad g_{3/2}(z) \underset{z\ll 1}{\simeq} z \tag{1.6}$$

where ζ is the Riemann zeta function.
Developing Eq. (1.5) in the high-temperature limit $T \gg 1$ (i.e. $z \ll 1$), one gets:

$$\mu = -\frac{3}{2} k_B T \ln\left(\frac{m k_B T}{2\pi\hbar^2 \rho^{2/3}}\right) \tag{1.7}$$

The chemical potential is negative for large enough temperatures, but, as temperature is decreased, it reaches zero from below. There should exist a critical temperature T_c such that

$$\mu(T) \xrightarrow{T\to T_c} 0^-$$

Its explicit expression is obtained substituting $g_{3/2}(z=1)$ inside Eq. (1.5):

$$T_c = \frac{2\pi\hbar^2}{m k_B}\left(\frac{\rho}{\zeta(3/2)}\right)^{2/3} \tag{1.8}$$

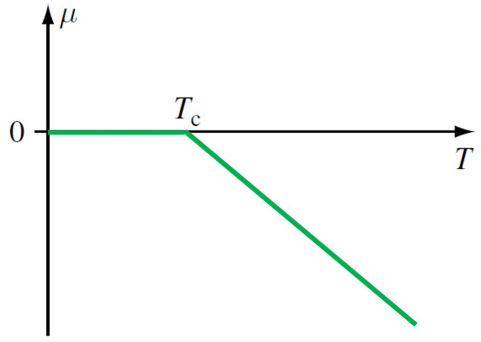

Figure 1.1: Chemical potential of a non-interacting Bose gas as a function of temperature. Figure taken from [17].

In 1925, on the basis of a paper of the Indian physicist S. N. Bose about the statistical description of the quanta of light [18], A. Einstein proposed a revolutionary picture that involves a phase transition in a gas of non-interacting bosons below the critical temperature T_c. This phase transition, that is a consequence of quantum statistical effects, is associated to the condensation of atoms in the lowest energy state: the number of particles occupying the ground state $\epsilon(\vec{k}=0) = 0$ is macroscopically large, $N_0 \gg 1$, and it grows with volume. This can be proven by analyzing the behaviour of the chemical potential below the critical temperature.

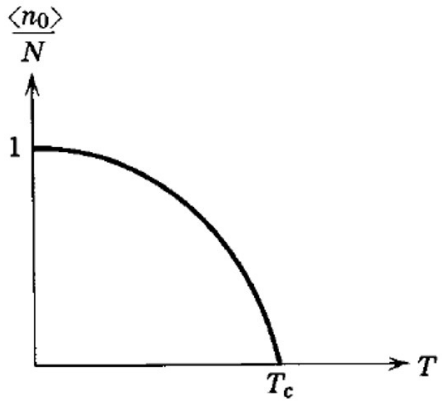

Figure 1.2: Condensate fraction as a function of temperature. Figure taken from [19].

From the number of particles in the ground state

$$N_0 = \rho_0 V = n(\vec{k}=0) = \frac{1}{e^{-\beta\mu} - 1} \tag{1.9}$$

the chemical potential reads

$$\mu = -k_B T \ln\left(1 + \frac{1}{N_0}\right) \xrightarrow[\rho_0 \text{ finite}]{N_0, V_0 \to \infty} 0 \qquad \forall\, T < T_c \tag{1.10}$$

Below the critical temperature the chemical potential remains equal to zero, provided that the ground state is macroscopically occupied: the function $\mu(T)$ is represented in Figure 1.1.
This new phenomenon is known as **Bose-Einstein condensation** (**BEC**); consequently, the critical temperature of Eq. (1.8) that marks the phase transition is called *condensation temperature*.

For a given $T < T_c$, the total number of particles of the system is expressed as the sum of two contributions: the number of particles in the condensate and the number of particles in the excited states

$$N \overset{T<T_c}{=} N_0 + \sum_{\vec{k}\neq 0} \frac{1}{e^{\beta\epsilon(\vec{k})} - 1} \tag{1.11}$$

It is worth stressing the fact that a macroscopic occupation of the ground state means that N_0 is a number of order N, while the other single-particle states have a microscopic occupation of order 1. The summation over $\vec{k} \neq 0$ is computed as in Eq. (1.3) and the result is provided by Eq. (1.5) with fugacity $z = 1$. By doing so, one obtains:

$$\begin{aligned} N &= N_0 + V \left(\frac{mk_BT}{2\pi\hbar^2}\right)^{3/2} \zeta(3/2) = N_0 + N \left(\frac{T}{T_c}\right)^{3/2} \\ \Rightarrow \quad \frac{N_0}{N} &= 1 - \left(\frac{T}{T_c}\right)^{3/2} \end{aligned} \tag{1.12}$$

The condensate fraction N_0/N (or, equivalently, ρ_0/ρ) represents the order parameter of a system of non-interacting bosons: it is zero in the normal phase and then it starts growing as soon as $T < T_c$, reaching its maximum at $T = 0$. As it is showed in Figure 1.2, the order parameter is continuous at the transition, while the first derivative is not: this is the peculiarity of a second order phase transition.

Under an experimental point view, for a long time these predictions had no practical impact: the first experimental studies on dilute atomic gases developed only from the 1970s, thanks to new techniques based on magnetic and optical trapping and advanced cooling mechanisms, while a great revolution took place in the 1980s with the advent of new laser based techniques to cool and trap neutral atoms. Finally, by combining different cooling techniques, two experimental teams at Boulder and at MIT succeeded in 1995 in reaching the temperatures and densities required to observe BEC in vapours of ^{87}Rb [20] and ^{23}Na [21].
Figure 1.3 shows the particle momentum distribution for the first observation of a Bose-Einstein condensate: it was produced in a vapor of ^{87}Rb atoms and it was confined by magnetic fields and evaporatively cooled [20]. The left frame corresponds to the gas just above condensation, with an isotropic velocity distribution given by the classical Boltzmann law. The condensate fraction first appeared near a temperature of 170 nK and a number density of 2.5×10^{12} cm^{-3} and it could be preserved for more than 15 seconds: in the central frame this is represented by the presence of a narrow peak, centered at zero velocity, on top of a broad thermal velocity distribution. The right frame was obtained after a further reduction, both of temperature and density, to 20 nK and 1×10^{11} cm^{-3}: the fraction of atoms that were in the low-velocity peak increased abruptly and the system now corresponds to a quasi-pure condensate.
A striking feature coming out from Figure 1.3 is the difference between aspect ratios for the two components of the cloud:

- the broad non-condensed fraction (yellow to green regions) displays an isotropic velocity distribution: it is consistent with a thermal equilibrium across many quantum wave functions;
- the condensate atoms (blue to white regions) form non-thermal elliptical patterns in the velocity plane: these particles, in fact, are all described by the same wave function, which carries an anisotropy reflecting that of the confining potential.

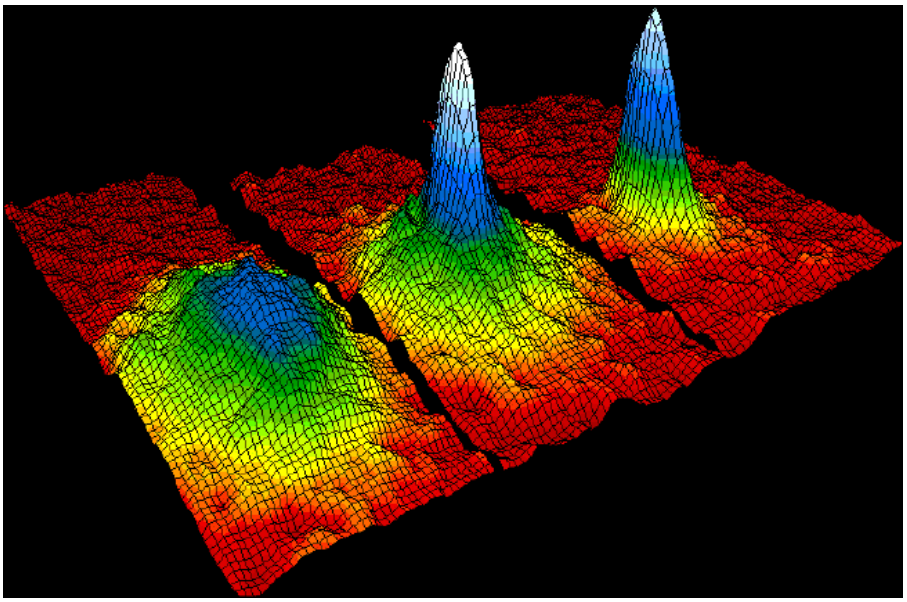

Figure 1.3: Momentum distribution for a gas of rubidium atoms that experimentally confirms the discovery of the Bose-Einstein condensation [20].The left frame corresponds to a gas just above condensation; the central frame is just after the appearance of the condensate; the right one, after further evaporation, corresponds to a quasi-pure condensate. Figure taken from NIST/JILA/CU-Boulder.

1.2 Weakly interacting Bose gas

The almost ideal Bose gas has the not trivial problem that the ground state energy is equal to zero in the absence of interactions, therefore a traditional perturbation analysis cannot be applied. Such a problem was solved in 1947 by Bogoliubov with the introduction of a new perturbation technique which modern approaches to Bose-Einstein condensation in dilute gases are based on.

Let r_0 be the typical range of the interatomic forces and $d = \rho^{-1/3}$ the average interparticle distance, fixed by the gas density $\rho = N/V$. A gas is said to be rarefied if it satisfies the following diluteness condition:

$$r_0 \ll d \tag{1.13}$$

As highlighted in [16], this condition has two important consequences:

- one can restrict only to interactions between pair of particles, safely neglecting those configurations where three or more particles interact simultaneously;
- the distance between two particles is always large enough to allow the use of asymptotic expressions for the wave function of the relative motion, which is fixed by the scattering amplitude. As a result, all the properties of the system can be expressed in terms of this quantity and the relevant values of momenta should satisfy the inequality $p\, r_0/\hbar \ll 1$. In this low energy limit, according to scattering theory [22–24], the scattering amplitude becomes a constant which is determined by the s-wave scattering length a. This quantity turns out to be the single parameter that characterizes the effects of the interaction on the physical properties of the gas.

The weakly interacting regime is achieved if the scattering length is small compared to the interparticle distance, requiring the smallness of the so-called gas parameter

$$\rho\, |a|^3 \ll 1 \tag{1.14}$$

A brief discussion of a weakly interacting Bose gas is now carried out in the second quantization formalism, therefore we introduce the field operators $\hat{\psi}^\dagger(\vec{r})$, $\hat{\psi}(\vec{r})$ that create and annihilate, respectively, a particle at point $\vec{r}$. For a system of bosons, these field operators obey the *canonical commutation relations*

$$\left[\hat{\psi}(\vec{r}),\, \hat{\psi}^\dagger(\vec{r}\,')\right] = \delta(\vec{r} - \vec{r}\,') \qquad \left[\hat{\psi}(\vec{r}),\, \hat{\psi}(\vec{r}\,')\right] = \left[\hat{\psi}^\dagger(\vec{r}),\, \hat{\psi}^\dagger(\vec{r}\,')\right] = 0 \tag{1.15}$$

A system of N interacting bosons with mass m can be described by the Hamiltonian

$$\hat{H} = \int d\vec{r} \left(\frac{\hbar^2}{2m} \vec{\nabla}\hat{\psi}^\dagger(\vec{r}) \cdot \vec{\nabla}\hat{\psi}(\vec{r}) \right) + \frac{1}{2} \int d\vec{r}\, d\vec{r}\,' \, \hat{\psi}^\dagger(\vec{r})\, \hat{\psi}^\dagger(\vec{r}\,')\, V(\vec{r} - \vec{r}\,')\, \hat{\psi}(\vec{r})\, \hat{\psi}(\vec{r}\,') \tag{1.16}$$

where $V(\vec{r})$ is the two-body potential and we assume the absence of any external potential.
The single-particle wave functions ϕ_i can be introduced to rewrite the field operator in the form

$$\hat{\psi}(\vec{r}) = \sum_i \phi_i(\vec{r})\, \hat{a}_i \tag{1.17}$$

where $\hat{a}_i$, $\hat{a}_i^\dagger$ are the annihilation and creation operators of a particle in the state ϕ_i and they obey the *canonical commutation relations*

$$\left[\hat{a}_i, \hat{a}_j^\dagger\right] = \delta_{ij} \qquad \left[\hat{a}_i, \hat{a}_j\right] = \left[\hat{a}_i^\dagger, \hat{a}_j^\dagger\right] = 0 \tag{1.18}$$

As already discussed, Bose-Einstein condensation occurs when the lowest single-particle state, labelled by $i = 0$, is occupied in a macroscopic way. It is then useful to separate in the field operator of Eq. (1.17) the condensate term from the other components:

$$\hat{\psi}(\vec{r}) \simeq \phi_0(\vec{r})\, \hat{a}_0 + \sum_{i \neq 0} \phi_i(\vec{r})\, \hat{a}_i \tag{1.19}$$

According to the macroscopic phenomena associated to BEC, on the one hand we have that $\langle \hat{a}_0^\dagger \hat{a}_0 \rangle = N_0 \gg 1$, on the other one the commutator between $\hat{a}_0$ and $\hat{a}_0^\dagger$ is of order 1. This is the key concept for the introduction of the Bogoliubov approximation that consists of ignoring the noncommutativity between the operators $\hat{a}_0$ and $\hat{a}_0^\dagger$ and replacing both of them with the c-number $\sqrt{N_0}$. The macroscopic component can be treated as a classical field, so that Eq. (1.19) becomes:

$$\hat{\psi}(\vec{r}) = \sqrt{N_0}\, \phi_0(\vec{r}) + \sum_{i \neq 0} \phi_i(\vec{r})\, \hat{a}_i = \psi_0(\vec{r}) + \delta\hat{\psi}(\vec{r}) \tag{1.20}$$

$\psi_0(\vec{r})$ is called the wave function of the condensate and it plays the role of an order parameter for the bosonic system. It is a complex quantity

$$\psi_0(\vec{r}) = \left|\psi_0(\vec{r})\right| e^{i\theta(\vec{r})} \tag{1.21}$$

where the modulus yields the condensate density $\left|\psi_0(\vec{r})\right|^2 = \rho_0(\vec{r})$, while the phase $\theta(\vec{r})$ plays an important role in coherence and superfluid phenomena, as it will be explored later in the chapter.
The diluteness condition discussed above guarantees that a detailed knowledge of the actual shape of the two-body potential is not necessary in order to describe the macroscopic properties of the gas: the only requirement is that the potential gives the correct value of the s-wave scattering length. It is then reasonable to assume the interaction to be modeled by a contact potential

$$V(\vec{r} - \vec{r}\,') = g\, \delta(\vec{r} - \vec{r}\,') \tag{1.22}$$

where the coupling constant g, formally defined as $g = \int d\vec{r}\, V(\vec{r})$, is related to the s-wave scattering length via the first-order Born approximation:

$$g = \frac{4\pi\hbar^2}{m} a \tag{1.23}$$

It can be positive or negative for a repulsive ($a > 0$) or attractive ($a < 0$) interaction, respectively (more details about the relationship between the s-wave scattering length and the interaction constant are developed in Appendix A).
Moreover, dealing with dilute Bose gases at very low temperatures, the non-condensed part $\delta\hat{\psi}$ can

be safely neglected developing the Bogoliubov approximation. Under these assumptions, Eq. (1.16) can be written as:

$$H = \int d\vec{r} \left(\frac{\hbar^2}{2m} \left| \vec{\nabla} \psi_0(\vec{r}) \right|^2 + \frac{1}{2} g \left| \psi_0(\vec{r}) \right|^4 \right) \tag{1.24}$$

Notice that this Hamiltonian is not an operator any more and it represents the total energy of the system.
For a uniform gas in a volume V at $T = 0$ all the atoms are in the condensate ($N = N_0$) and the condensate density coincides with the total density $\rho_0 = \rho$. In the ground state the order parameter is constant and it can be taken as a real quantity:

$$\psi_0(\vec{r}) \equiv \psi_0 = \rho^{1/2} = \left(\frac{N}{V} \right)^{1/2} \tag{1.25}$$

We recall here the very general and important feature that the order parameter is defined up to a constant phase factor $e^{i\alpha}$, reflecting the global $U(1)$ gauge symmetry exhibited by all the physical equations of the problem. Any explicit choice for the value of the phase (as it is done in Eq. (1.25)) corresponds to a formal breaking of the gauge symmetry: a more detailed and clearer analysis of the *spontaneous symmetry breaking* mechanism and its crucial consequences can be performed using the path integral formalism, for example in [17, 25, 26].
The ground state energy of the system is, therefore:

$$E_0 = \frac{1}{2} N g \rho \tag{1.26}$$

Contrary to the ideal Bose gas, now E_0 does not vanish at zero temperature due to the presence of the interaction.

1.2.1 Bogoliubov spectrum

The ground state energy in Eq. (1.26) has been obtained taking into account only the classical contribution ψ_0 in the decomposition of the field operator $\hat{\psi}(\vec{r})$. This is a very restrictive choice that hides some interesting physical results, therefore we perform a higher-order approximation including the noncondensed part $\delta\hat{\psi}$:

$$\hat{\psi}(\vec{r}) = \rho_0^{1/2} + \delta\hat{\psi}(\vec{r}) \tag{1.27}$$

The Bogoliubov theory consists of a Gaussian approximation up to the second order in the fluctuations of the field operator, i.e. Eq. (1.27) is substituted inside the Hamiltonian of Eq. (1.16) retaining all the quadratic terms in $\delta\hat{\psi}$, $\delta\hat{\psi}^\dagger$:

$$\hat{H} = g\frac{N_0^2}{2V^2} + \int d\vec{r} \left\{ \frac{\hbar^2}{2m} \vec{\nabla} \left(\delta\hat{\psi}^\dagger(\vec{r}) \right) \cdot \vec{\nabla} \left(\delta\hat{\psi}(\vec{r}) \right) + \frac{1}{2} g \rho_0 \left[\left(\delta\hat{\psi}(\vec{r}) \right)^2 + \left(\delta\hat{\psi}^\dagger(\vec{r}) \right)^2 + 4\, \delta\hat{\psi}^\dagger(\vec{r})\, \delta\hat{\psi}(\vec{r}) \right] \right\} \tag{1.28}$$

The linear terms in the fluctuations do not appear since they result in a constant contribution that can be reabsorbed through a redefinition of the total energy.
Even in this case we consider a uniform gas occupying a volume V where the field operator can be written in the form:

$$\hat{\psi}(\vec{r}) = \frac{1}{\sqrt{V}} \sum_{\vec{p}} \hat{a}_{\vec{p}}\, e^{i\vec{p}\cdot\vec{r}/\hbar} \tag{1.29}$$

where $\hat{a}_{\vec{p}}$ is the operator annihilating a particle in the single-particle state with momentum $\vec{p}$ and the values of $\vec{p}$ obey cyclic boundary conditions. At this point, one can rewrite the Hamiltonian of Eq. (1.28) in momentum space considering that:

- the fluctuation operators, using Eq. (1.29), become:

$$\delta\hat{\psi}(\vec{r}) = \frac{1}{\sqrt{V}} \sum_{\vec{p}\neq 0} \hat{a}_{\vec{p}}\, e^{i\vec{p}\cdot\vec{r}/\hbar} \tag{1.30}$$

- the presence of the fluctuations implies that there is a non-negligible number of atoms (the so-called *normal part*) that is not in the BEC phase, given by:

$$N' = \int d\vec{r}\, \delta\hat{\psi}^\dagger(\vec{r})\, \delta\hat{\psi}(\vec{r}) = \sum_{\vec{p}\neq 0} \hat{a}^\dagger_{\vec{p}}\, \hat{a}_{\vec{p}} \tag{1.31}$$

  such that the total number of atoms is $N = N_0 + N'$. As a result, neglecting higher order corrections, in the first term of Eq. (1.28) the following replacement is required:

$$N_0^2 \simeq N^2 - 2N \sum_{\vec{p}\neq 0} \hat{a}^\dagger_{\vec{p}}\, \hat{a}_{\vec{p}} \tag{1.32}$$

  The Gaussian level of the approximation alllows to substitute $\rho_0 \simeq \rho$ in the third term of Eq. (1.28).

- in order to achieve a higher accuracy, it is necessary to go beyond the lowest-order Born approximation for the relation between the two-body potential and the s-wave scattering length. Using higher order perturbation theory (see [22]) one finds the following replacement for the coupling constant:

$$g \longmapsto g\left(1 + \frac{g}{V}\sum_{\vec{p}\neq 0}\frac{m}{p^2}\right) \tag{1.33}$$

Performing these steps, the final expression for the Hamiltonian in the Fourier transform representation is:

$$\hat{H} = g\frac{N^2}{2V^2} + \sum_{\vec{p}\neq 0}\frac{p^2}{2m}\hat{a}^\dagger_{\vec{p}}\,\hat{a}_{\vec{p}} + \frac{1}{2}g\rho\sum_{\vec{p}\neq 0}\left(2\hat{a}^\dagger_{\vec{p}}\,\hat{a}_{\vec{p}} + \hat{a}^\dagger_{\vec{p}}\,\hat{a}^\dagger_{-\vec{p}} + \hat{a}_{\vec{p}}\,\hat{a}_{-\vec{p}} + \frac{mg\rho}{p^2}\right) \tag{1.34}$$

This Hamiltonian is quadratic in the operators $\hat{a}_{\vec{p}}$, $\hat{a}^\dagger_{\vec{p}}$ and can be diagonalized by the following linear transformation, known as *Bogoliubov transformation*:

$$\begin{cases} \hat{a}_{\vec{p}} &= u_{\vec{p}}\,\hat{b}_{\vec{p}} + v^*_{-\vec{p}}\,\hat{b}^\dagger_{-\vec{p}} \\ \hat{a}^\dagger_{\vec{p}} &= u^*_{\vec{p}}\,\hat{b}^\dagger_{\vec{p}} + v_{-\vec{p}}\,\hat{b}_{-\vec{p}} \end{cases} \tag{1.35}$$

The new operators $\hat{b}_{\vec{p}}$, $\hat{b}^\dagger_{\vec{p}}$ must obey the same commutation relations as $\hat{a}_{\vec{p}}$, $\hat{a}^\dagger_{\vec{p}}$ and this is true if

$$|u_{\vec{p}}|^2 - |v_{-\vec{p}}|^2 = 1 \qquad \longrightarrow \qquad \begin{cases} u_{\vec{p}} &= \cosh\alpha_{\vec{p}} \\ v_{-\vec{p}} &= \sinh\alpha_{\vec{p}} \end{cases} \tag{1.36}$$

The parameter $\alpha_{\vec{p}}$ is chosen in order to make the off diagonal coefficients of the Hamiltonian in Eq. (1.34) vanish. This condition takes the explicit form

$$\frac{g\rho}{2}\left(|u_{\vec{p}}|^2 + |v_{-\vec{p}}|^2\right) + \left(\frac{p^2}{2m} + g\rho\right) u_{\vec{p}}\, v_{-\vec{p}} = 0 \qquad \longrightarrow \qquad \coth 2\alpha_{\vec{p}} = -\frac{p^2/2m + g\rho}{g\rho} \tag{1.37}$$

By doing so, the final diagonal form of the Hamiltonian reads:

$$\hat{H} = E_0 + \sum_{\vec{p}\neq 0}\epsilon(p)\,\hat{b}^\dagger_{\vec{p}}\,\hat{b}_{\vec{p}} \tag{1.38}$$

where

$$E_0 = \frac{1}{2}Ng\rho + \frac{1}{2}\sum_{\vec{p}\neq 0}\left[\epsilon(p) - g\rho - \frac{p^2}{2m} + \frac{m(g\rho)^2}{p^2}\right] \tag{1.39}$$

is the ground state energy calculated at the quadratic order approximation, while

$$\epsilon(p) = \sqrt{\left(\frac{p^2}{2m}\right)^2 + \frac{g\rho}{m}p^2} = \frac{p}{2m}\sqrt{p^2 + (2mc)^2} \qquad \text{with} \quad c \equiv \sqrt{\frac{g\rho}{m}} \tag{1.40}$$

is the famous **Bogoliubov dispersion relation** for elementary excitations of the system [27].
This last set of equations provides a deep physical meaning: the original system of (weakly) interacting particles can be described in terms of a Hamiltonian of independent quasi-particles with single-particle energy $\epsilon(p)$ and whose annihilation and creation operators are, respectively, $\hat{b}_{\vec{p}}$ and $\hat{b}^\dagger_{\vec{p}}$.
The Bogoliubov spectrum in Eq. (1.40) shows two interesting limits:

- in the long wavelength limit, i.e. for $p \ll mc$, it approaches the dispersion relation of acoustic waves
$$\epsilon(p) \simeq c\,p \tag{1.41}$$
The quantity c is then identified as the sound velocity in the Bose gas;
- for large values of the momentum $p \gg mc$, Eq. (1.40) goes back to the dispersion relation of a free particle that is characteristic of a Bose-Einstein condensate:
$$\epsilon(p) \simeq \frac{p^2}{2m} \tag{1.42}$$

Bogoliubov theory shows that the presence of the interaction $g > 0$ alters the dispersion relation from a quadratic to a linear behaviour in p: this fact leads to superfluidity, which will be explained at the end of this chapter.

1.2.2 Quantum depletion

Let us consider the classical solution $\psi_0 = \rho_0^{1/2}$ and analyze the consequences of a non-vanishing interaction.
It was already seen that it is possible to define the normal part N' which corresponds to the number of particles in the excited states, such that the total number of particles can be written as:

$$N = N_0 + N' = \psi_0^2 V + N' \tag{1.43}$$

In the absence of the interaction ($g = 0$) the normal part is simply given by a summation over the Bose distribution

$$N' = \sum_{\vec{k}\neq 0} n_{\mathrm{B}}(\vec{k})|_{\mu=0} \tag{1.44}$$

and so the order parameter can be fixed from the total number of particles.
When the interaction is switched on ($g > 0$), this is no longer true since ψ_0 becomes a dynamical variable that determines also the normal part N'. Restricting the discussion to zero temperature and following Ref. [26], one can show that

$$N' = \frac{V}{3\pi^2}(mg)^{3/2}\psi_0^3 \tag{1.45}$$

and Eq. (1.43) becomes

$$N = V\left[\underbrace{\psi_0^2}_{\text{classical solution}} + \underbrace{\frac{1}{3\pi^2}(mg)^{3/2}\psi_0^3}_{\text{Gaussian fluctuations}}\right] \tag{1.46}$$

Eq. (1.46) allows to determine the condensed density ψ_0^2. Remembering that we performed an expansion where the fluctuations are assumed to be small, we expect the second term to be much smaller than the first one, so that:

$$\psi_0^2 \underset{T=0}{\simeq} \rho - \frac{1}{3\pi^2}(mg)^{3/2}\rho^{3/2} \tag{1.47}$$

For $g > 0$ the number of particles in the ground state is reduced by the presence of the interaction: this is a pure quantum mechanical effect known as *depletion*.
This phenomenon has direct consequences also on the total energy of the system. In particular, the ground state energy of Eq. (1.39) can be calculated by replacing the sum with an integral in momentum space and observing that only values $p \simeq \sqrt{mg\rho}$ give an important contribution in the integration. The correct result was computed by Lee, Huang, Yang in 1957 [9]:

$$E_0 = g\frac{N^2}{2V}\left[1 + \frac{128}{15\sqrt{\pi}}\left(\rho a^3\right)^{1/2}\right] \tag{1.48}$$

The second term, known as **Lee-Huang-Yang (LHY) correction**, accounts for quantum depletion and it gives a contribution to the energy per atom E/N that is proportional to $\rho^{3/2}$: this peculiar behaviour will play a crucial role in the formation of self-bound systems of binary Bose mixtures, that will be treated in Chapter 2. Notice that the LHY correction for the energy density $\mathcal{E} = E/V$ is proportional to $\rho^{5/2}$.

The Bogoliubov theory, as described above, is appropriate in the dilute limit ($\rho \ll 1$) or when the coupling is weak ($g \ll 1$): in any case, depletion is always present due to quantum fluctuations.
Summarizing, we have seen that:

- in the non-interacting case, at $T = 0$ all the particles occupy the ground state ($\rho = \rho_0$), while at $T > 0$ there is a finite depletion ($\rho_0 < \rho$) as a consequence of *thermal* fluctuations;
- in the interacting case, depletion is already present at $T = 0$ as a result of *quantum* fluctuations.

1.3 Landau criterion for superfluidity

The flow of a steady state current in normal environments is prevented by the mechanism of energy dissipation: particles constituting the current flow scatter off imperfections inside the system, thereby converting part of their energy into the creation of elementary excitations (macroscopically, this corresponds to heat production).
Such a mechanism seems to be inactivated in superfluid states of matter, where the current flow is dissipationless: how can it be possible?
First of all, if elementary excitations were so energetically high-lying that the kinetic energy stored in the particle current would not be sufficient to create them, then no energy could be exchanged. Actually, this trivial answer is not consistent with the situation encountered with superfluids, where there is no energy gap separating the quasi-particle excitations from the ground state: on the contrary, the dispersion relation $\epsilon(p)$ vanishes linearly as $p \to 0$.
The correct explanation was provided by Landau with a brilliant argument in [28], where he showed that an acoustic excitation spectrum is sufficient to generate dissipationless transport phenomena.
Let's consider the flow of some fluid through a pipe under the following assumptions:

- liquid flows with a constant velocity $\vec{v}$;
- the walls of the pipe are rough and the particles of the liquid are slowed down by back-scattering with these imperfections, introducing viscosity in the system.

The situation can be analyzed from two different points of view. The first one is the laboratory frame (Figure 1.4 (a)) where the fluid is moving with velocity $\vec{v}$ and the walls can be seen as a static perturbation. The second one is the frame that is co-moving with the fluid (Figure 1.4 (b)): here the fluid is at rest and it sees the pipe moving with opposite velocity $-\vec{v}$, while the walls represent time-dependent perturbations.
These two reference frames are connected by a Galilean transformation. By denoting with M the total mass of the fluid and with U its internal energy, in the rest frame the fluid has momentum $\vec{p}$ and

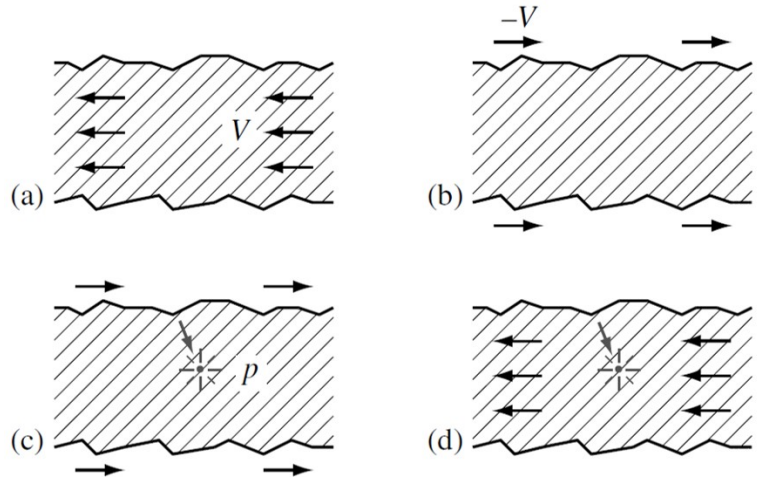

Figure 1.4: (a) Flow of a fluid through a rough pipe. (b) The same viewed from the rest frame of the fluid. (c) Dissipative creation of a (quasi-particle) excitation. (d) The same viewed from the laboratory frame. Figure taken from [17]

energy $E = U + \frac{p^2}{2M}$. The corresponding momentum and energy in the laboratory frame (denoted with a "prime ") are:

$$\vec{p}\,' = \vec{p} + M\vec{v} \qquad E' = U + \frac{p'^2}{2M} = E + \frac{M}{2}v^2 + \vec{v}\cdot\vec{p} \tag{1.49}$$

We can start from a situation where, at time $t = 0$, the fluid has zero energy and momentum in its rest frame. Immediately at $t > 0$ we can consider events where the particles of the fluid are scattered by the rough boundaries of the pipe: in the rest frame (Figure 1.4 (c)) there is a transfer of momentum $\vec{p}$ from the pipe to the fluid that leads to the creation of an elementary excitation with energy $\epsilon(p)$. These same events correspond, in the laboratory frame (Figure 1.4 (d)) to a transfer of both energy and momentum from the fluid towards the pipe. Energies and momenta in both reference frames evaluated before and after the creation of an elementary excitation are collected in Table 1.1.

	Rest frame	Lab frame
initial condition	$\vec{p}_i = 0$ $E_i = 0$	$\vec{p}_i\,' = M\vec{v}$ $E_i\,' = \frac{M}{2}v^2$
final condition	$\vec{p}_f = \vec{p}$ $E_f = \epsilon(p)$	$\vec{p}_f\,' = \vec{p} + M\vec{v}$ $E_f\,' = \epsilon(p) + \frac{M}{2}v^2 + \vec{v}\cdot\vec{p}$

Table 1.1: Initial and final states in the two reference frames.

Dissipation implies that the fluid loses part of its energy in favour of the walls, leading to the following condition:

$$E_f\,' - E_i\,' < 0 \qquad \Rightarrow \qquad \epsilon(p) + \vec{v}\cdot\vec{p} < 0 \qquad \forall\vec{p} \tag{1.50}$$

Since $\vec{v}\cdot\vec{p} > -v\,q$, there exists a minimum velocity

$$v_{min} = \min_{\vec{p}} \frac{\epsilon(p)}{p} \tag{1.51}$$

such that for each velocity smaller than this critical value there is no dissipation at all.
Eq.(1.51) represents the heart of the so-called Landau criterion for superfluidity, the reason becoming clear after the discussion of the following two applications:

- normal fluids can be approximated as made of almost free particles (with mass m) with the usual quadratic dispersion relation:

$$\epsilon(p) = \frac{p^2}{2m} \qquad \Rightarrow \qquad v_{min} = \min_{\vec{p}} \frac{p}{2m} = 0 \tag{1.52}$$

Dissipation takes place for every value of fluid velocity.

- superfluids are characterized by an acoustic spectrum, so that:

$$\epsilon(p) \underset{p\ll 1}{\simeq} c\,p \qquad \Rightarrow \qquad v_{min} = \min_{\vec{p}} \frac{c\,p}{p} = c \tag{1.53}$$

The sound velocity in the medium c represents the critical value below which the system enters the superfluid regime.
Notice that the critical velocity corresponds to the sound velocity, as represented in the left panel of Figure 1.5, only in the approximation of weakly interacting bosons that can be treated by means of Bogoliubov theory. The situation is slightly more complicated when dealing with strongly interacting Bose systems: the right panel of Figure 1.5, for instance, shows the case of ^{4}He where the critical velocity is actually determined by the roton minimum.

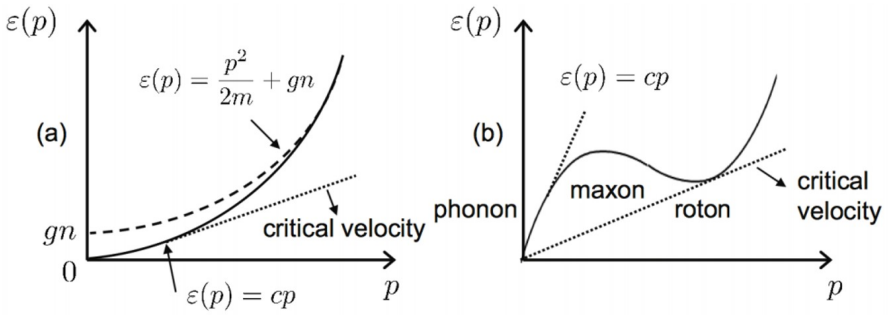

Figure 1.5: On the left it is shown the excitation spectrum of a weakly interacting Bose gas, for which the critical velocity is equal to the sound velocity, $v_c = c$. On the right the excitation spectrum of a strongly interacting Bose liquid as ^{4}He, for which the critical velocity is smaller than the sound velocity, $v_c < c$. Figure taken from [16].

1.4 Phenomenology of superfluidity

In order to analyze the rotation of a superfluid, let's write the order parameter using the *hydrodynamic form*, i.e. in terms of a density and a phase:

$$\psi(\vec{r},t) = \sqrt{\rho(\vec{r},t)}\, e^{i\theta(\vec{r},t)} \tag{1.54}$$

The current density associated to the system is, by definition:

$$\vec{j}(\vec{r},t) = \frac{\hbar}{2m\,i}\left[\psi^*(\vec{r},t)\,\vec{\nabla}\psi(\vec{r},t) - \vec{\nabla}\psi^*(\vec{r},t)\,\psi(\vec{r},t)\right] = \rho(\vec{r},t)\frac{\hbar}{m}\vec{\nabla}\theta(\vec{r},t) \tag{1.55}$$

It follows that the velocity of the condensate flow is given by:

$$\vec{v}_s(\vec{r},t) = \frac{\hbar}{m}\vec{\nabla}\theta(\vec{r},t) \tag{1.56}$$

The identification of the superfluid velocity with the gradient of the phase of the order parameter represents a key relationship between Bose-Einstein condensation and superfluidity. It is worth noticing that it would be wrong to identify the condensate density $\rho_0 = |\psi_0|^2$ with the superfluid density ρ_s. This distinction is already clear at $T = 0$, where the whole fluid is superfluid and $\rho_s = \rho$, while the condensate density $|\psi_0|^2$ is smaller than ρ because of the quantum depletion: as an example, at $T = 0$ liquid ^{4}He is 100 % superfluid, but less than 10 % condensate.
Let's now consider a ring filled with a superfluid flowing with velocity $\vec{v}_s$. A steady state of the system is described by a non vanishing superfluid velocity: this means that, due to the absence of

dissipation, $\vec{v}_s$ cannot decrease, i.e. it is time-independent. From symmetry arguments, the velocity is directed along the poloidal direction and one can introduce a circular closed path $\mathcal{C}$ that lies inside the ring.
The circulation of the superfluid velocity along the curve $\mathcal{C}$ is:

$$\kappa = \oint_{\mathcal{C}} d\vec{s} \cdot \vec{v}_s = \frac{\hbar}{m} \oint_{\mathcal{C}} d\vec{s} \cdot \vec{\nabla}\theta = \frac{\hbar}{m} \Delta\theta \tag{1.57}$$

$\Delta\theta$ represents the variation of the quantum mechanical phase after a closed path and its explicit expression is obtained by recalling that the complex wave function in Eq. (1.54), being the real physical quantity, must be a single-valued continuous function: this means that, after a closed path, its value goes back to the starting one. The phase variation must thus be an integer multiple of 2π and a direct substitution inside Eq. (1.57) leads to the crucial result:

$$\kappa = \frac{h}{m} n, \qquad\qquad n \in \mathbb{Z} \tag{1.58}$$

The circulation of the superfluid velocity is quantized in units of h/m: $\vec{v}_s$ can acquire only some specific finite values, as it is experimentally verified [29].
By taking the curl of Eq. (1.56) one immediately finds out that the superfluid velocity is an irrotational vector field, that is:

$$\vec{\nabla} \times \vec{v}_s = 0 \tag{1.59}$$

If the circulation was computed by means of Stokes' theorem (where the surface enclosed by the curve $\mathcal{C}$ is denoted by Σ), the only possible solution would be a vanishing superfluid velocity, in fact:

$$\oint_{\mathcal{C}} d\vec{s} \cdot \vec{v}_s = \int_{\Sigma\,:\,\partial\Sigma=\mathcal{C}} d\vec{\Sigma} \cdot \left(\vec{\nabla} \times \vec{v}_s\right) = 0 \qquad \forall \mathcal{C} \qquad \Rightarrow \qquad \vec{v}_s = 0 \tag{1.60}$$

However this result is not correct because Stokes' theorem cannot be applied to the particular system under consideration: the starting hypothesis are not satisfied, since we are dealing with a space that is not simply connected due to the presence of the hole in the middle of the ring.
Let's now consider a system where Stokes' theorem is supposed to be valid, for instance a vessel with a cylindrical shape, and let's perform the following operations:

- the vessel is filled with a fluid while it is kept in a high energy phase: the fluid is a normal fluid since superfluidity is suppressed by thermal fluctuations;
- applying a rotation to the cylinder around its symmetry axis, angular momentum is transferred to the normal fluid (microscopically, it takes place thanks to the roughness of the walls);
- the system is now brought below the critical temperature, entering the superfluid phase. At this point, applying Stokes' theorem, the only possible solution is the one in Eq. (1.60).

This conclusion, however, is in contrast with experimental results that show a macroscopic rotation of the superfluid, compatible with a non-vanishing superfluid velocity. Such a paradox can be solved by observing that the vectorial equation (1.59) has a solution $\vec{v}_s \neq 0$, so that its circulation is different from zero, too. It can be proven working with cylindrical coordinates (r, φ, z) that are naturally suggested by the geometry of the system. From symmetry arguments, $\vec{v}_s$ must lay along the poloidal direction and should depend only on the radial coordinate:

$$\vec{v}_s = v_{s,\varphi}(r)\ \hat{u}_\varphi \tag{1.61}$$

Eq. (1.59) admits as a solution a finite superfluid velocity with a vortex-shape:

$$\vec{v}_s(r) = \frac{\kappa}{2\pi r}\ \hat{u}_\varphi \tag{1.62}$$

The system generates some topological defects in correspondence of $r = 0$ such that the velocity $\vec{v}_s$ is finite, but at the same time the superfluid is still irrotational. The presence of these topological defects plays a crucial role because this configuration, which at the beginning was thought to be associated to a trivial topological domain, actually lives in a space that is not simply connected: once more, Stokes' theorem cannot be applied.
Moreover, these defects take place only in a discrete number inside rotating superfluids: vortices, in fact, are quantized and they share the same quantum number n of circulation in Eq. (1.58). They usually arrange in regular patterns, as it can be seen in Figure 1.6: one of these configurations can be a triangular lattice, known as Abrikosov lattice of vortices (see [31] for details).

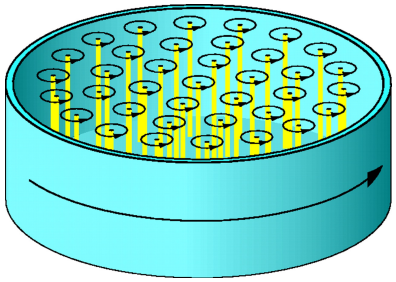

Figure 1.6: Rotation of a superfluid is not uniform but takes place via a lattice of quantized vortices, whose cores (yellow) are parallel to the axis of rotation. Small arrows indicate the circulation of the superfluid velocity v_s around each singularity. Figure taken from [30].

For a superfluid enclosed in a cylindrical container rotating around its symmetry axis, only the normal component will be brought into rotation, in fact at low enough angular velocity the superfluid part will remain at rest ($\vec{v}_s = 0$). However, for a sufficiently large angular velocity such a state becomes energetically unfavourable, as it can be seen moving to frame rotating with the container, where the total energy reads

$$E_r = E - \omega L_z \tag{1.63}$$

being E and L_z the energy and the third component of the angular momentum (supposing a rotation around the z axis) in the laboratory frame, while ω is the angular velocity of the cylinder. For sufficiently large values of ω, configurations with $\omega L_z > 0$ are thermodinamically more favourable than the superfluid at rest, where $L_z = 0$. As it was seen, a superfluid cannot rotate in a rigid way so the rotation can take place only through the creation of quantized vortex lines.
In the case of a single straight vortex line along the symmetry axis of a cylindrical vessel (with length L and radius R) the velocity field is given by Eq.(1.62) and the total angular momentum of the fluid is:

$$L_z = \int dm\, |\vec{r} \times \vec{v}_s| = \int_{cylinder} d\vec{r}\, \rho(r)\, v_s(r)\, r \simeq \pi R^2 L \rho_s \frac{\hbar}{m} \tag{1.64}$$

The size of the vortex core r_c is assumed to be much smaller than R, so that the density can be approximated by the value of the superfluid density ρ_s far from the core.
The energy carried by a vortex line is predominantly kinetic energy

$$E_v = \int d\vec{r}\, \frac{1}{2} \rho(r)\, v_s(r)^2 \simeq L\pi\, \rho_s \left(\frac{\hbar}{m}\right)^2 \ln\left(\frac{R}{r_c}\right) \tag{1.65}$$

The critical angular velocity ω_c for the existence of an energetically stable vortex line is obtained imposing $E - E_r = E_v$ inside Eq. (1.63):

$$\omega_c = \frac{E_v}{L_z} = \frac{\hbar}{m\, R^2} \ln\left(\frac{R}{r_c}\right) \tag{1.66}$$

This corresponds to the result obtained by Feynman in [32], leading to the following important conclusion: for $\omega \gg \omega_c$ more vortices will appear in the fluid, making the rotation of the system more similar to the one of a rigid body, characterized by a vorticity $\vec{\nabla} \times \vec{v}_s = 2\,\vec{\omega}$.
The physical meaning of the quantum number n can be recovered considering as a closed path inside the fluid the circumference $\mathcal{C}(R)$ at the border of the cylinder. The velocity field associated with a rigid rotation is $\vec{v}_s = \omega R\, \hat{u}_\varphi$ with a corresponding circulation

$$\kappa = \oint_{\mathcal{C}(R)} d\vec{s} \cdot \vec{v}_s = 2\,\pi\,\omega\, R^2 \tag{1.67}$$

A direct comparison of Eqs. (1.58, 1.67) shows that n represents the number of vortices enclosed inside the cylindrical vessel:

$$n = \frac{2\,m\,\omega}{h}\,\pi R^2 \tag{1.68}$$

Finally, the areal density of vortices turns out to be

$$\frac{n}{\pi R^2} = \frac{m}{\pi\hbar}\,\omega \tag{1.69}$$

that is, the higher the angular velocity transferred to the fluid, the higher the number of vortices per unit area.

1.5 Rotation and shapes of a superfluid

The moment of inertia Θ relative to the z axis can be defined as the response of the system to a rotational field $H_{\rm pert} = -\omega\,L_z$ according to the relationship

$$\langle L_z\rangle = \Theta\,\omega \tag{1.70}$$

where $L_z = \sum_i \left(x_i\,p_i^y - y_i\,p_i^x\right)$ is the third component of the angular momentum (for a system made of $i = 1, ..., N$ particles) and the average is taken over stationary configurations in the presence of the perturbation.
For a classical system, the moment of inertia takes the rigid value

$$\Theta_{\rm rig} = m\int d\vec{r}\,\rho(\vec{r})\,\left(x^2+y^2\right) = N\,m\,\left(\langle x^2\rangle + \langle y^2\rangle\right) \tag{1.71}$$

For a quantum system, L_z is replaced by the third component of the angular momentum operator

$$\hat{L}_z = x\,\hat{p}_y - y\,\hat{p}_x = -i\hbar\left(x\frac{\partial}{\partial y} - y\frac{\partial}{\partial x}\right) \tag{1.72}$$

while the moment of inertia is given by the irrotational form

$$\Theta_{\rm irr} = \varepsilon^2\,\Theta_{\rm rig} \tag{1.73}$$

where the deformation parameter ε accounts for the shape of the atomic cloud in the x-y plane and is defined as:

$$\varepsilon = \frac{\langle y^2\rangle - \langle x^2\rangle}{\langle y^2\rangle + \langle x^2\rangle} \tag{1.74}$$

Notice that all these results do not assume a small angular velocity and that, in general, the value of ε will depend on ω.
Eq. (1.73) shows that in a superfluid the value of the moment of inertia is smaller than the rigid value. In particular, for axisymmetric systems (where $\langle x^2\rangle = \langle y^2\rangle$), the above relation implies a vanishing angular momentum $\langle\hat{L}_z\rangle = \Theta_{\rm irr}\,\omega = 0$. This means that axisymmetric configurations cannot spin: if these systems are set into rotation, a vortex array develops in such a way the angular momentum to be stored in its vortex cores. We stress again the fact that the presence of a large enough vortex array confers to the system some of the properties of their rotating classical counterparts.
On the contrary, non axisymmetric configurations (where $\langle x^2\rangle \neq \langle y^2\rangle$) are able to spin with a finite angular momentum $\langle\hat{L}_z\rangle = \Theta_{\rm irr}\,\omega \equiv L_{\rm cap}$ that is stored in the form of the so-called *capillary waves*. They correspond to surface excitations associated to quadrupolar deformations and, in the specific case of a rotation around the z axis, they can be described by the following irrotational velocity field:

$$\vec{v}(\vec{r}) \propto \vec{\nabla}\,(xy) \tag{1.75}$$

Even if capillary waves can form in the absence of quantized vortices, in general these two configurations may coexist in non axisymmetric systems, producing two different irrotational velocity flows

that are compatible with the superfluid requirement.

The interplay between vortices and capillary waves was theoretically studied in superfluid ^{4}He, both for deformable self-sustained cylinders [33] and for quantum droplets [4, 14] . In this last case, it was verified that oblate axisymmetric drops can rotate only by nucleating quantized vortices, while spinning prolate ones can host both vortices and capillary waves: the results for ^{4}He rotating droplets will be presented in more detail at the beginning of Chapter 5.
In this thesis work we will perform a similar analysis with the two same geometrical configurations as above, but considering a different bosonic system: a binary Bose mixture.

Chapter 2

Theory of binary Bose mixtures

In this chapter we will discuss the conditions underlying the formation of self-bound states in Bose-Einstein condensates characterized by competing interactions. We will then focus on the description of the ^{41}K-^{87}Rb bosonic mixture within the Density Functional Theory framework: in these binary systems the competition between the mean field attraction and the repulsive character of quantum fluctuations (encoded inside the Lee-Huang-Yang correction) may lead to the formation of self-bound liquid droplets. A theoretical treatment of the uniform system allows to derive explicit expressions for the bulk densities of the two species that will play an important role throughout the whole thesis work. Finally, the Gross-Pitaevskii equations for this mixture will be derived and few hints about their numerical resolution will be provided.

2.1 Self-bound systems

Within the Density Functional Theory (DFT) framework, the total energy of a single-component Bose Einstein condensate of N bosons with mass m inside a volume V can be written as

$$E = \int_V d\vec{r}\, \mathcal{E}\,[\rho] \tag{2.1}$$

where the energy density $\mathcal{E}\,[\rho]$ is a functional of the local density $\rho(\vec{r})$ and of the order parameter $\psi(\vec{r})$, such that $|\psi(\vec{r})|^2 = \rho(\vec{r})$.
At the mean field level, the interparticle interaction can be described by a zero-range repulsive potential (as already discussed in Chapter 1 for a weakly interacting Bose gas) with a positive interaction constant connected to the s-wave scattering length from $g = \frac{4\pi\hbar^2}{m}a$. Under these assumptions, Eq. (2.1) becomes:

$$E = \int_V d\vec{r} \left(\frac{\hbar^2}{2m} |\vec{\nabla}\psi(\vec{r})|^2 + \frac{1}{2}\, g\, \rho^2(\vec{r}) + V_{ext}\, \rho(\vec{r}) \right) \tag{2.2}$$

where V_{ext} is a possible external potential acting on the system.
In the mean field approximation [34] atoms still occupy one single state, as it would be in the absence of interactions, however the interaction modifies this state with respect to the single-particle one. The ground state energy of a uniform system with constant density ρ (and in the absence of external potentials) is simply:

$$\frac{E}{V} = \frac{1}{2}\, g\, \rho^2 \tag{2.3}$$

The repulsive character of the interaction implies that the energy of the system is lowest when the density has the lowest possible value: the system is in the gas phase and it always expands, so an external trapping potential is needed to confine it. In the opposite case of an attractive interparticle interaction ($g < 0$), the energy is minimized when ρ is maximized: the ensemble can only collapse on itself.

In the weakly interacting regime, corrections going beyond the mean field approximation are obtained performing a perturbative expansion of the total energy in the gas parameter $\rho a^3 \ll 1$. The first exact calculation of the next leading-order term in the energy is known as LHY correction, from T.D. Lee, K. Huang and C.N. Yang who developed it in 1957 [9]. The physical interpretation of this new term is strictly related to the quantum depletion: even in the ground state, the collective modes of the BEC undergo zero-point fluctuations as dictated by Heisenberg's uncertainty principle.
The total energy of the uniform system displays now a new term:

$$\frac{E}{V} = \frac{1}{2} g \rho^2 + \alpha_{\mathrm{LHY}} (g \rho)^{5/2} \tag{2.4}$$

where the constant α_{LHY} depends only on the atomic mass. Being the interaction repulsive, the LHY correction gives a positive contribution exactly as the mean field term, as it is showed in Figure 2.1: the system remains in the gas phase.

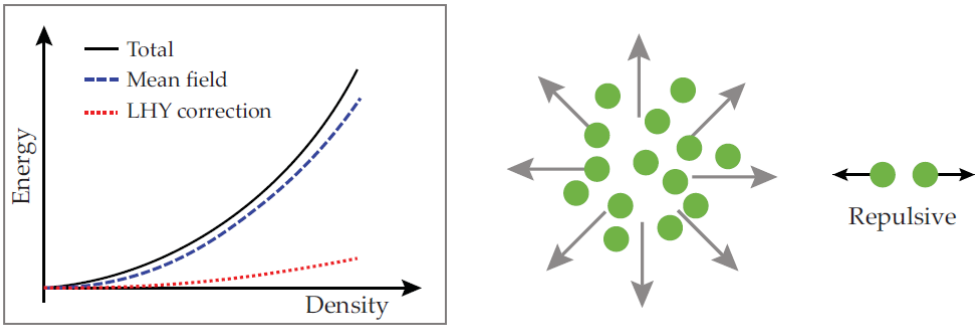

Figure 2.1: A single-species Bose Einstein condensate has repulsive short-range interactions. The sum of the mean-field term and the LHY correction yields a positive repulsive term: atoms are not bound and they form a gas. Figure taken from [34].

The game-changing idea to reverse the nature of the BEC was developed in 2015 by D. Petrov in his seminal work [5] and it was experimentally observed by a group headed by T. Pfau few months later [35]. Even if making use of different configurations, both of them considered a bosonic system described by two separate interactions with different coupling constants. The total energy is the sum of the two contributions: if the two interactions have the same sign, then the system just goes back to the situation previously described. The key ingredient is to deal with two competing interactions [34], one repulsive (with coupling constant $g > 0$) and the other attractive ($g' < 0$), so that the total energy of a uniform system becomes

$$\frac{E}{V} = \frac{1}{2} \delta g \rho^2 + \alpha'_{\mathrm{LHY}} (g \rho)^{5/2} \tag{2.5}$$

where $\delta g = g + g'$ and α'_{LHY} is a positive constant that depends only on the ratio g'/g. When g and g' are of the same order and $g' < -g$, the mean field term (proportional to ρ^2) is attractive, while the LHY correction (proportional to $\rho^{5/2}$) is repulsive. The final energy as a function of density is represented by the black curve in Figure 2.2: it reaches a minimum at a finite value of ρ as a result of the balance between the mean field attraction, dominant at low densities, and the beyond-mean field repulsion at higher densities. This competition is crucial to allow the formation of self-bound *quantum droplets*. These states share some of the peculiar properties of a liquid, even if their characteristic density (that is clearly higher than the one of the gaseous phase) is several orders of magnitude lower than in ordinary liquids.
Petrov proposed [5] to consider a mixture of two types of bosons where atoms of the same species repel each other with a given coupling constant, while atoms of different species attract each other with a different coupling constant: these systems are investigated in details in the following section.

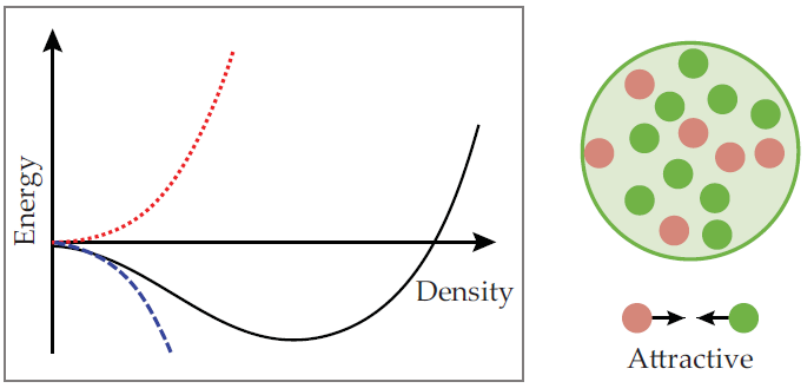

Figure 2.2: Bose-Einstein condensates of atomic mixtures can have attractive and repulsive interactions. If the mean field energy (blue dashed line) and the LHY correction (red dashed line) have opposite signs, the total energy (black solid line) can develop a minimum at finite density: atoms can form self-bound liquid droplets. Figure taken from [34].

The first observation of a two-component liquid phase was realized with a mixture of two hyperfine states of ^{39}K, namely $|F = 1, m_F = 0\rangle$ and $|F = 1, m_F = -1\rangle$: this result was achieved by two teams, one led by L. Tarruell at the ICFO [6], and the other by M. Fattori at the University of Florence [7].
It is important to mention that the first evidences of self-bound liquid droplets were found in single-species BEC made of magnetic atoms, where the repulsive contact interaction is accompanied by an anisotropic longer-ranged dipole-dipole interaction: when atoms are mostly distributed head-to-tail, the dipole interaction is responsible for the same competition that arises in two-species systems. The aforementioned T. Pfau's group worked with Dy atoms [35], characterized by a large magnetic moment; after that, some experiments realized at the University of Innsbruck, under the direction of F. Ferlaino, showed the same stabilization with Er atoms [36].

2.2 Two-component Bose-Einstein condensates

Let's consider a uniform Bose-Bose mixture with two components with masses m_1, m_2 inside a volume V. The two species interact with coupling constants

$$g_{ii} = \frac{4\pi\hbar^2}{m_i} a_{ii} \qquad (i = 1, 2) \qquad\qquad g_{12} = \frac{2\pi\hbar^2}{m_r} a_{12} \tag{2.6}$$

where $m_r = m_1 m_2/(m_1 + m_2)$ is the reduced mass. The intraspecies s-wave scattering lengths a_{11}, a_{22} are positive (repulsive interaction), while the interspecies one a_{12} can be positive or negative (attractive interaction).
In this thesis work we study the case of a ^{41}K-^{87}Rb mixture with the following values for the intraspecies scattering lengths:

$$\begin{aligned} a_{11} &= 65\, a_0 \\ a_{22} &= 100.4\, a_0 \end{aligned} \tag{2.7}$$

Here and in the following we are using atomic units (a.u.): $\hbar = e = m_e = 1$. Lengths are thus measured in units of the Bohr radius a_0, while energies are expressed in Hartree (1 Ha = 27.2 eV). Moreover, ^{41}K is denoted as the first species and it is labelled by the index 1, while ^{87}Rb is the second species, labelled by the index 2.

Using a DFT approach [5, 16], a binary Bose mixture admits as order parameters two complex wave functions ψ_1, ψ_2, one for each species, that are related to the local densities through

$$\rho_i(\vec{r}) = |\psi_i(\vec{r})|^2 \qquad\qquad \int_V d\vec{r}\, |\psi_i(\vec{r})|^2 = N_i \qquad\qquad (i = 1, 2) \tag{2.8}$$

being N_i the number of atoms of the i^{th} species.
The total energy of the system is given by

$$E = \int_V d\vec{r}\, \mathcal{E}(\rho_1, \rho_2) \tag{2.9}$$

where the energy density is evaluated at the local densities $\rho_1(\vec{r})$, $\rho_2(\vec{r})$:

$$\mathcal{E}(\rho_1, \rho_2) = \frac{\hbar^2}{2m_1}|\vec{\nabla}\psi_1|^2 + \frac{\hbar^2}{2m_2}|\vec{\nabla}\psi_2|^2 + \frac{1}{2}\, g_{11}\, \rho_1^2 + \frac{1}{2}\, g_{22}\, \rho_2^2 + g_{12}\, \rho_1\, \rho_2 + \mathcal{E}_{\mathrm{LHY}} \tag{2.10}$$

The first contribution in Eq. (2.10) comes from the kinetic energy term

$$\mathcal{E}_{\mathrm{KIN}} = \sum_{i=1}^{2} \frac{\hbar^2}{2m_i}|\vec{\nabla}\psi_i|^2 \tag{2.11}$$

that accounts for the spatial variations of the densities.

The second term in Eq. (2.10) is the mean field (MF) contribution

$$\begin{aligned} \mathcal{E}_{\mathrm{MF}} &= \frac{1}{2}\, g_{11}\, \rho_1^2 + \frac{1}{2}\, g_{22}\, \rho_2^2 + g_{12}\, \rho_1\, \rho_2 \\ &= \frac{1}{2}\left(\rho_1 \sqrt{g_{11}} - \rho_2 \sqrt{g_{22}}\right)^2 + \delta g\, \rho_1\, \rho_2 \end{aligned} \tag{2.12}$$

where we have introduced the parameter

$$\delta g = g_{12} + \sqrt{g_{11} g_{22}} \tag{2.13}$$

First of all, the stability of the system requires the first term in Eq. (2.12) to be zero, locking the ratio between the densities to the so called *MF optimal ratio* predicted by Petrov [5]:

$$\frac{\rho_1}{\rho_2} = \sqrt{\frac{g_{22}}{g_{11}}} \simeq 0.85 \tag{2.14}$$

The value of g_{12} is not fixed, but it can be experimentally tuned by means of Feshbach resonances (more details can be found in [8]). This allows to explore a wide range of the interspecies coupling constant, where three different regimes can be identified:

- if all interactions are repulsive and $g_{12} > \sqrt{g_{11} g_{22}}$ we have the **immiscible region** where the two species are not spatially overlapping;
- if $-\sqrt{g_{11} g_{22}} < g_{12} < \sqrt{g_{11} g_{22}}$ we have the **miscible region** where the interspecies interaction is weak and the two species are almost the same of a single-species BEC;
- if $g_{12} < -\sqrt{g_{11} g_{22}}$, i.e. $\delta g < 0$, the energy is minimized for $\rho_1, \rho_2 \to \infty$, meaning that the condensate collapses: this is the **mean field collapse region**. For the ^{41}K-^{87}Rb mixture, the critical value of the interspecies scattering length, in correspondence of which $\delta g = 0$, is:

$$a_{12,c} = -75.4\, a_0 \tag{2.15}$$

Figure 2.3(a) shows the calculated value of a_{12} as a function of the magnetic field B in a range between two Feshbach resonances: increasing the field from 60 to 78 G, all the three regimes can be explored. The effects of the interactions can be observed by means of absorption images of the expanding binary condensate, like the ones in Figure 2.3(b). The first column corresponds to the immiscible region at $a_{12} \simeq 255\, a_0$: the two clouds repel each other as a consequence of strong repulsive intraspecies interactions. The second column shows the miscible region at $a_{12} \simeq 10\, a_0$: here the two clouds weakly interact during the expansion, so that the density distributions do not differ from the ones of a single-species BEC.

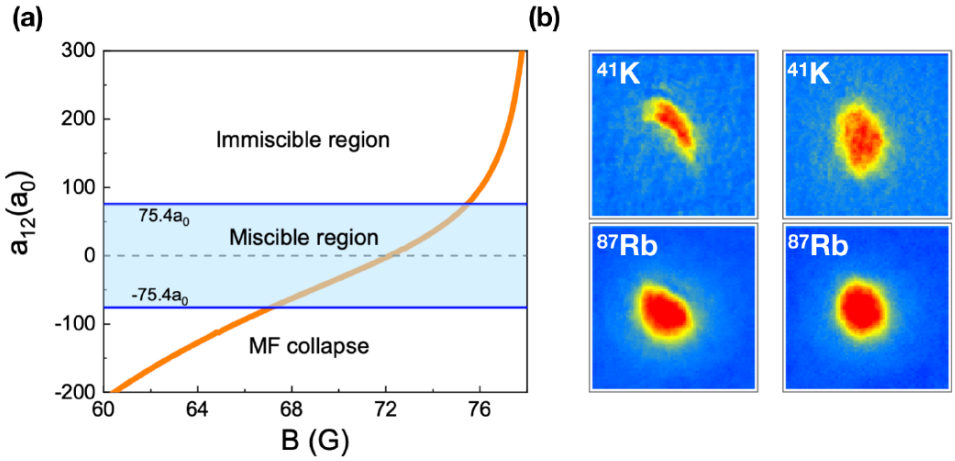

Figure 2.3: (a) Calculated interspecies scattering length for a $^{41}\mathrm{K} - {}^{87}\mathrm{Rb}$ mixture as a function of the applied magnetic field. (b) Absorption images of the binary BEC in the immiscible (first column) and miscible (second column) regions. Figure taken from [37].

The last term of Eq. (2.10) is the beyond-mean field (BMF) correction $\mathcal{E}_{\mathrm{LHY}}$ that encodes purely quantum fluctuations through the Lee-Huang-Yang (LHY) mechanism [9]. This is a repulsive term that, in the MF collapse region, counterbalances the MF attractive one: as explained in details in the previous section, the competition between the MF ($\mathcal{E}_{\mathrm{MF}} \propto \rho^2 < 0$) and the LHY ($\mathcal{E}_{\mathrm{LHY}} \propto \rho^{5/2} > 0$) contributions gives rise to the formation of self-bound droplets. From now on we mainly work in the *self-bound regime* given by:

$$\delta g < 0 \qquad \longleftrightarrow \qquad a_{12} < a_{12,c} \tag{2.16}$$

The explicit expression for a binary Bose mixture was carried out by D. Larsen in [38] and it reads:

$$\mathcal{E}_{\mathrm{LHY}} = \frac{8}{15\pi^2}\left(\frac{m_1}{\hbar^2}\right)^{3/2}(g_{11}\,\rho_1)^{5/2}\, f\left(\frac{m_2}{m_1}, \frac{g_{12}^2}{g_{11}g_{22}}, \frac{g_{22}\rho_2}{g_{11}\rho_1}\right) \tag{2.17}$$

where $f > 0$ is a dimensionless function depending, in principle, on the interspecies scattering length and on the ratio between densities.

Assuming the *MF optimal ratio* of Eq. (2.14) to be valid everywhere, Eq. (2.10) becomes a functional of density ρ_1 alone:

$$\begin{aligned}\mathcal{E}(\rho_1) &= \frac{\hbar^2}{2}\left(\frac{1}{m_1} + \frac{1}{m_2}\sqrt{\frac{g_{11}}{g_{22}}}\right)|\vec{\nabla}\sqrt{\rho_1}|^2 + \left(g_{11} + g_{12}\sqrt{\frac{g_{11}}{g_{22}}}\right)\rho_1^2 + \mathcal{E}_{\mathrm{LHY}}(\rho_1) \\ &= \frac{\hbar^2}{8}\left(\frac{1}{m_1} + \frac{1}{m_2}\sqrt{\frac{g_{11}}{g_{22}}}\right)\frac{|\vec{\nabla}\rho_1|^2}{\rho_1} + \delta g\sqrt{\frac{g_{11}}{g_{22}}}\,\rho_1^2 + \mathcal{E}_{\mathrm{LHY}}(\rho_1)\end{aligned} \tag{2.18}$$

with the LHY energy correction given by:

$$\mathcal{E}_{\mathrm{LHY}}(\rho_1) = \frac{8}{15\pi^2}\left(\frac{m_1}{\hbar^2}\right)^{3/2} g_{11}^{5/2}\, f\left(z = \frac{m_2}{m_1},\ u = \frac{g_{12}^2}{g_{11}g_{22}},\ x = \sqrt{\frac{g_{22}}{g_{11}}}\right)\rho_1^{5/2} \tag{2.19}$$

The most complicated part inside this expression is represented by the explicit form of the positive dimensionless function $f(z,u,x)$. The first thing to notice, as shown in [5], is that this function is weakly dependent on u, so it can be replaced by its value in correspondence of the MF collapse, where $\delta g = 0$, i.e. $u = 1$. $f(z,1,x)$ has a simple analytical expression [5] in the particular case of equal masses, while in the more general case of heteronuclear mixtures ($m_1 \neq m_2$) it is given by:

$$f(z,1,x) = \frac{15}{32}\int_0^\infty k^2 \mathcal{F}(k,z,x)\,dk \tag{2.20}$$

where the form of the function $\mathcal{F}(k,z,x)$ can be found in [39].
The numerical integral appearing in Eq. (2.20) can be parametrized by a simpler analytical formula that reproduces in an accurate way the behaviour of the numerical curve in the limited domain of the parameter x we are interested in. In particular, for our ^{41}K-^{87}Rb mixture with fixed $z = \frac{m_2}{m_1} \simeq 2.1$, we are interested in the value of the function f at $x = \sqrt{\frac{g_{22}}{g_{11}}} \simeq 0.85$. In this region of interest, $f(z = 2.1, u = 1, x)$ is interpolated by the following polynomial function:

$$f(x) = 1 + a\,x + b\,x^2 + c\,x^3 + d\,x^{3/2} \tag{2.21}$$

The parameters of the fit are:

a	5.19 ± 0.03
b	7.53 ± 0.02
c	0.476 ± 0.001
d	-4.08 ± 0.05

Table 2.1: Fit parameters from the polynomial function in Eq. (2.21).

At this point, Eq. (2.18) can be rewritten in a clearer way as

$$\mathcal{E}(\rho_1) = \alpha \frac{|\vec{\nabla}\rho_1|^2}{\rho_1} + \beta\,\rho_1^2 + \gamma\,\rho_1^{5/2} \tag{2.22}$$

after introducing the constants

$$\begin{aligned} \alpha &= \frac{\hbar^2}{8}\left(\frac{1}{m_1} + \frac{1}{m_2}\sqrt{\frac{g_{11}}{g_{22}}}\right) \\ \beta &= \delta g \sqrt{\frac{g_{11}}{g_{22}}} < 0 \\ \gamma &= \frac{8}{15\pi^2}\left(\frac{m_1}{\hbar^2}\right)^{3/2} g_{11}^{5/2} f(z,1,x) > 0 \end{aligned} \tag{2.23}$$

2.3 The uniform system

Let's now focus on the analysis of some equilibrium thermodynamic properties of a uniform system made of a self-bound mixture of two species with densities ρ_1, ρ_2. In particular, we will derive general expressions for the total pressure and the isothermal compressibility without relying on the assumption of the *MF optimal ratio* between the two densities, given in Eq. (2.14).
As introduced in the previous section, the energy per unit volume of the uniform system is

$$\mathcal{E}(\rho_1,\rho_2) = \frac{E}{V} = \frac{1}{2}g_{11}\,\rho_1^2 + \frac{1}{2}g_{22}\,\rho_2^2 + g_{12}\,\rho_1\rho_2 + \mathcal{E}_{\mathrm{LHY}} \tag{2.24}$$

and the total energy is $E = \mathcal{E}\,V$.
The total pressure of the uniform system at $T = 0$ is given by:

$$P(\rho_1,\rho_2) = -\frac{dE}{dV} = -\frac{d}{dV}\left(V\,\mathcal{E}(\rho_1,\rho_2)\right) = -\mathcal{E} + \sum_{i=1,2}\rho_i\frac{\partial\mathcal{E}}{\partial\rho_i} \tag{2.25}$$

From Eq. (2.24) the derivatives are obtained in a straightforward way:

$$\begin{aligned} \frac{\partial\mathcal{E}}{\partial\rho_1} &= g_{11}\,\rho_1 + g_{12}\,\rho_2 + \frac{\partial\mathcal{E}_{\mathrm{LHY}}}{\partial\rho_1} \\ \frac{\partial\mathcal{E}}{\partial\rho_2} &= g_{22}\,\rho_2 + g_{12}\,\rho_1 + \frac{\partial\mathcal{E}_{\mathrm{LHY}}}{\partial\rho_2} \end{aligned} \tag{2.26}$$

The BMF term in the energy functional reads

$$\mathcal{E}_{\rm LHY}(\rho_1,\rho_2) = \frac{8}{15\pi^2}\left(\frac{m_1}{\hbar^2}\right)^{3/2} g_{11}^{5/2}\rho_1^{5/2} f\left(z=\frac{m_2}{m_1},\, u\simeq 1,\, x(\rho_1,\rho_2)=\frac{g_{22}}{g_{11}}\frac{\rho_2}{\rho_1}\right) \tag{2.27}$$

so that the derivatives appearing in Eq. (2.26) are:

$$\begin{aligned}\frac{\partial \mathcal{E}_{\rm LHY}}{\partial \rho_1} &= \frac{8}{15\pi^2}\left(\frac{m_1}{\hbar^2}\right)^{3/2} g_{11}^{5/2}\rho_1^{1/2}\left[\frac{5}{2}\rho_1 f - \frac{g_{22}\rho_2}{g_{11}}\frac{\partial f}{\partial x}\right]\\ \frac{\partial \mathcal{E}_{\rm LHY}}{\partial \rho_2} &= \frac{8}{15\pi^2}\left(\frac{m_1}{\hbar^2}\right)^{3/2} g_{11}^{3/2} g_{22}\rho_1^{3/2}\frac{\partial f}{\partial x}\end{aligned} \tag{2.28}$$

Putting everything together, the final expression for the total pressure is:

$$P(\rho_1,\rho_2) = \frac{1}{2}g_{11}\rho_1^2 + \frac{1}{2}g_{22}\rho_2^2 + g_{12}\rho_1\rho_2 - \mathcal{E}_{\rm LHY} + \rho_1\frac{\partial \mathcal{E}_{\rm LHY}}{\partial \rho_1} + \rho_2\frac{\partial \mathcal{E}_{\rm LHY}}{\partial \rho_2} \tag{2.29}$$

If the two densities satisfy the *MF optimal ratio* of Eq. (2.14), then the total pressure reduces to a function of the density of the first species alone:

$$P(\rho_1) = \beta\rho_1^2 - \gamma\rho_1^{5/2} + \frac{5}{2}\gamma\rho_1^{5/2} = \rho_1^2\left(\beta + \frac{3}{2}\gamma\rho_1^{1/2}\right) \tag{2.30}$$

At this point, the zero-pressure condition $P(\rho_1) = 0$ allows to determine the bulk densities of the droplets:

$$\begin{aligned}\rho_1^{(0)} &= \frac{25\pi}{1024}\frac{1}{a_{11}^3}\frac{\delta g^2}{g_{11}g_{22}} f^{-2}(z,1,x)\\ \rho_2^{(0)} &= \sqrt{\frac{g_{11}}{g_{22}}}\rho_1^{(0)}\end{aligned} \tag{2.31}$$

Notice that these are only approximated results that are useful to obtain an estimate of the value that densities reach at saturation in the droplet core, far from the surface. The exact bulk densities, for a given interparticle scattering length a_{12}, can be computed in a more refined way by means of the following numerical procedure [39]:

- *mechanical stability*: find the curve $P(\rho_1,\rho_2) = 0$ in the (ρ_1,ρ_2) plane using Eq. (2.29);
- *thermodynamic stability*: find the portion of plane where both chemical potentials $\mu_i = \frac{\partial \mathcal{E}}{\partial \rho_i}$, $i = 1,2$, are negative;
- *minimization of energy*: select the point $(\rho_1^{(b)},\rho_2^{(b)})$ which satisfies the previous conditions and for which the energy per particle $E/N = \mathcal{E}/\rho$ is minimum.

In the following we will denote with the apex (0) the approximate theoretical results for the bulk densities, while the apex (b) refers to the numerical values obtained with this procedure.

Another important thermodynamic quantity is the bulk modulus κ that is defined as the inverse of the isothermal compressibility:

$$\kappa = -V\frac{\partial P(\rho_1,\rho_2)}{\partial V} = -V\sum_{i=1,2}\frac{\partial \rho_i}{\partial V}\frac{\partial P}{\partial \rho_i} = \sum_{i=1,2}\rho_i\frac{\partial P}{\partial \rho_i} \tag{2.32}$$

Computing the derivatives of the total pressure, using Eq. (2.29)

$$\begin{aligned}\frac{\partial P}{\partial \rho_1} &= g_{11}\rho_1 + g_{12}\rho_2 + \rho_1\frac{\partial^2 \mathcal{E}_{\rm LHY}}{\partial \rho_1^2} + \rho_2\frac{\partial^2 \mathcal{E}_{\rm LHY}}{\partial \rho_1\partial \rho_2}\\ \frac{\partial P}{\partial \rho_2} &= g_{22}\rho_2 + g_{12}\rho_1 + \rho_1\frac{\partial^2 \mathcal{E}_{\rm LHY}}{\partial \rho_1\partial \rho_2} + \rho_2\frac{\partial^2 \mathcal{E}_{\rm LHY}}{\partial \rho_2^2}\end{aligned}$$

and exploiting Eq. (2.28)

$$\frac{\partial^2 \mathcal{E}_{\rm LHY}}{\partial \rho_1^2} = \frac{8}{15\pi^2}\left(\frac{m_1}{\hbar^2}\right)^{3/2} g_{11}^{5/2}\left[\frac{15}{4}\rho_1^{1/2} f - 3\frac{g_{22}}{g_{11}}\frac{\rho_2}{\rho_1^{1/2}}\frac{\partial f}{\partial x} + \frac{g_{22}^2}{g_{11}^2}\frac{\rho_2^2}{\rho_1^{3/2}}\frac{\partial^2 f}{\partial x^2}\right]$$
$$\frac{\partial^2 \mathcal{E}_{\rm LHY}}{\partial \rho_2^2} = \frac{8}{15\pi^2}\left(\frac{m_1}{\hbar^2}\right)^{3/2} g_{11}^{1/2} g_{22}^2 \rho_1^{1/2}\frac{\partial^2 f}{\partial x^2}$$
$$\frac{\partial^2 \mathcal{E}_{\rm LHY}}{\partial \rho_1 \partial \rho_2} = \frac{8}{15\pi^2}\left(\frac{m_1}{\hbar^2}\right)^{3/2} g_{11}^{5/2}\rho_1^{1/2}\left[\frac{3}{2}\frac{g_{22}}{g_{11}}\frac{\partial f}{\partial x} - \frac{g_{22}^2}{g_{11}^2}\frac{\rho_2}{\rho_1}\frac{\partial^2 f}{\partial x^2}\right]$$

one finds the final expression for the bulk modulus of an homogeneous Bose-Bose mixture:

$$\kappa \;=\; g_{11}\,\rho_1^2 \;+\; g_{22}\,\rho_2^2 \;+\; 2\,g_{12}\,\rho_1\,\rho_2 \;+\; \frac{15}{4}\,\mathcal{E}_{\rm LHY} \tag{2.33}$$

In the specific case where the densities of the two species satisfy the *MF optimal ratio*, the bulk modulus reduces to:

$$\kappa \;=\; 2\,\beta\,\rho_1^2 \;+\; \frac{15}{4}\,\gamma\,\rho_1^{5/2} \tag{2.34}$$

2.4 Gross-Pitaevskii equations

The ground state of the system is obtained by a functional minimization of the total energy in Eq. (2.9), subjected to the constraint of keeping fixed the total number of particles of each species (N_1, N_2): this well known procedure will give, as a result, the Euler-Lagrange equations of the system.

Starting with the variation of the total energy, one has:

$$\begin{aligned}\delta E \;=\; \int d\vec{r}\,\Bigg\{ &\left[-\frac{\hbar^2}{2m_1}\,\vec{\nabla}^2\psi_1 \;+\; \left(\frac{\partial \mathcal{E}_{\rm LHY}}{\partial \rho_1} + g_{11}\,\rho_1 + g_{12}\,\rho_2\right)\psi_1\right]\delta\psi_1^* \;+ \\ &+\left[-\frac{\hbar^2}{2m_2}\,\vec{\nabla}^2\psi_2 \;+\; \left(\frac{\partial \mathcal{E}_{\rm LHY}}{\partial \rho_2} + g_{22}\,\rho_2 + g_{12}\,\rho_1\right)\psi_2\right]\delta\psi_2^*\Bigg\}\end{aligned} \tag{2.35}$$

while the variation of total number of particles for each species ($i = 1, 2$) reads:

$$\delta N_i \;=\; \int d\vec{r}\,\psi_i\,\delta\psi_i^* \tag{2.36}$$

The final solution of the functional minimization subject to constraints

$$\delta(E \;-\; \mu_1\,N_1 \;-\; \mu_2\,N_2) \;\stackrel{!}{=}\; 0$$

where the chemical potentials μ_1, μ_2 play the role of Lagrange multipliers, is provided by the following set of coupled stationary Gross-Pitaevskii (GP) equations:

$$\begin{aligned}\left[-\frac{\hbar^2}{2m_1}\,\vec{\nabla}^2 \;+ V_1(\rho_1,\rho_2)\right]\psi_1(\vec{r}) \;&=\; \mu_1\,\psi_1(\vec{r}) \\ \left[-\frac{\hbar^2}{2m_2}\,\vec{\nabla}^2 \;+ V_2(\rho_1,\rho_2)\right]\psi_2(\vec{r}) \;&=\; \mu_2\,\psi_2(\vec{r})\end{aligned} \tag{2.37}$$

The effective potentials include both the usual mean field term and the LHY correction

$$V_i(\rho_1,\rho_2) \;=\; g_{ii}\rho_i \;+\; g_{ij}\,\rho_j \;+\; \frac{\partial \mathcal{E}_{\rm LHY}}{\partial \rho_i} \qquad\qquad i \neq j \tag{2.38}$$

where the derivatives of the LHY functional can be read in Eq. (2.28).

The self-consistent solutions of the above equations allow to find the ground-state of the system (or stationary states in the corotating frame, as it will be shown in the following). The real-time dynamics of the system can be computed as well by solving the associated time-dependent GP equations [8, 40]:

$$\begin{aligned} i\hbar\,\frac{\partial\psi_1(\vec{r},t)}{\partial t} &= \left[-\frac{\hbar^2}{2m_1}\vec{\nabla}^2 + V_1(\rho_1,\rho_2) + U_1(\vec{r}) - i\hbar\frac{K_3}{2}|\psi_2(\vec{r},t)|^4\right]\psi_1(\vec{r},t) \\ i\hbar\,\frac{\partial\psi_2(\vec{r},t)}{\partial t} &= \left[-\frac{\hbar^2}{2m_2}\vec{\nabla}^2 + V_2(\rho_1,\rho_2) + U_2(\vec{r}) - i\hbar K_3|\psi_1(\vec{r},t)|^2\,|\psi_2(\vec{r},t)|^2\right]\psi_2(\vec{r},t) \end{aligned} \tag{2.39}$$

The two new terms appearing in the Hamiltonians of Eq. (2.39) take into account the presence of an external potential $U_{1,2}$ acting on the two species (for instance, an harmonic trap to achieve confinement properties) and also the effect of three-body losses: they are included adding to the starting total energy a dissipative contribution

$$\int d\vec{r}\,\left[-\frac{i}{2}\hbar K_3\,\rho_1(\vec{r},t)\,\rho_2^2(\vec{r},t)\right]$$

(with $K_3 = 7\times10^{-41}$ m^6/s, see [8] for further details) describing the dominant recombination channel K-Rb-Rb. Few more comments about this phenomenon can be found in the next Chapter.

The solutions of the set of coupled GP equations are computed numerically: the ground-state configurations come out from an imaginary time evolution of Eqs. (2.37), while the dynamics of the system is studied solving Eqs. (2.39) in real time. More precise details about the simulation domain and the numerical methods that are employed can be found in Appendix B.

Chapter 3

Surface properties of a self-bound droplet

The appearance of self-bound droplets implies the existence of a surface energy, hence a surface tension associated to it. In this chapter we will discuss the surface properties of a ^{41}K-^{87}Rb self-bound droplet, starting from the determination of the surface tension σ_0 in the planar approximation, i.e. working with the so-called "slab" geometry. The surface of a droplet, however, is not planar, so curvature effects cannot be neglected. They are introduced by the Tolman's length δ that will be derived in two different ways: from a simple thermodynamical approach and using the liquid drop model (LDM). With the knowledge of σ_0 and δ, the correct value of the surface tension σ will be obtained. After that, we will briefly analyze the behaviour of density profiles for different values of the interspecies scattering length a_{12}. Surface tension plays an important role in the droplet stability: in the last part the critical number of particles above which the droplet is stable is computed as a function of a_{12}.

3.1 Planar approximation

As explained in [39], the surface tension of a fluid planar free surface is determined along the saturation line of the liquid-vapor (or liquid-liquid) two-phase equilibrium. In this particular case, since the mixture is at zero temperature, it corresponds to the $P = 0$ point. Furthermore, the computation can be simplified by working with the so called "slab" geometry that is characterized by a uniform density in the x-y plane and two "liquid"-vacuum planar interfaces perpendicular to the z axis. The "liquid" phase corresponds to a self-bound mixture of species 1 and 2 whose densities $\rho_1^{(0)}$, $\rho_2^{(0)}$ in the bulk region of the slab are determined by the equilibrium conditions discussed in Chapter 2: more details about the "slab" geometry can be found in Appendix B.
From thermodynamics, the total energy of the binary Bose mixture is:

$$\begin{aligned} E &= T\,S - P\,V + \sigma\,\mathcal{A} + \mu_1\,N_1 + \mu_2\,N_2 \\ &= \sigma\,\mathcal{A} + \mu_0\,N_1 \end{aligned} \tag{3.1}$$

where we assumed that the system is at $T = 0 = P$ and that only one species is a variable, the second one being fixed by Eq. (2.14). $\mathcal{A}$ is the free-surface area in the x-y plane, while μ_0 is the saturated "bulk" value of the chemical potential: its explicit expression, given by Eq. (C.8), is derived in Appendix C during the discussion of the density profile of a quantum droplet at the liquid-vacuum interface.
In order to take care of the fact we are working in a planar geometry, the surface tension is denoted

as σ_0. Its explicit expression can be found out exploiting Eqs. (2.22, C.10, C.11):

$$\begin{aligned}\sigma_0 =& \frac{1}{\mathcal{A}}(E-\mu_0 N_1) = \frac{1}{\mathcal{A}}\int d\vec{r}(\mathcal{E}-\mu_0\rho_1)\\ =& \frac{1}{\mathcal{A}}\underbrace{\int dx\,dy}_{\mathcal{A}}\int_{-\infty}^{+\infty} dz\,[\mathcal{E}(\rho_1(z))-\mu_0\rho_1(z)]\\ =& \int_{\rho_1^{(0)}}^{0}\frac{d\rho_1}{h(\rho_1)}\,[\mathcal{E}(\rho_1)-\mu_0\rho_1] = \int_0^{\rho_1^{(0)}} d\rho_1\sqrt{\frac{\alpha}{\rho_1}}\frac{2\left(\beta\rho_1^2+\gamma\rho_1^{5/2}-\mu_0\rho_1\right)}{\left(\beta\rho_1^2+\gamma\rho_1^{5/2}-\mu_0\rho_1\right)^{1/2}}\end{aligned} \tag{3.2}$$

Finally:

$$\sigma_0 = 2\int_0^{\rho_1^{(0)}} d\rho\,\sqrt{\alpha}\,\left(\beta\rho+\gamma\rho^{3/2}-\mu_0\right)^{1/2} \tag{3.3}$$

Notice that to compute the surface tension no information about the profile of the interface is required.
The "planar" surface tension is computed by solving numerically the integral in Eq. (3.3) for different values of the interspecies scattering length a_{12}: the results are shown in Figure 3.1.

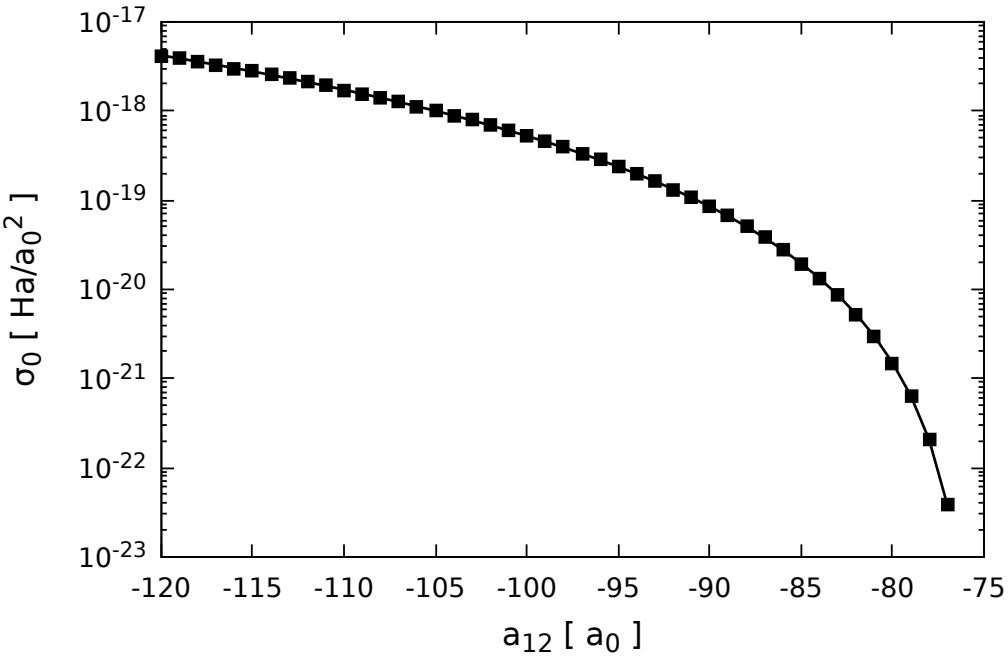

Figure 3.1: Calculated surface tension (in the "slab" geometry approximation) of the self-bound systems for the ^{41}K-^{87}Rb mixture as a function of a_{12}.

3.2 Curvature correction to surface tension: the Tolman length

The finite curvature of the droplet actually introduces a correction in the surface tension that is given by:

$$\sigma \simeq \sigma_0\left(1-\frac{2\delta}{R}\right) \tag{3.4}$$

where R is the typical radius of the droplet and σ_0 is the just computed surface tension in the planar interface approximation (the situation appears clear looking at Figure 3.2).
The new quantity δ is the Tolman length [41]: it provides the correction to the surface tension for a

curved interface up to the first order in the curvature.

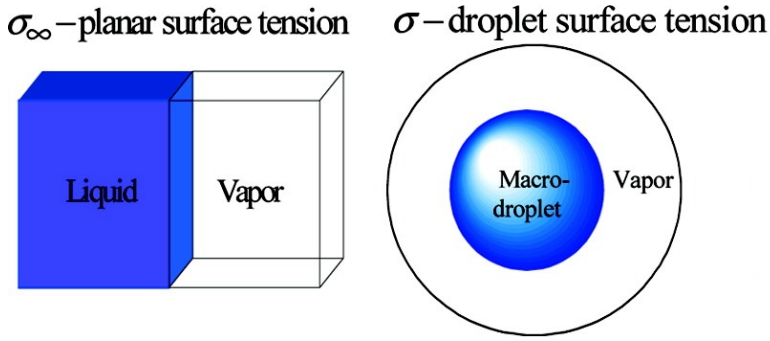

Figure 3.2: The left figure is a schematic representation of the planar model based on a "slab" geometry: the planar approximation σ_∞ for the surface tension is denoted, in the text, as σ_0.
The right figure shows the actual liquid-vapor interface for a droplet whose surface tension is affected by a finite curvature. The image is taken from [42].

As represented in Figure 3.3, the Tolman length should be negative if the interface of the droplet tends to curve towards the liquid phase, while it is positive in the opposite situation.

In the following we will provide two methods to compute the Tolman length and, therefore, to correctly estimate the surface tension σ.

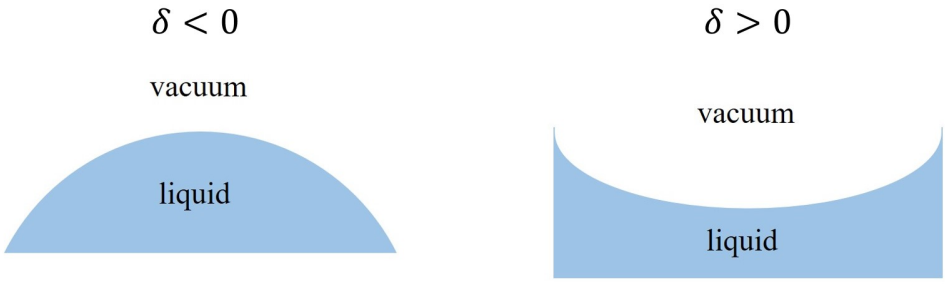

Figure 3.3: The Tolman length δ is negative if the interface tends to curve towards the liquid phase (left), while it is positive for interfaces that tend to curve towards the vacuum phase (right).

3.2.1 Thermodynamic expression for the Tolman length

A thermodynamic argument [43, 44] relates the Tolman length to the isothermal compressibility κ^{-1} through the following expression:

$$\delta \simeq -\kappa^{-1}\sigma_0 \tag{3.5}$$

Previously, some studies have noticed that the product $\kappa^{-1}\sigma_0$ is a fundamental characteristic length in liquid droplets [45–49], however the connection with the Tolman length was never explicitly made.
The expression for the compressibility is the one obtained in Chapter 2 during the analysis of the uniform system. In particular, since the two densities are assumed to satisfy the *MF optimal ratio*, it is obtained by taking the inverse of Eq. (2.34):

$$\kappa^{-1} = \left(2\beta\rho_1^2 + \frac{15}{4}\gamma\rho_1^{5/2}\right)^{-1} \tag{3.6}$$

In Figure 3.4 the compressibility κ^{-1} is represented as a function of the interspecies scattering length a_{12} in the self-bound droplet regime.

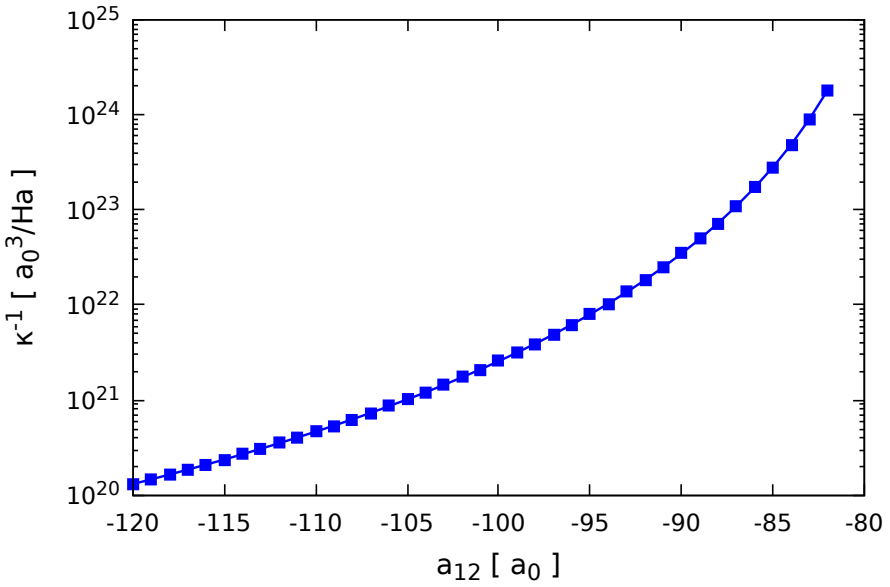

Figure 3.4: Numerical results for the isothermal compressibility as a function of the interspecies scattering length a_{12}.

With these values of the compressibility and the planar surface tension previously computed, the Tolman length is estimated by means of Eq. (3.5) for different values of a_{12}: the results are shown in Figure 3.5. As one can read in the legend, the green dots stand for the results of the computations explained in this section. The red triangles are the estimates of the Tolman length computed for four different values of a_{12} exploiting the liquid drop model: this procedure is explained in detail in the next section.

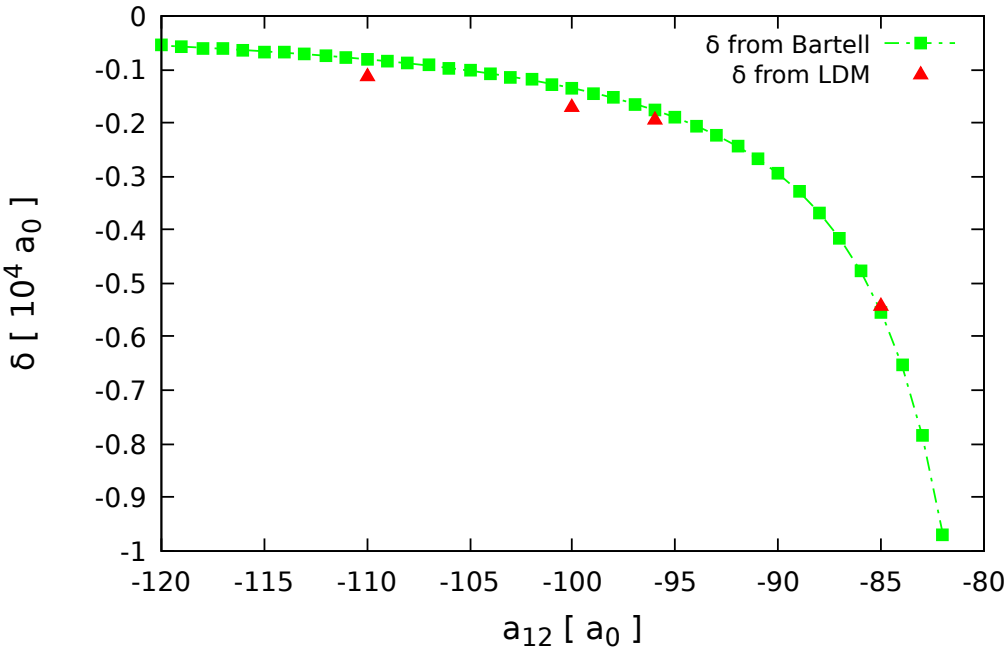

Figure 3.5: Numerical results for the Tolman length as a function of the interspecies scattering length a_{12}.

3.2.2 Liquid drop model

The total energy of the droplet can be decomposed into the sum of three contributions:

$$E = E_{\text{bulk}} + E_{\text{surface}} + E_{\text{curvature}} \tag{3.7}$$

The last two terms are directly computed using the explicit expression of Eq. (3.4), so that Eq. (3.7) can be equivalently written as:

$$\begin{aligned} & E_{\text{surface}} + E_{\text{curvature}} = 4\,\pi\,R^2\,\sigma = 4\,\pi\,R^2\,\sigma_0\left(1-\frac{2\delta}{R}\right) \\ \Rightarrow \quad & E = E_{\text{bulk}} + 4\,\pi\,R^2\,\sigma_0 + (-8\,\pi\,R\,\delta\,\sigma_0) \end{aligned} \tag{3.8}$$

The liquid drop model (LDM) provides a semi-empirical formula for the total energy of a droplet as a function of the number of particles N of the species it is made of:

$$E = E_b\,N + E_s\,N^{2/3} + E_c\,N^{1/3} \tag{3.9}$$

E_b, E_s and E_c are parameters that can be determined by a fit of experimental data.
The total number of atoms (under the assumption of a perfectly spherical droplet) is obtained from

$$N = \frac{4\,\pi}{3}\,R^3\,\rho^{(b)} \tag{3.10}$$

where $\rho^{(b)}$ is the total bulk density, that is actually a function of the interspecies scattering length:

$$\rho^{(b)} = \rho_1^{(b)} + \rho_2^{(b)} = \rho^{(b)}(a_{12}) \tag{3.11}$$

Combining Eq. (3.9) with Eq. (3.10) it is clear that in the LDM formula the bulk, surface and curvature contributions are separated:

$$E_b\,N \propto R^3 \sim E_{\text{bulk}} \qquad E_s\,N^{2/3} \propto R^2 \sim E_{\text{surface}} \qquad E_c\,N^{1/3} \propto R \sim E_{\text{curvature}} \tag{3.12}$$

In prevision of a fit of the numerical data, it is convenient to focus on the total energy per particle of a droplet, that is, from Eq. (3.9):

$$\begin{aligned} \frac{E}{N} &= E_b + E_s\,N^{-1/3} + E_c\,N^{-2/3} \\ &= E_b + E_s\,x + E_c\,x^2 \qquad\qquad \text{with} \qquad x \equiv N^{-1/3} \end{aligned} \tag{3.13}$$

Eq. (3.12) allows to obtain explicit expressions for the parameters E_c and E_s in terms of σ_0 and δ:

$$E_s = \frac{E_{\text{surface}}}{N^{2/3}} = 4\pi\left(\frac{R^3}{N}\right)^{2/3} = 4\pi\left(\frac{3}{4\pi\rho^{(b)}}\right)^{2/3}\sigma_0 \tag{3.14}$$

$$E_c = \frac{E_{\text{curvature}}}{N^{1/3}} = -8\pi\left(\frac{R^3}{N}\right)^{1/3}\delta\,\sigma_0 = -\,8\pi\left(\frac{3}{4\pi\rho^{(b)}}\right)^{1/3}\delta\,\sigma_0 \tag{3.15}$$

Finally, the Tolman length can be determined from the fit parameters without any knowledge of σ_0:

$$\delta(a_{12}) = -\,\frac{E_c}{2\,E_s}\left(\frac{3}{4\pi\rho^{(b)}(a_{12})}\right)^{1/3} \tag{3.16}$$

We can now make a summary of the procedure followed in order to compute the surface tension of a droplet using this *à la Tolman*-approach:

- the first step consists of computing the surface tension σ_0 in the planar ("slab" geometry) approximation (it was done in an analytical way);

- the total energy as a function of the number of atoms is obtained via droplet calculations, then a fit performed through the empirical relation given by the LDM (Eq. (3.13)) yields the parameters E_s, E_c;
- from the fit parameters, the Tolman length δ is obtained through Eq. (3.16);
- the surface tension is calculated via Eq. (3.4) for a given a_{12} and R.

In the following we will provide some specific examples for this approach, focusing on the last three steps.

3.2.3 Total energy and LDM fit

The total energy of the heteronuclear ^{41}K-^{87}Rb mixture in the droplet regime corresponds to the ground state energy that can be computed with a steepest descent algorithm, as explained in detail in Appendix B.
A series of Fortran routines was previously developed by a collaboration between researchers from the University of Padova and University of Barcelona to study the ground state properties and the dynamics of a Bose mixture via numerical evolutions both in imaginary and real time. This code is employed to determine the total energy of the system as a function of the number of particles $N = N_1 + N_2$ (we recall that 1 labels ^{41}K, while 2 is related to ^{87}Rb). This same procedure is repeated for four specific values of the interspecies scattering length:

$$a_{12} = [\,-85,\ -96,\ -100,\ -110\,]\,a_0$$

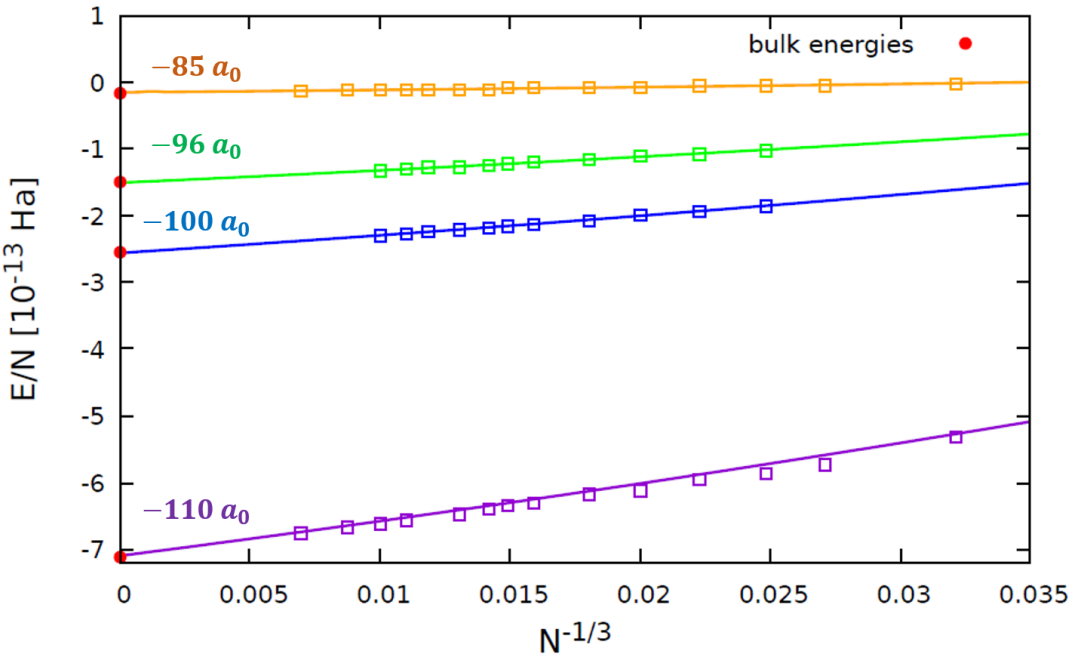

Figure 3.6: Energy per particle as a function of the total number of particles N for different values of the interspecies scattering length. Data are fitted within the LDM.

We are specifically interested in the energy per particle E/N, so it is important to look at what happens in the thermodynamic limit, when both the number of particles N and the volume V grow to infinity, but keeping their ratio constant. From the definition of thermodynamic limit itself, i.e. a regime with a constant density $\rho = N/V$, it appears clear that when $N \to \infty$ one is left with a uniform system. In this limit, the energy per particle corresponds to the bulk energy given by

$$\frac{E}{N} \xrightarrow{N\to\infty} \frac{E}{V}\frac{V}{N} = \frac{\mathcal{E}_{bulk}}{\rho^{(b)}} \tag{3.17}$$

where $\mathcal{E}_{bulk}$ is the energy density of the uniform system written in Eq. (2.24), while $\rho^{(b)} = \rho_1^{(b)} + \rho_2^{(b)}$ is the total bulk density.

Selecting the total number of particles inside the interval

$$N \in [3 \times 10^4, 3 \times 10^6]$$

the results of the numerical computations are presented in Figure 3.6, where the total energy per particle is plotted as a function of the quantity $N^{-1/3}$ in order to realize the parabolic fit in Eq. (3.13). Red dots stand for the bulk energies per particle of the system, for a given value of a_{12}, that were discussed above; solid lines are the result of the fit from the liquid drop model, whose parameters are collected in Table 3.1, together with the total bulk densities.

a_{12} [a_0]	$\rho^{(b)}$ [a_0^{-3}]	E_b [Ha]	E_s [Ha]	E_c [Ha]
-85	1.5525×10^{-10}	-1.501×10^{-14}	3.295×10^{-13}	2.991×10^{-12}
-96	7.1150×10^{-10}	-1.505×10^{-13}	1.759×10^{-12}	9.364×10^{-12}
-100	1.0218×10^{-9}	-2.559×10^{-13}	2.520×10^{-12}	1.330×10^{-11}
-110	2.0062×10^{-9}	-7.101×10^{-13}	4.990×10^{-12}	2.165×10^{-11}

Table 3.1: Total bulk density and parameters of the LDM fit given by Eq. (3.13) for different values of a_{12}.

At this point, the Tolman length for each interspecies scattering length can be estimated from Eq. (3.16). Both Table 3.2 and Figure 3.5 provide a direct comparison between the results of the LDM (red triangles) and the thermodynamic expression (Eq. (3.5)) derived by Bartell (green squares): it can be said that the two set of data present a good general agreement.

a_{12} [a_0]	-85	-96	-100	-110
δ [a_0] (**Bartell**)	-5530.979	-1761.518	-1350.061	-809.5488
δ [a_0] (**LDM**)	-5414.264	-1909.291	-1682.485	-1101.553

Table 3.2: Comparison between the results of the Tolman length computed with the thermodynamic expression from Bartell and with the LDM.

3.2.4 Final estimate of the surface tension

Once the Tolman length is computed, then the curvature correction to the surface tension can finally be realized, following Eq. (3.4).
First of all, let us rewrite the bulk radius in a slightly different fashion, starting from Eq. (3.10):

$$R = \left(\frac{3N}{4\pi\rho^{(b)}}\right)^{1/3} = r_0 N^{1/3} \qquad \text{with} \qquad r_0(a_{12}) \equiv \left(\frac{3}{4\pi\rho^{(b)}(a_{12})}\right)^{1/3} \tag{3.18}$$

This means that, for a fixed interspecies scattering length a_{12}, the surface tension is actually a function of the number of particles N:

$$\sigma \simeq \sigma_0 \left(1 - \frac{2\delta}{R}\right) = \sigma_0 \left(1 - \frac{2\delta}{r_0} N^{-1/3}\right) \tag{3.19}$$

The set of data (N, σ) is plotted in Figure 3.7, where dash-dotted lines represent the planar approximation σ_0. The surface tension increases as the absolute value of a_{12} becomes higher and, as expected from Eq. (3.19), it tends to σ_0 in the $N \to \infty$ limit. This same behaviour is confirmed by Figure 3.8: the ratio σ/σ_0 approaches the unitary value as N becomes higher and higher.

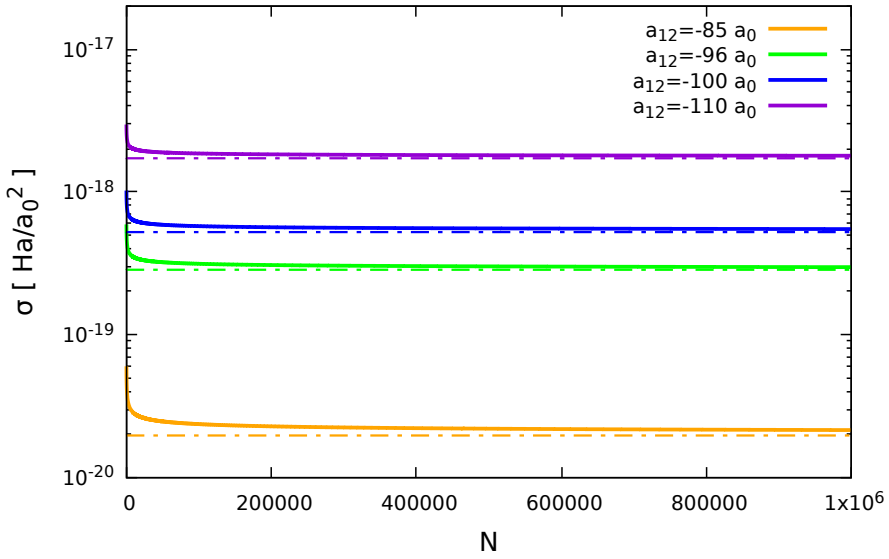

Figure 3.7: Final surface tension, σ, with the curvature correction as a function of the number of particles for different values of the interspecies scattering length. For each of them, dash-dotted lines correspond to the planar approximation of the surface tension.

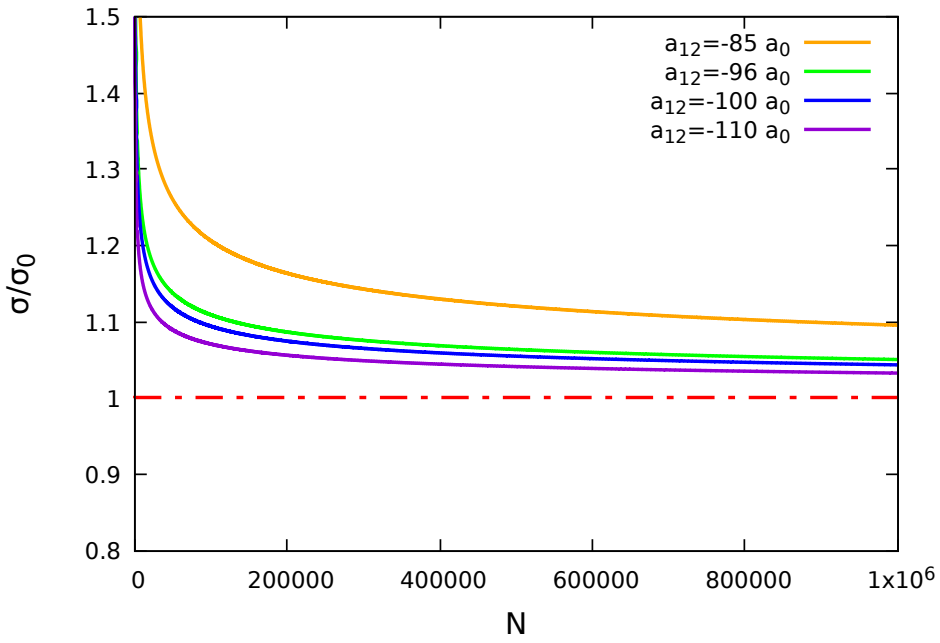

Figure 3.8: Ratio between the corrected value of the surface tension and the planar approximation as a function of the total number of particles.

3.3 Density profiles

We have also computed the ground state density profiles of the two species and, therefore, the total density of the mixture. These densities are actually functions of the three spatial coordinates: we consider, in the following, one-dimensional projections along one of the three directions (x, y or z) and two-dimensional projections onto a symmetry plane passing through the droplet center that is orthogonal to one of the Cartesian axes (x-y, x-z or y-z plane).
Once the total number of particles is fixed to $N = 50\,000$, five different computations are performed to determine the densities of the system for each value of a_{12}: the results for the bulk densities and the equilibrium radii are reported in Table 3.3, while the one- and two-dimensional density profiles are shown in Figures 3.9 - 3.13.

a_{12} $[a_0]$	$\rho_1^{(b)}$ $[a_0^{-3}]$	$\rho_2^{(b)}$ $[a_0^{-3}]$	N_1	N_2	N	R $[a_0]$
-85	7.210×10^{-11}	8.315×10^{-11}	23 221	26 779	50 000	42 522.60
-90	1.675×10^{-10}	1.917×10^{-10}	23 313	26 687	50 000	32 148.83
-95	3.033×10^{-10}	3.447×10^{-10}	23 404	26 596	50 000	26 409.76
-100	4.799×10^{-10}	5.418×10^{-10}	23 486	26 514	50 000	22 690.59
-105	6.980×10^{-10}	7.828×10^{-10}	23 569	26 431	50 000	20 050.37

Table 3.3: Bulk densities and equilibrium radii for quantum droplets with different values of a_{12}.

On the one hand, Eq. (2.31) tells that the bulk density is proportional to δg^2, therefore it grows when the interspecies scattering length a_{12} becomes more negative. On the other hand, from Eq. (3.18) one can see that $r_0 \propto {\rho^{(b)}}^{-1/3}$: this means that, for a fixed N, the bulk radius decreases as $|a_{12}|$ increases. These expectations are exactly confirmed by the numerical results: in fact going from $a_{12} = -85\,a_0$ to $a_{12} = -110\,a_0$ the density profiles become "higher" (consistently with the increasing of the bulk densities $\rho_1^{(b)}$, $\rho_2^{(b)}$) and "narrower" (consistently with the decreasing of the bulk radius R), in such a way to keep the integral constant to N.
As a final comment, the sigmoid shapes of the 1D projections confirm the droplet regime where bulk properties are dominant over surface ones, while the 2D projections make evident the spherical symmetry of the system allowing us to visualize the droplet in space.

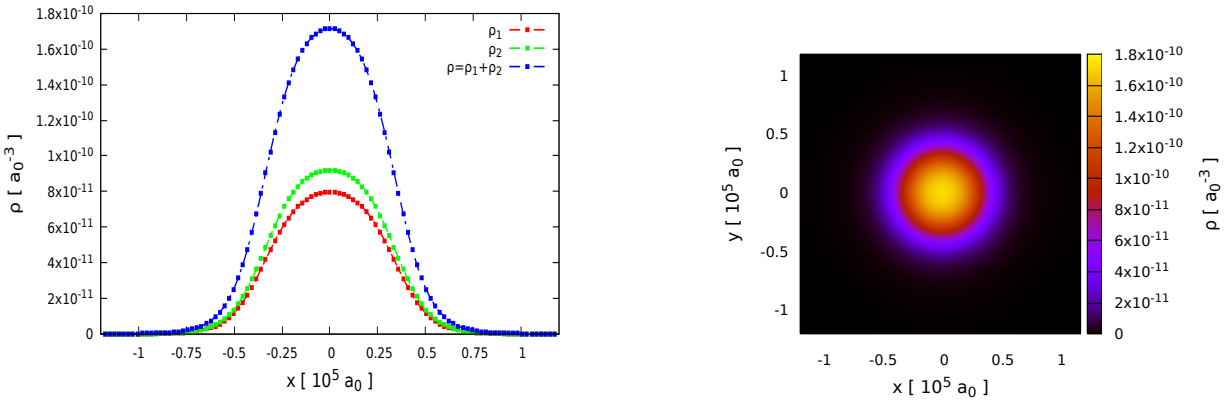

(a) Densities along the x direction.

(b) Density in the x-y plane passing through the droplet center.

Figure 3.9: One-dimensional and two-dimensional projections of the total density, in atomic units, for a droplet in free space with $a_{12} = -85\,a_0$

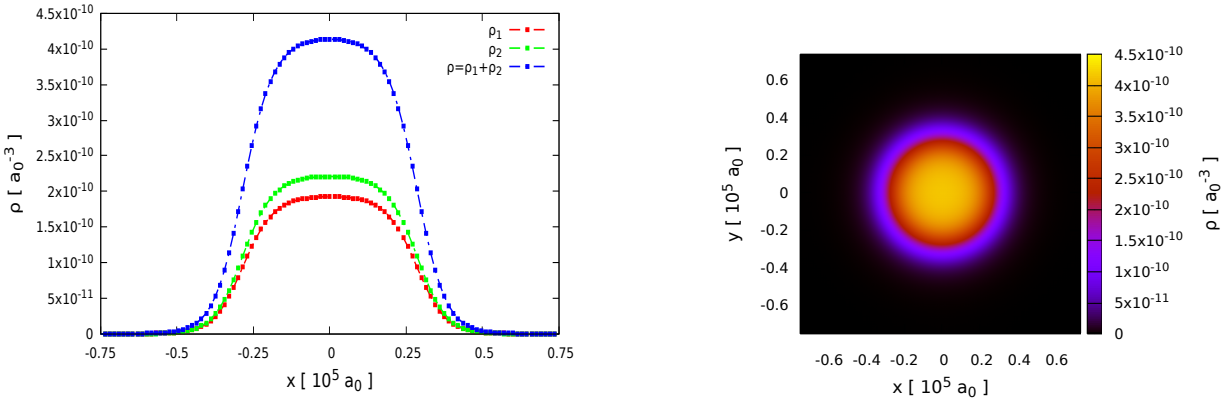

(a) Densities along the x direction.

(b) Density in the x-y plane passing through the droplet center.

Figure 3.10: One-dimensional and two-dimensional projections of the total density, in atomic units, for a droplet in free space with $a_{12} = -90\,a_0$.

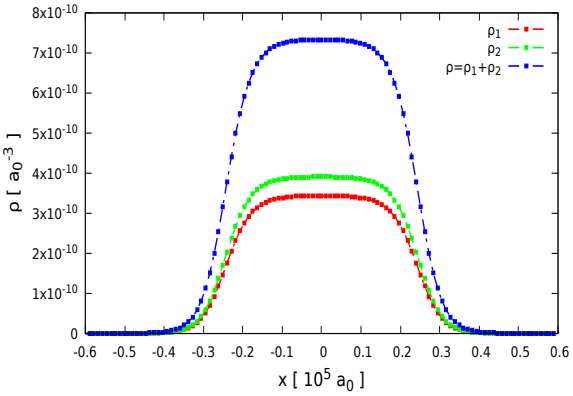

(a) Densities along the x direction.

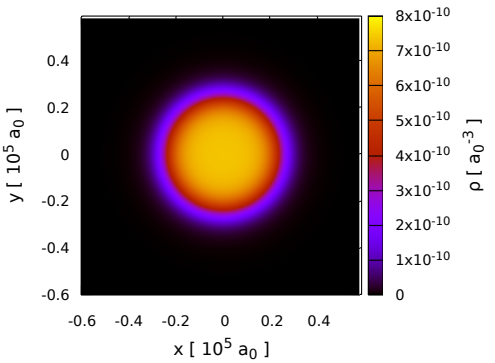

(b) Density in the x-y plane passing through the droplet center.

Figure 3.11: One-dimensional and two-dimensional projections of the total density, in atomic units, for a droplet in free space with $a_{12} = -95\,a_0$.

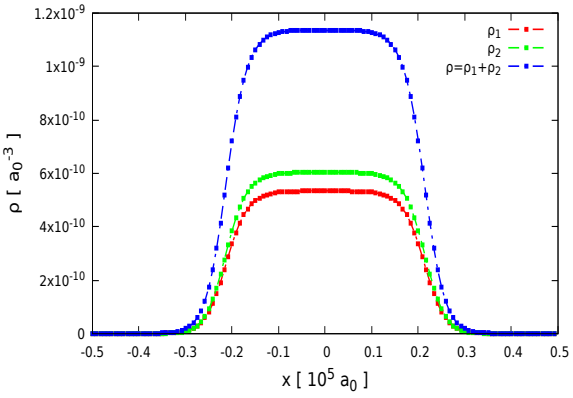

(a) Densities along the x direction.

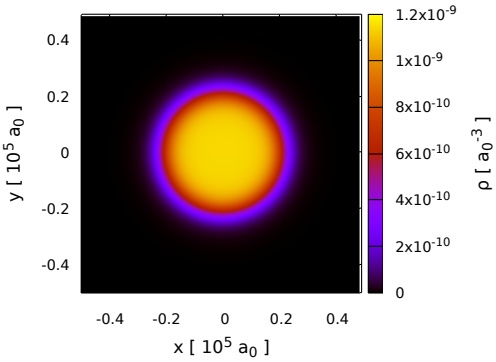

(b) Density in the x-y plane passing through the droplet center.

Figure 3.12: One-dimensional and two-dimensional projections of the total density, in atomic units, for a droplet in free space with $a_{12} = -100\,a_0$.

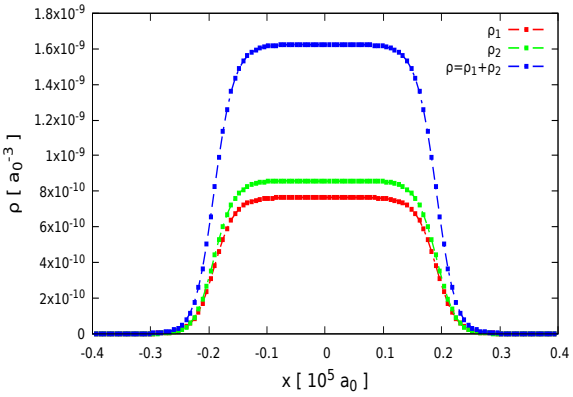

(a) Densities along the x direction.

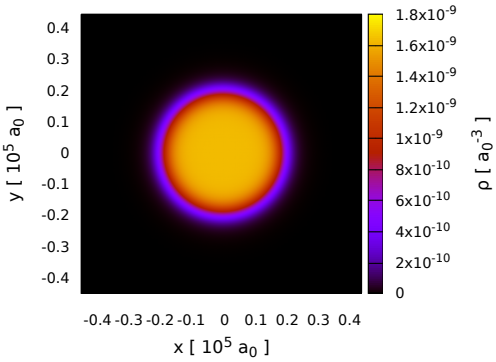

(b) Density in the x-y plane passing through the droplet center.

Figure 3.13: One-dimensional and two-dimensional projections of the total density, in atomic units, for a droplet in free space with $a_{12} = -105\,a_0$.

3.4 The critical number of particles for droplet stability

The density of any real liquid droplet is not uniform, but it increases from zero at the droplet's edge to a peak value at its center. In a dilute quantum liquid the density gradient at the surface acts as a surface tension that enters the Schroedinger equation in the kinetic energy terms. If the surface tension shifts the total energy from negative to positive, then the system cannot be self-bound anymore and the ground state is a gas: the kinetic energy can thus drive to a liquid-to-gas phase transition. As a result, not all values of the total number of atoms N are allowed for droplet formation: small droplets with N lower than a critical value N_c are unstable. An easy way to have an estimate of N_c for a given value of a_{12} is to perform a variatonal study. If we assume that in the critical region droplets have a gaussian-like density profile, we can use the following simple ansatz for the density of the first species:

$$\rho_1(r) = \frac{N_1}{\pi^{3/2}\,\sigma^3}\, e^{-\frac{r^2}{\sigma^2}} \tag{3.20}$$

It is normalized to the total number of particles N_1 of the selected species and the variance σ plays the role of variational parameter. This ansatz describes a so-called "all surface" droplet, since the density profile feels a dominant contribution from surface rather than from the bulk region that is not extended in space: this represents a good approximation of what happens near the evaporation threshold.
Under the assumption that the *MF optimal ratio* between densities is fixed everywhere, the energy functional is given by Eq. (2.22) and the total energy is obtained from:

$$E = \int d\vec{r} \left\{ 4\alpha \left(\frac{\partial \sqrt{\rho_1}}{\partial r} \right)^2 + \beta\, \rho_1^2 + \gamma\, \rho_1^{5/2} \right\} \tag{3.21}$$

Inserting the expression for $\rho_1(r)$ given in Eq. (3.20), the three contributions to the integral are:

- kinetic term

$$E_{\mathrm{KIN}} = 4\,\pi \int_0^\infty dr\, r^2\, 4\,\alpha \left(\frac{\partial}{\partial r} \sqrt{\rho_1(r)} \right)^2 = 6\alpha\, \frac{N_1}{\sigma^2} \tag{3.22}$$

- mean field term

$$E_{\mathrm{MF}} = 4\,\pi \int_0^\infty dr\, r^2\, \beta\, \rho_1^2(r) = \frac{\beta}{(2\pi)^{3/2}}\, \frac{N_1^2}{\sigma^3} \tag{3.23}$$

- beyond mean field term

$$E_{\mathrm{BMF}} = 4\,\pi \int_0^\infty dr\, r^2\, \gamma\, \rho_1^{5/2}(r) = \frac{\gamma}{\pi^{9/4}} \left(\frac{2}{5} \right)^{3/2} \frac{N_1^{5/2}}{\sigma^{9/2}} \tag{3.24}$$

Introducing the new parameters

$$a \equiv 6\alpha > 0 \qquad b \equiv \frac{\beta}{(2\pi)^{3/2}} < 0 \qquad c \equiv \frac{\gamma}{\pi^{9/4}} \left(\frac{2}{5} \right)^{3/2} > 0 \tag{3.25}$$

the effective single-component total energy can be explicitly written as a function of the number of atoms:

$$E = \frac{a}{\sigma^2}\, N_1 + \frac{b}{\sigma^3}\, N_1^2 + \frac{c}{\sigma^{9/2}}\, N_1^{5/2} \tag{3.26}$$

The variational parameter can be fixed to the value σ^*, for a given atom number N_1, by minimizing the energy per particle E/N_1. At the same time, we can identify the critical particle number $N_{1,c}$ as

the one below which the total energy is positive and so the system is not bound anymore: such value comes out from the condition of the separation line $E/N_1 = 0$
The coupled equations

$$\begin{cases} \frac{\partial}{\partial\sigma}\left(\frac{E}{N_1}\right)_{\sigma^*,N_{1,c}} &= 0 \\ \left(\frac{E}{N_1}\right)_{\sigma^*,N_{1,c}} &= 0 \end{cases} \tag{3.27}$$

are solved by:

$$N_{1,c} = -\frac{c}{\left(a+\frac{b}{\delta}\right)\delta^{5/2}} \qquad \sigma^* = -\frac{3\,b\,N_{1,c}}{5\,a} \tag{3.28}$$

where the parameter δ is defined by $\delta \equiv -3\,b\,/\,5\,a$.
This is the critical threshold for the number of atoms of the first component (^{41}K) of the mixture; since the ratio between the densities of the two species is fixed, $\rho_1/\rho_2 = (g_{22}/g_{11})^{1/2} \simeq 0.85$, the critical total number of atoms is simply

$$N_c = N_{1,c} + N_{2,c} = \left(1+\sqrt{\frac{g_{11}}{g_{22}}}\right) N_{1,c} \tag{3.29}$$

While the parameters α and γ are fixed by the species of the mixture (^{41}K, ^{87}Rb), β depends on δg, i.e. on a_{12}. The total number of atoms N and the parameter δg form a phase diagram where $N_c(\delta g)$ is the critical curve that marks a phase transition. This is represented by the black solid line in Figure 3.14: the region above the curve represents the stable droplet (liquid) phase, while systems that are located in the region below the curve are not able to form a self-bound state because evaporation processes will dominate destroying the self stability. A final summary of the regimes available to a ^{41}K-^{87}Rb mixture in free space is provided by Figure 3.15, where the total atom number is now represented as a function of the interspecies scattering length. The blue solid line denotes the critical scattering length $a_{12,c} = -75.4\,a_0$ for which $\delta g = 0$. In the right region ($\delta g > 0$) the gas is stable at the MF level, while in the left one ($\delta g < 0$) the MF attraction is balanced by quantum fluctuations. This region is divided by the red solid line representing the critical curve $N_c(a_{12})$: if $N < N_c$ the system forms a so-called LHY gas, while above N_c a droplet is created. N_c decreases as the strength of the attractive interaction increases: this is a result of a higher droplet binding energy that counteracts the surface tension.

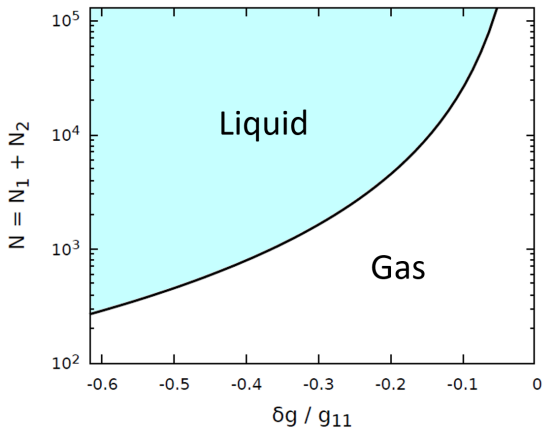

Figure 3.14: Phase diagram for the ^{41}K-^{87}Rb mixture in the self-bound regime $\delta g < 0$. The black solid line is the critical curve N_c that separates the self-bound liquid phase from the free gaseous one.

The phase diagram in Figure 3.14 has been experimentally verified using the three-body losses mechanism [6, 35, 50], that is responsible for the decrease in the number of atoms inside a liquid drop due to collisions that recombine two atoms into one molecule. Due to energy and momentum conservation, three atoms must be involved in the collision and so the loss rate strongly increases with density. The typical lifetime of a liquid droplet is limited by these losses to a range between a few and tens of milliseconds: during this period the atom number decreases until the liquid-gas phase transition is reached and the droplet evaporates.

At the end of evaporation, the three-body losses stop and the number of atoms remains constant.

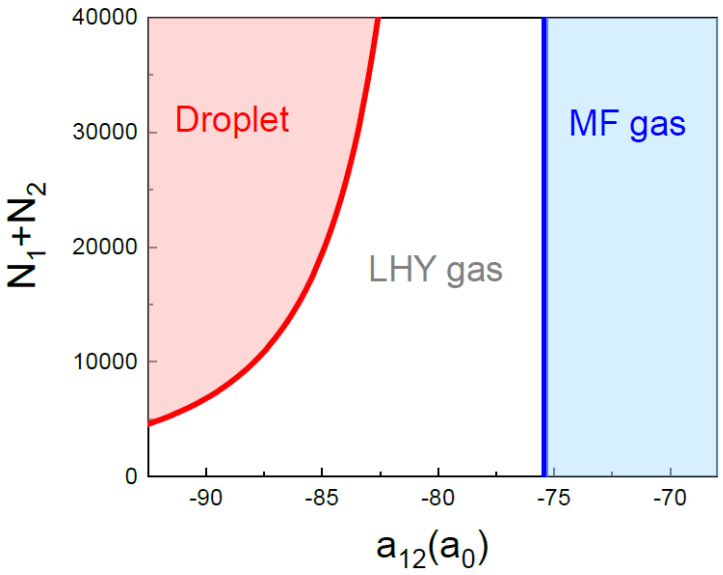

Figure 3.15: Phase diagram for the ^{41}K-^{87}Rb mixture, in free space. For $a_{12} > a_{12,c}$ the gas is stable within the MF theory (the blue solid line represents the critical scattering length $a_{12,c} = -75.4\,a_0$). For $a_{12} < a_{12,c}$ the MF energy is balanced by the Lee-Huang-Yang term, giving birth to a LHY gas. For a sufficiently large atom number (the red solid line stands for the critical curve N_c) and strong interactions, self-bound droplets can be formed. Figure taken from [37].

Finally, we report in Table 3.4 the critical atom number for some values of the interspecies scattering length that will be analyzed in the following of this thesis work.

a_{12} [a_0]	-85	-90	-95	-100	-105
N_c [a_0]	20 669.9	7255.13	3476.47	1970.56	1241.07

Table 3.4: Critical number of particles for different values of the interspecies scattering length.

Chapter 4

Vortices in a uniform Bose mixture

Inside a Bose superfluid a vortex is a quantized topological excitation that represents a line singularity in the phase of the condensate wave function: in particular, this phase has an increment of 2π each time one turns once around such a line. Vortices play a crucial role inside a rotating superfluid, therefore they are expected to come out as soon as one starts the investigation of rotational properties of quantum droplets made of binary Bose mixtures. In Chapter 1 we discussed the properties of *linear vortices*: they terminate at the surface of the superfluid in such a way that the end points are always orthogonal to it (this is the typical vortical configuration displayed by quantum droplets). However, other more complicated forms can be found inside a superfluid: among them there are the so called *vortex rings*, i.e. vortex lines of circular shape that close on themselves.
This chapter is devoted to the analysis of the main effects that characterize a uniform Bose mixture in the presence of vorticity.

4.1 Vorticity in a uniform system

The starting point is the uniform system made of a ^{41}K-^{87}Rb mixture, where the density of each species is constant over the whole available space: we work in the droplet regime, where $\delta g < 0$.
We consider a linear, singly quantized vortex excitation with axis parallel to the z direction and with a core located at the position (x_v, y_v). According to [4, 51], this vortex can be generated through the "imprinting procedure" that consists of computing the stationary state obtained by starting the imaginary time evolution from the following wave function:

$$\begin{aligned} \psi^{ini}(\vec{r}) &= \sqrt{\rho_0(\vec{r})}\, e^{i\,\theta(\vec{r})} \\ &= \sqrt{\rho_0(\vec{r})}\, \frac{(x-x_v)+i\,(y-y_v)}{\sqrt{(x-x_v)^2+(y-y_v)^2}} \end{aligned} \tag{4.1}$$

$\rho_0(\vec{r})$ represents the ground state density of the system in the absence of the vortex, while the phase $\theta(\vec{r})$ corresponds to the polar angle in the x-y plane around the vortex centre.
During the evolution in imaginary time, the vortex position and the structure of the vortex core change in order to provide, once convergence is reached, the lowest energy configuration: this will be the stationary state of the system with embedded vorticity.
In the presence of N_v vortices, labelled by $k = 1, \ldots, N_v$, at positions $(x_v^{(k)}, y_v^{(k)})$, the effective wave function in Eq. (4.1) can be easily generalized to:

$$\psi^{ini}(\vec{r}) = \sqrt{\rho_0(\vec{r})} \prod_{k=1}^{N_v} \frac{\left(x-x_v^{(k)}\right)+i\,\left(y-y_v^{(k)}\right)}{\sqrt{\left(x-x_v^{(k)}\right)^2+\left(y-y_v^{(k)}\right)^2}} \tag{4.2}$$

Let's now consider a uniform system and let's introduce a vortex line in each of the two species at the origin of the x-y plane in the mesh of simulation: $(x_v, y_v) = (0,0)$, while $\rho_0(\vec{r}) = \rho^{(b)}$ is the corresponding constant density.

4.1.1 Superfluid velocity field

It is convenient to decompose the wave function in terms of its real and imaginary parts, rather than working directly with the local phase. The system is totally superfluid, so the normal component to the density can be neglected ($\rho = \rho_s$) and the current $\vec{j}(\vec{r})$ is given by:

$$\begin{aligned}\vec{j}(\vec{r}) &= \frac{\hbar}{2m\,i}\left[\psi^*(\vec{r})\,\vec{\nabla}\psi(\vec{r}) - \vec{\nabla}\psi^*(\vec{r})\,\psi(\vec{r})\right] \\ &= \frac{\hbar}{m}\left[\mathrm{Re}\psi(\vec{r})\,\vec{\nabla}\mathrm{Im}\psi(\vec{r}) - \mathrm{Im}\psi(\vec{r})\,\vec{\nabla}\mathrm{Re}\psi(\vec{r})\right] \\ &\equiv \rho(\vec{r})\,\vec{v}(\vec{r})\end{aligned} \tag{4.3}$$

The superfluid velocity is thus:

$$\vec{v}(\vec{r}) = \frac{\hbar}{m\,\rho(\vec{r})}\left[\mathrm{Re}\psi(\vec{r})\,\vec{\nabla}\mathrm{Im}\psi(\vec{r}) - \mathrm{Im}\psi(\vec{r})\,\vec{\nabla}\mathrm{Re}\psi(\vec{r})\right] \tag{4.4}$$

In the presence of one singly quantized vortex, the superfluid velocity must obey anti-periodic boundary conditions (aPBC), in such a way that there is no flow across the boundaries of the computational cell.
Moreover, the system under study is actually a superfluid if the circulation of the velocity field along a closed path that encircles the center of the vortex is quantized: in the presence of one singly quantized vortex ($n = 1$), the value of the circulation is expected to be $\kappa = h/m$.
The simulation mesh, as explained in Appendix B, is a cubic box with the center in the origin of a 3D Cartesian reference system. For this particular configuration it is possible to reduce to two dimensions, exploiting the translational invariance along the z direction: there is no discretization along z (i.e. the number of points is $n_z = 1$), therefore the mesh is a square with coordinates $x \in [-x_{max}, x_{max}[$, $y \in [-y_{max}, y_{max}[$. The circulation of the superfluid velocity is computed along a square path with the center in the origin and the side equal to 80 % of the side of the mesh. More explicitely, denoting with $(\pm x^*, \pm y^*)$ the coordinates of the integration path, the circulation is computed as:

$$\begin{aligned}\kappa &= \oint_C d\vec{s}\cdot\vec{v} \\ &= \int_{-x^*}^{x^*} dx\,[v_x(x,-y^*) - v_x(x,y^*)] + \int_{-y^*}^{y^*} dy\,[v_y(x^*,y) - v_y(-x^*,y)] \equiv \kappa_x + \kappa_y\end{aligned} \tag{4.5}$$

Notice that the sign of the circulation can be changed by simply changing the sign of the imaginary part of the initial effective wave function in Eq. (4.1): this transformation maps a counterclockwise velocity flow into a clockwise one (and viceversa).

4.1.2 Vortex energy

The energy associated to a vortex inside a uniform system corresponds to the kinetic energy related to the spatial variation of the wave function (and, therefore, of the density profile) approaching the vortex core. The presence of a linear vortex suggests the use of a cylindrical geometry, in particular one can consider a cylinder with radius $R = \sqrt{x^2+y^2}$ and length L coaxial with the vortex. According to [52], a measure of the local vortex excitation energy per unit length is the integrated vortex kinetic energy:

$$\frac{E_{kin}}{L} = \frac{1}{L}\int_{\text{cylinder}} dx\,dy\,dz\,\frac{\hbar^2}{2m}|\vec{\nabla}_R\psi|^2 = \frac{\hbar^2}{2m}\int_0^{2\pi} d\varphi\int_0^R dR'\,R'\,|\vec{\nabla}_R\psi|^2 \tag{4.6}$$

where $\vec{\nabla}_R = \left(\frac{\partial}{\partial x}, \frac{\partial}{\partial y}\right)$ is the gradient restricted to the x-y plane.
Let's consider, for a moment, the general case of a system whose density is not uniform on the x-y

plane (but it is along the z direction). In the absence of vortices, the wave function is $\psi(\vec{r}) = \sqrt{\rho(\vec{r})}$ and Eq. (4.6) becomes:

$$\frac{E_{kin}}{L} = \frac{\hbar^2}{2m}\int_0^{2\pi} d\varphi \int_0^R dR'\, R' \,|\vec{\nabla}_R \sqrt{\rho(R',\varphi)}|^2 \tag{4.7}$$

The only contribution to the total kinetic energy comes from the density fluctuations inside the cylinder.
When the system contains a vortex, the wave function acquires a phase factor $\psi^v(\vec{r}) = \sqrt{\rho(\vec{r})}\, e^{i\,\theta(x,y)}$ and the kinetic energy per unit length reads:

$$\begin{aligned}\frac{E^v_{kin}}{L} &= \frac{E_{kin}}{L} + \frac{\hbar^2}{2m}\int_0^{2\pi} d\varphi \int_0^R dR'\, R'\, \rho(R',\varphi)\,|\vec{\nabla}_R \theta(R',\varphi)|^2 \\ &= \frac{E_{kin}}{L} + \frac{m}{2}\int_0^{2\pi} d\varphi \int_0^R dR'\, R'\, \rho(R',\varphi)\,|\vec{v}|^2\end{aligned} \tag{4.8}$$

Now, there appears a second contribution, connected to the spatial variation of the phase, that corresponds to the "hydrodynamic" kinetic energy density integrated over the volume of the cylinder. This last term is exactly the pure kinetic energy associated to the vortex, therefore:

$$\begin{aligned}\epsilon_v(R) &= \frac{1}{L}\left[E^v_{kin}(R) - E_{kin}(R)\right] \\ &= \frac{m}{2}\int_0^{2\pi} d\varphi \int_0^R dR'\, R'\, \rho(R',\varphi)\,|\vec{v}|^2\end{aligned} \tag{4.9}$$

Eq. (4.9) can be further manipulated using the classical hydrodynamic approximation for a vortex of circulation κ in an incompressible fluid of density ρ_0:

$$\epsilon_v^{hydro}(R) = \frac{m\,\rho_0}{2}\int_0^{2\pi} d\varphi \int_0^R dR'\, R' \left(n\frac{\hbar}{m\,R'}\right)^2 = \frac{\hbar^2}{m}\,\pi\,\rho_0\,n^2\,\ln\left(\frac{R}{d_c}\right) \tag{4.10}$$

Energy displays a logarithmic dependence on the distance from the vortex axis, where d_c is a quantity that allows to regularize the radial integral and it is related to the vortex-core radius . Moreover, the vortex excitation energy grows quadratically with the winding number n, meaning that states with highly quantized vortices are very unlikely to be formed.

4.1.3 Healing length for a Bose mixture

A single species BEC, in the absence of an external trapping potential, is described by a wave function $\psi(\vec{r})$ that obeys the stationary GP equation:

$$\left(-\frac{\hbar^2}{2m}\vec{\nabla}^2 + g|\psi|^2\right)\psi = \mu\,\psi \tag{4.11}$$

This is a nonlinear Schroedinger equation involving both the kinetic energy and the local repulsive Hartree potential $g\rho$ for a uniform medium with bulk density $\rho = |\psi|^2$. From dimensional considerations [53], it is possible to introduce a correlation length ξ that allows to approximate the Laplace operator as $\vec{\nabla}^2 \simeq \xi^{-2}$ and it is defined from the balance between the two terms in Eq. (4.11):

$$\xi = \frac{\hbar}{\sqrt{2m\rho g}} = \frac{1}{\sqrt{8\pi\rho a}} \tag{4.12}$$

It is called *healing length* and it characterizes the distance over which the condensate wave function gets back to its bulk value when perturbed locally.
Using a similar procedure, one can derive the explicit expression of the healing length associated to each of the two species inside a binary Bose mixture. For sake of simplicity, the densities are assumed to satisfy the *MF optimal ratio* of Eq. (2.14) so that one is left with the energy density in Eq. (2.22) that depends on the density of the first species alone. A functional minimization, subject to the constraint

of keeping fixed the total number of particles (with μ_1 as a Lagrange multiplier), yields the stationary GP equations that is satisfied by the wave function ψ_1:

$$\left(-\alpha\vec{\nabla}^2 + 2\beta\rho_1 + \frac{5}{2}\gamma\rho_1^{3/2}\right)\psi_1 = \mu_1\psi_1 \tag{4.13}$$

The left hand side is made of three terms: the first one associated to the kinetic energy, while the other two representing the MF and LHY contributions to potential energy. Remembering that the kinetic contribution is a positive quantity, the balance of these terms leads to the condition

$$\alpha\frac{1}{\xi_1^2} + 2\beta\rho_1^{(b)} + \frac{5}{2}\gamma\rho_1^{(b)3/2} = 0 \tag{4.14}$$

where a dimensional analysis was employed to substitute the Laplace operator with the correlation length and the local density with its bulk value.
It is now straightforward to write down the explicit expression for the healing length of the first species from Eq. (4.14):

$$\xi_1 = \left(-\frac{\alpha}{2\beta\rho_1^{(b)} + \frac{5}{2}\gamma\rho_1^{(b)3/2}}\right)^{1/2} \tag{4.15}$$

The minus sign accounts for the fact that the total interaction potential is negative since it describes a self-bound system.
The expression for the healing length of the second species has exactly the same form as Eq. (4.15), provided the following substitutions:

$$\rho_1^{(b)} \mapsto \rho_2^{(b)} \qquad \alpha \mapsto \alpha' = \sqrt{\frac{g_{22}}{g_{11}}}\alpha \qquad \beta \mapsto \beta' = \frac{g_{22}}{g_{11}}\beta \qquad \gamma \mapsto \gamma' = \left(\frac{g_{22}}{g_{11}}\right)^{5/4}\gamma$$

Notice that, if the bulk densities satisfy exactly the *MF optimal ratio*, then the two healing lengths coincide.

4.2 Vortices inside a cylinder

The hydrodynamic approximation discussed in Section 4.1.2 can be tested by directly studying vortices in a cylindrical geometry. The mixture is contained inside a box with sides $2 \times x_{max}$, $2 \times y_{max}$, $2 \times z_{max}$ and the density is not vanishing inside a cylinder with radius R_{cy} in the x-y plane and height $L = 2 \times z_{max}$ along the z-direction. This means that the initial density profiles, for each of the two species ($i = 1, 2$), are parametrized by:

$$\rho_i(x, y, z) = \begin{cases} \rho_i^{(b)} & \text{if} \quad \sqrt{x^2 + y^2} \leq R_{cy} \\ 0 & \text{otherwise} \end{cases} \tag{4.16}$$

where $\rho_i^{(b)}$ represents the density of the i^{th} species in the uniform system for a given value of the interspecies scattering length a_{12}.
By means of the "imprinting" procedure, a singly quantized vortex line is introduced into each of the two species with the geometry explained above: they are aligned along the z-axis and they are located at the origin of the x-y plane.
The total number of particles for each species is set in such a way that the density inside the volume of the cylinder corresponds to the bulk value, that is:

$$\frac{N_i}{V} = \rho_i^{(b)} \qquad \longrightarrow \qquad N_i = \rho_i^{(b)}\,\pi\,R_{cy}^2\,L = 2\,\rho_i^{(b)}\,\pi\,R_{cy}^2\,z_{max} \qquad i = 1, 2 \tag{4.17}$$

After the initialization is completed, the whole system undergoes an evolution in imaginary time until it reaches a stable configuration that corresponds to the ground state in the presence of two

singly quantized vortices, one in each component. During the relaxation, the density modifies and the system rearranges the radius of the cylinder in order to minimize the total energy. A qualitative example of the final shape for the density profiles is provided by Figure 4.1, where three main features can be highlighted:

- in correspondence of the position of the vortex, there is a depletion of the density that drops to zero with a quadratic behaviour close to the origin of the x-y plane: this region represents the *vortex core*;
- far from the vortex line the density saturates to a constant bulk value that is given by the equilibrium value for the uniform system, $\rho^{(b)}$;
- in the outer region one can recognize the interface between the bulk and the vacuum: here the density rapidly decays to zero with an exponential behaviour.

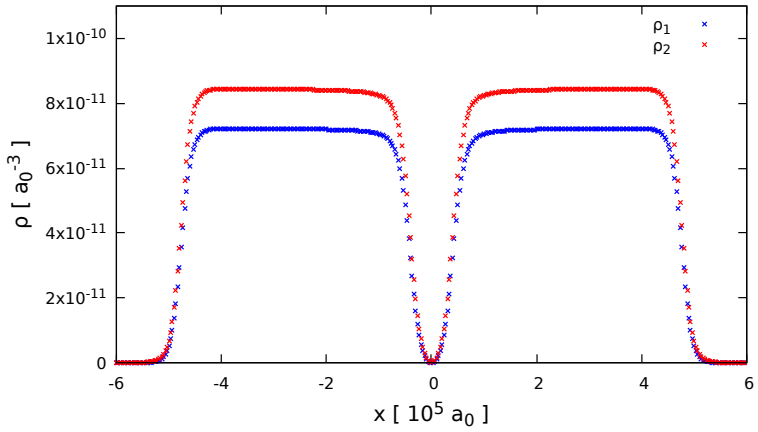

Figure 4.1: One-dimensional projection along the x-direction of the densities of the two species (blue markers for the first one, red markers for the second one). These profiles are the result of a computation performed with $R_{cy} = 5 \times 10^5\ a_0$ and $a_{12} = -85\ a_0$.

The study of vortices inside a uniform mixture can be performed also by means of simulations in a so called *extended system*, i.e. assuming the density to be constant inside the whole 3D box. It was verified that the results provided by this method are equivalent to the ones with the cylindrical geometry as far as the vortex core region and the bulk one are concerned. Both these geometries are very useful in order to reduce to less demanding 2D computations, however the cylinder presents the following advantages:

- standard PBC can be implemented at the borders of the simulation cell;
- any possible unbalance in the number of atoms of the two species deviating from the *MF optimal ratio* is automatically adjusted: the fraction in excess is expelled from the cylinder creating a weak background density in the outer region;
- if the radius R_{cy} is sufficiently large, then it reproduces the plateau of the density far from the vortex core that characterizes a real extended system.

We want to compute the integrated kinetic energy per unit length at different distances R from the vortex core and compare the results with the hydrodynamic formula in Eq. (4.10). Strictly speaking, this formula accounts only for the hydrodynamic contribution to the kinetic energy, so the set of radial distances has to lay inside the bulk region, far away from both the vortex core and the interface: here the density is almost constant, so that the total kinetic energy is expected not to differ in a significant way from the hydrodynamic one. A wide bulk region is required in order to let the density saturate, so the radius of the cylinder is chosen as large as possible (compatible with the times of

simulation): the geometrical dimensions of the simulation domain are collected in Table 4.1.

The integrated kinetic energy per unit length is computed for both species, since each of them contains a vortex, and the whole procedure is repeated for five different values of the interspecies scattering length a_{12} inside the droplet regime: the goal is to investigate how the size of the vortex core depends on the strength of this attractive interaction.

R_{cy} $[a_0]$	x_{max} $[a_0]$	y_{max} $[a_0]$	z_{max} $[a_0]$	L $[a_0]$
20×10^5	21×10^5	21×10^5	42×10^5	84×10^5

Table 4.1: Geometrical parameters for the simulation of vortices inside a uniform system with cylindrical geometry.

Figure 4.2 shows the superfluid velocity of the first species in the x-y plane in the case of $a_{12} = -100\, a_0$: the streamlines follow a counterclockwise flow around the vortex line and the magnitude decreases going far away from the center, as it is expected from the dependence on the inverse of the radial distance.

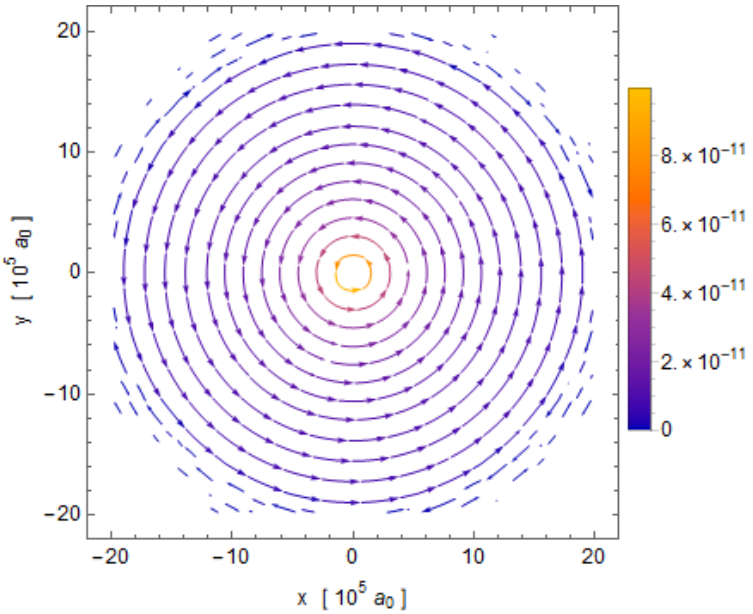

Figure 4.2: Superfluid velocity field in the x-y plane for the first species and $a_{12} = -100\, a_0$. The presence of some arrows in the external region following the opposite direction with respect to the counterclockwise flow is not relevant: this is a consequence of border effects where the density exponentially drops to zero. Values in the legend on the right of the plot are expressed in atomic units: for velocities, they correspond to $(\mathrm{Ha}\, m_e^{-1})^{1/2}$.

Once the density profile of the ground state (with embedded vorticity) is obtained, one can give an estimate of the vortex core size, d_v. It can be defined as the distance from the center at which the modulus of the wave function $|\psi(\vec{r})| = \sqrt{\rho(\vec{r})}$ is equal to half the value it takes in the saturation region. For each of the two species ($i = 1, 2$) this condition is:

$$\left|\psi_i\left(\sqrt{x^2+y^2} = d_{v,i}\right)\right| \overset{!}{=} \frac{1}{2}\left|\psi_i^{(b)}\right| = \frac{1}{2}\sqrt{\rho_i^{(b)}} \tag{4.18}$$

These estimates carried out from different simulations are collected in Table 4.2, together with the equilibrium value of the densities. It appears that the size of the vortex core is comparable for both the species and it reduces when a_{12} gets more negative. In the same table there are also the healing lengths computed for each species: strictly speaking, they are obtained multiplying by $\sqrt{2}$ the result of Eq. (4.15). The ratio $d_{v,i}/\xi_i$ turns out to be a constant quantity, as it will be better investigated in the following after the introduction of a new parameter that is related to the core size.

	^{41}K			^{87}Rb		
a_{12} $[a_0]$	$\rho_1^{(b)}$ $[a_0^{-3}]$	$d_{v,1}$ $[a_0]$	ξ_1 $[a_0]$	$\rho_2^{(b)}$ $[a_0^{-3}]$	$d_{v,2}$ $[a_0]$	ξ_2 $[a_0]$
-85	7.210×10^{-11}	32 706	25 284	8.315×10^{-11}	32 716	24 973
-90	1.675×10^{-10}	17 600	14 554	1.917×10^{-10}	17 605	13 304
-95	3.033×10^{-10}	11 470	8751.9	3.447×10^{-10}	11 480	8543.9
-100	4.799×10^{-10}	8204.5	6250.3	5.418×10^{-10}	8212.3	6069.3
-105	6.980×10^{-10}	6242.0	4755.9	7.828×10^{-10}	6250.0	4592.8

Table 4.2: Equilibrium densities (computed from the numerical code) and numerical estimates of the vortex core for each species at different interspecies scattering lengths a_{12}. Other reported quantities are the healing lengths estimated by means of Eq. (4.15).

The integrated total kinetic energy at a given distance R is computed by discretizing Eq. (4.6) and then summing the contributions from each of the two species.
For each of them ($i = 1, 2$), these values should be described by the hydrodynamic form in Eq. (4.10) that, after some manipulations, can be written as:

$$\begin{aligned} \frac{E_{kin,i}}{L}(R) &= \frac{\hbar^2}{m_i}\,\pi\,\rho_i^{(b)}\,\ln\left(\frac{R}{\lambda_i}\right) \\ &= \Bigg[\underbrace{\frac{m_e}{m_i}\,\pi\,\rho_i^{(b)}}_{A_i}\,\ln(R)\;\underbrace{-\frac{m_e}{m_i}\,\pi\,\rho_i^{(b)}\,\ln(\lambda_i)}_{B_i}\Bigg]\frac{\mathrm{Ha}}{a_0} \end{aligned} \tag{4.19}$$

Going from the first to the second line each quantity was explicitly expressed in atomic units so that one can work with dimensionless variables. Notice that the so called *core parameter* λ has been introduced in the above phenomenological formula to replace d_c in Eq. (4.10).

The kinetic energies per unit length can be, therefore, fitted with the logarithmic function

$$\frac{E_{kin,i}}{L}(R) \;=\; A_i\,\ln(R) \,+\, B_i \tag{4.20}$$

and then, from the fit parameters A_i, B_i, it is possible to determine the value of the density in the bulk region and the corresponding core parameter:

$$\rho_i^{(b)} \;=\; \frac{m_i}{m_e}\,\frac{1}{\pi}\,A_i \qquad\qquad \lambda_i \;=\; e^{-B_i/A_i} \tag{4.21}$$

	^{41}K		^{87}Rb	
a_{12} $[a_0]$	$\rho_1^{(b)}$ $[a_0^{-3}]$	λ_1 $[a_0]$	$\rho_2^{(b)}$ $[a_0^{-3}]$	λ_2 $[a_0]$
-85	7.147×10^{-11}	26 974	8.370×10^{-11}	26 901
-90	1.649×10^{-10}	14 554	1.932×10^{-10}	14 493
-95	2.969×10^{-10}	9411.6	3.478×10^{-10}	9354.6
-100	4.674×10^{-10}	6729.2	5.476×10^{-10}	6676.6
-105	6.764×10^{-10}	5121.3	7.926×10^{-10}	5072.0

Table 4.3: Parameters $\rho^{(b)}$ and λ computed from the fit of the vortex kinetic energy with the hydrodynamic form given by Eq. (4.20) for both species and five different values of a_{12}

Estimates from the fit parameters are collected in Table 4.3. A first result is that the bulk densities derived from the hydrodynamic fit are compatible with the numerical values reported in Table 4.2. After that, there is nothing that physically relates the λ parameters to the actual size of the vortex cores in the hydrodynamic model, so it is not a surprise that they do not coincide with the estimates, denoted with d_v: however they share a common general trend highlighting that the vortex core shrinks as the interspecies interaction becomes more attractive.

4.2.1 Deviations from the hydrodynamic approximation

On the one hand, it was seen that the hydrodynamic model works very well in the bulk region, far away from the vortex core: the parameters coming out from the logarithmic fit, in fact, are consistent with the composition of the mixture and the observed geometry of the vortices. On the other hand, it is also interesting to analyze where the hydrodynamic approximation loses its validity: clearly this should happen for low radial values, i.e. in the proximity of the vortex core where the contribution to the kinetic energy due to density fluctuations becomes important. The results, in the specific case of the first species, are shown in Figure 4.3, where the radial density profile (black open points) is superimposed to the values of the integrated kinetic energies per unit length represented by blue open squares: approaching the vortex center, the density drops to zero and the kinetic energy deviates from the hydrodynamic model (the red solid line in the figure).

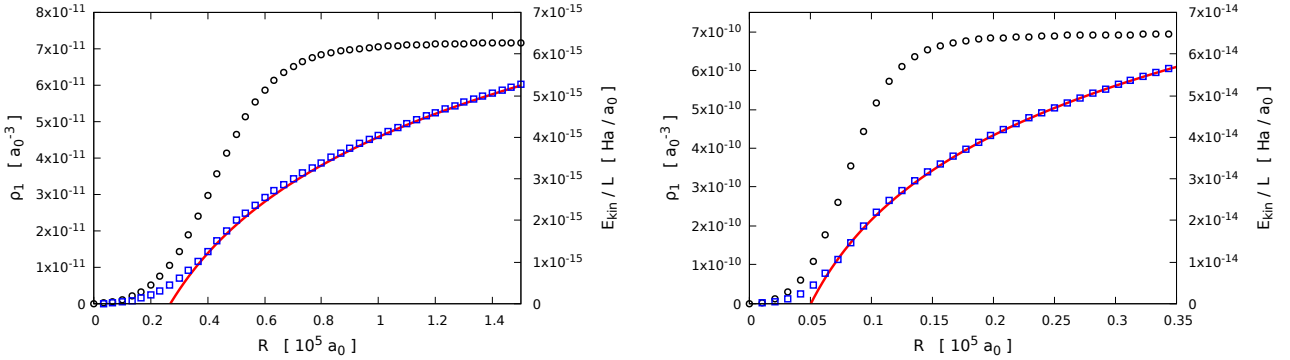

(a) $a_{12} = -85\,a_0$ (b) $a_{12} = -105\,a_0$

Figure 4.3: Zoom on the vortex core region for the first species and for the minimum and maximum values of a_{12}. Blue squares are the integrated kinetic energies, while the red line is the hydrodynamic fit that is obtained in the bulk region. Black open points represent the corresponding density profile in order to highlight the vortex core region where the hydrodynamic form stops to be valid.

Let's write the wave function of one single species, $\psi(\vec{r})$, in the hydrodynamic expression

$$\psi(\vec{r}) = \sqrt{\rho(\vec{r})}\, e^{i\theta(\vec{r})} = \phi(\vec{r})\, e^{i\theta(\vec{r})} \tag{4.22}$$

where $\phi(\vec{r}) = \sqrt{\rho(\vec{r})}$ accounts for the spatial variation of the density, while the phase factor yields the superfluid velocity $\vec{v}(\vec{r}) = \hbar/m\vec{\nabla}\theta(\vec{r})$.
As previously anticipated, close to the vortex center this wave function has a linear behaviour in the radial distance, meaning that it can be written as $\phi(\vec{r}) = \alpha\, r$, with α a constant prefactor. In a small region within the vortex core size, therefore, the integrated kinetic energy per unit length becomes:

$$\begin{aligned}\frac{E_{kin}}{L}(R) &\overset{R\ll 1}{\sim} \frac{1}{L}\int dz \int_0^{2\pi} d\varphi \int_0^R dr\, r\, \frac{\hbar^2}{2m}|\vec{\nabla}\psi(r)|^2 \\ &= 2\pi \int_0^R dr\, r \left(\frac{\hbar^2}{2m}|\vec{\nabla}\phi(r)|^2 + \frac{m}{2}|\phi(r)|^2|\vec{v}(r)|^2\right) \\ &= 2\pi\,\frac{\hbar^2}{2m}\,\alpha^2 \int_0^R dr\, 2r = \frac{\hbar^2}{m}\,\pi\,\alpha^2\,R^2\end{aligned} \tag{4.23}$$

There is the same quadratic dependence on the radial distance as for the density.

One can define a core energy as the integrated kinetic energy per unit length evaluated exactly at the core size:

$$\frac{E_{kin}^{core}}{L} \equiv \frac{E_{kin}}{L}(R = d_v) \tag{4.24}$$

Exploiting the definitions of d_v and of the wave function $\phi(\vec{r})$ (see Eq. (4.18)), the explicit espression of the parameter α can be obtained:

$$\begin{cases} \phi(r = d_v) & \equiv \frac{1}{2}\phi^{(b)} = \frac{1}{2}\sqrt{\rho^{(b)}} \\ \phi(r = d_v) & = \alpha\, d_v \end{cases} \qquad \Longrightarrow \qquad \alpha = \frac{\sqrt{\rho^{(b)}}}{2d_v} \tag{4.25}$$

Substituting this result inside Eq. (4.23):

$$\frac{E_{kin}^{core}}{L} = \frac{\hbar^2}{m}\,\pi\,\alpha^2\,d_v^2 = \frac{\pi}{4}\,\frac{\hbar^2}{m}\,\rho^{(b)} \tag{4.26}$$

We recall that the the bulk densities can be estimated by the approximated results carried out in the study of the uniform system (see Eq. (2.31) in Section 2.3), so that:

$$\begin{aligned} \rho_1^{(b)} \simeq \rho_1^{(0)} = \mathcal{K}_1'\,\delta g^2 \quad &\rightarrow \quad \frac{E_{kin,1}^{core}}{L} \simeq \frac{\pi}{4}\,\frac{\hbar^2}{m_1}\,\mathcal{K}_1'\,\delta g^2 = \mathcal{K}_1\,\delta g^2 \\ \rho_2^{(b)} \simeq \rho_2^{(0)} = \mathcal{K}_2'\,\delta g^2 \quad &\rightarrow \quad \frac{E_{kin,2}^{core}}{L} \simeq \frac{\pi}{4}\,\frac{\hbar^2}{m_2}\,\mathcal{K}_2'\,\delta g^2 = \mathcal{K}_2\,\delta g^2 \end{aligned} \tag{4.27}$$

where the $\mathcal{K}$'s are constant factors introduced to simplify the notation. The key result is that the core energies are quadratic in the parameter δg and so they display a parabolic behaviour also in the scattering length a_{12} (see Eqs. (2.6, 2.13)).

Figure 4.4 shows a very good agreement between the calculated values of the core energy (black squares for the first species and black diamonds for the second one) and the predictions of the above model (red dotted parabolas). Deviations can be due to the fact that the bulk densities used in the numerical code do not perfectly coincide with the ones given in Eq. (4.27).

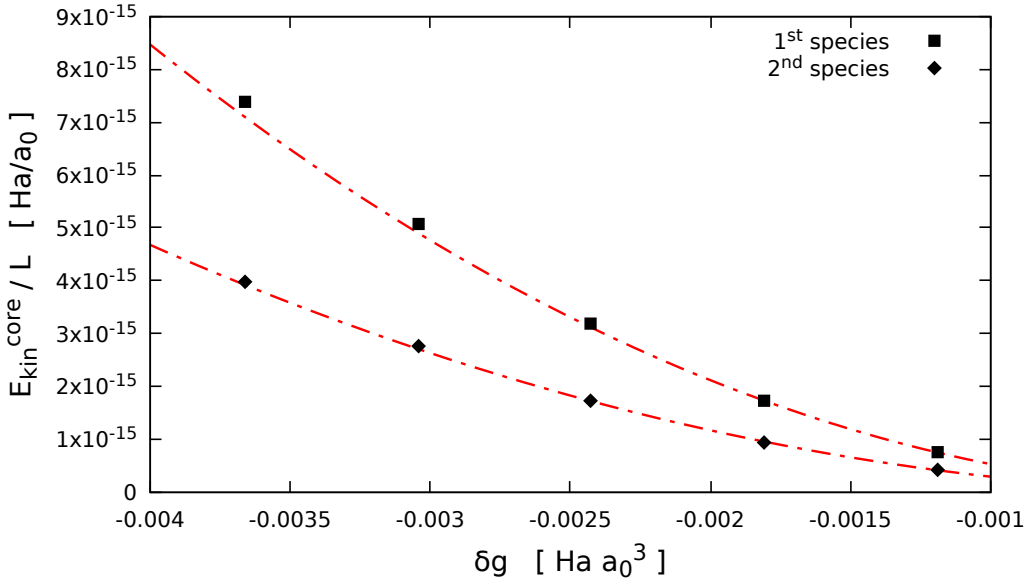

Figure 4.4: Core energies for the two species as a function of the parameter δg. Black squares and diamonds represent the numerical results, while the red dashed lines are obtained from the theoretical estimations in Eq. (4.27).

In Figure 4.5 the projection of the densities of the first species (red data) and the second one (green data) along the x axis are represented, together with the ratio ρ_1/ρ_2 (blue points). The ratio between the two densities remains constant to the ratio between the starting bulk densities (marked by the purple dashed line in the figure), while deviations start to appear as soon as one gets closer to the vortex core, reaching the maximum exactly at the vortex center. These deviations are small effects,

but it is interesting to look at what happens going from the minimum (Figure 4.5 (a)) to the maximum (Figure 4.5 (b)) value of a_{12}. As the interspecies interaction becomes more attractive, the deviations from the constant ratio increase and the same happens for the gap between this constant ratio and the MF optimal one, represented with the orange dashed line. As a last comment, when studying the ratio between densities in the case of a vortex in an extended system one obtains results that are very similar to Figure 4.5: in the core region the ratio increases with respect to the bulk one.

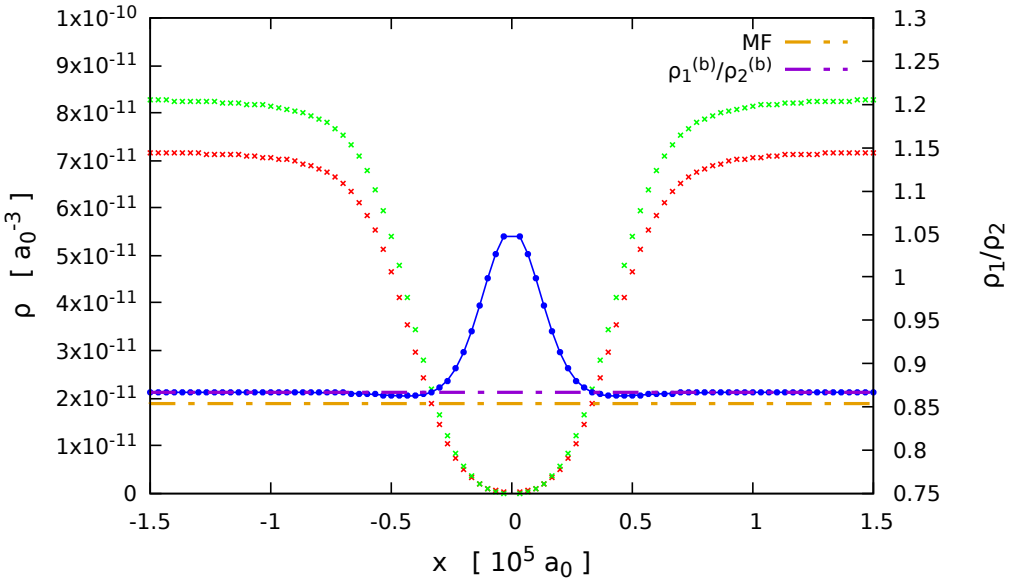

(a) $a_{12} = -85\, a_0$

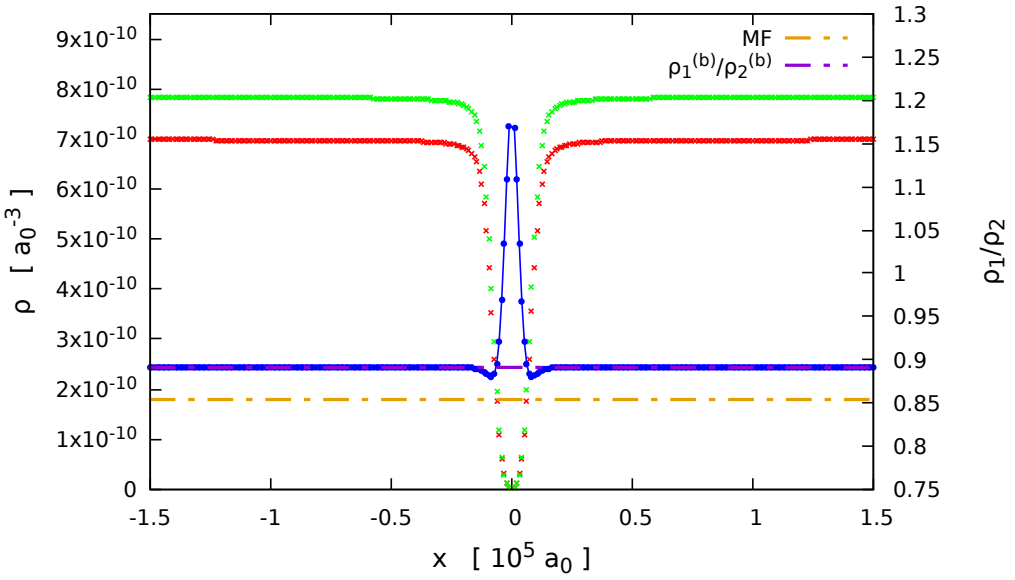

(b) $a_{12} = -105\, a_0$

Figure 4.5: Densities of the first (red) and second (green) species and ratio (blue points) between them for the minimum and maximum value of the interspecies scattering length. The orange dashed line shows the *MF optimal ratio* $(g_{11}/g_{22})^{1/2}$, while the purple dashed one corresponds to the ratio between the bulk values of the densities.

Figure 4.6 represents a summary of what happens to the vortex core when the interspecies interaction becomes more attractive. The core size was estimated by means of three quantities (d_v, λ, ξ) that are shown together in Figure 4.6 (a): they do not coincide since they are obtained from different definitions and procedures, however they clearly show the tendency of the vortex to shrink going towards more negative values of a_{12}. The consistency of the choice of these quantities is confirmed by Figure 4.6 (b) that contains all the possible ratios between them: these ratios, apart from small fluctuations that are more evident in the region of weak interaction, remains almost constant meaning that they provide equivalent information about the vortices studied in this section. Notice that Figure 4.6 is obtained from the data of the first species, but the same considerations can be applied to the second one, too.

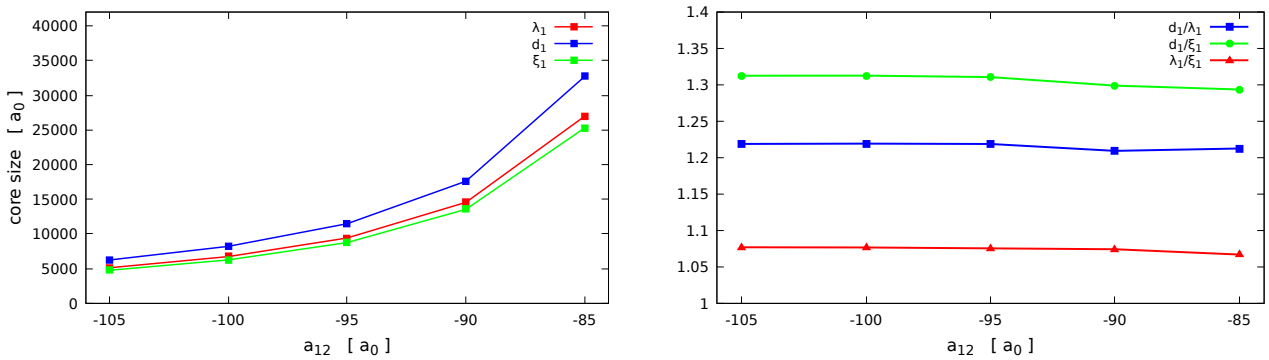

(a) Different quantities to identify the size of the vortex core.

(b) Ratios between the different quantities.

Figure 4.6: The dimension of the vortex core shrinks as the interspecies interaction becomes more attractive. These data refer to the first species (^{41}K).

In Figure 4.7 one can have a direct visualization of the behaviour that comes out from the results of the hydrodynamic fit as far as the total density $\rho = \rho_1 + \rho_2$ is concerned: going towards more negative values of a_{12}, the bulk density increases and the vortex core size reduces.

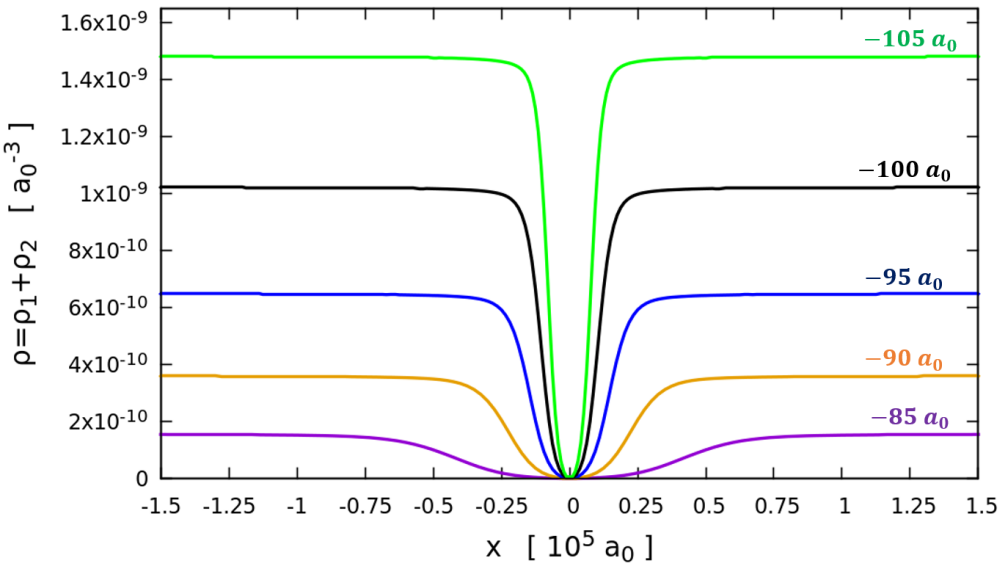

Figure 4.7: Visualization of the vortex cores for the total density $\rho = \rho_1 + \rho_2$.

4.3 Single component analysis

Up to now we have imprinted a total number of two vortices in the centre of a uniform system, one for each species. It is interesting to study what happens in the case the system carries only one quantum of vorticity in one of the two species. This can be done by imprinting a vortex in one species and then performing a minimization to reach the corresponding stationary configuration. Even in this case, we exploit the cylindrical geometry and we repeat the procedure for five different values of the interspecies scattering length.

4.3.1 Density profiles

The first interesting result comes out from the analysis of the one dimensional density profiles of the final configurations: Figure 4.8 provides an example for $a_{12} = -95\, a_0$, in fact all the other cases display the same qualitative behaviour. On the one hand, the species with embedded vorticity generates a vortex that is visible from the density profiles going to zero at the center: this is a "true" core, since both the circulation around a closed path surrounding the vortex center and the angular momentum are equal to 1 (in suitable units), as expected. On the other hand, the species without vorticity is somehow perturbed by the presence of the vortex, as the density profiles create a hole in the central region: we can call this a "fake" core, in fact both the circulation and the angular momentum for this species are equal to zero.

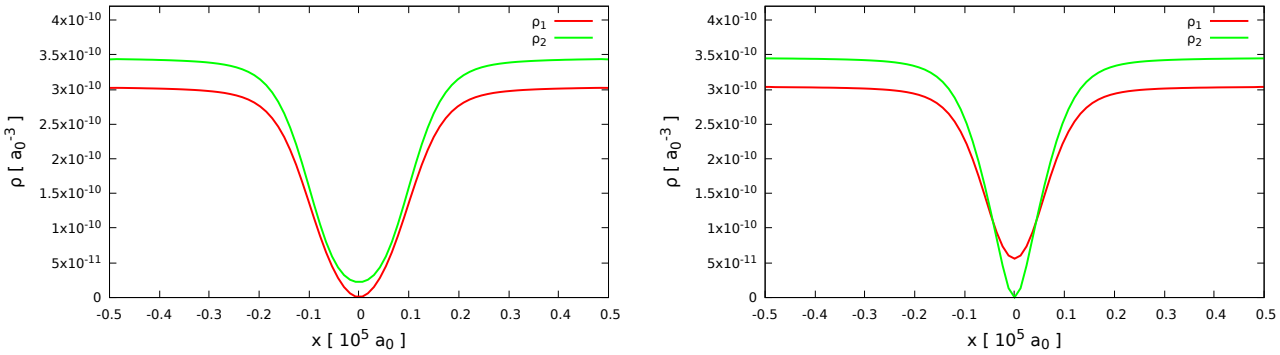

(a) Vorticity in the first species alone.

(b) Vorticity in the second species alone.

Figure 4.8: One-dimensional density profiles with vorticity in one single species for $a_{12} = -95\, a_0$.

A possible explanation can be traced back to the fact that the system tries to reorganize itself in such a way to keep the ratio between densities as close as possible to the one given by the MF theory. Clearly this condition is satisfied up to the region close to the vortex center, where one of the densities approaches zero, while the other one reaches a minimum finite value.
A second important evidence consists in the shrinkage of the vortex core when there is only one species with embedded vorticity. This fact can be appreciated looking at Figure 4.9 that shows the 1D density profiles of both species for $a_{12} = -105\, a_0$: the markers are associated to the configuration with one vortex in each species (red for the first, green for the second one), while solid lines represent the configuration with one vortex only in the second (denser) species.

4.3.2 Vortex filling

The species without vorticity is subjected to a depletion, as it is shown by the lowering of the density in the central region: the overall result is that the "true" vortex is filled by the vortex-less species and the total density $\rho = \rho_1 + \rho_2$ reaches a finite value at the vortex centre.
We study now the dependence of such a filling on the interspecies scattering length a_{12}.
For a given value of a_{12}, a vortex is imprinted in the first species and an evolution in imaginary time is run to obtain the stationary configuration: once at convergence, the residual density of the

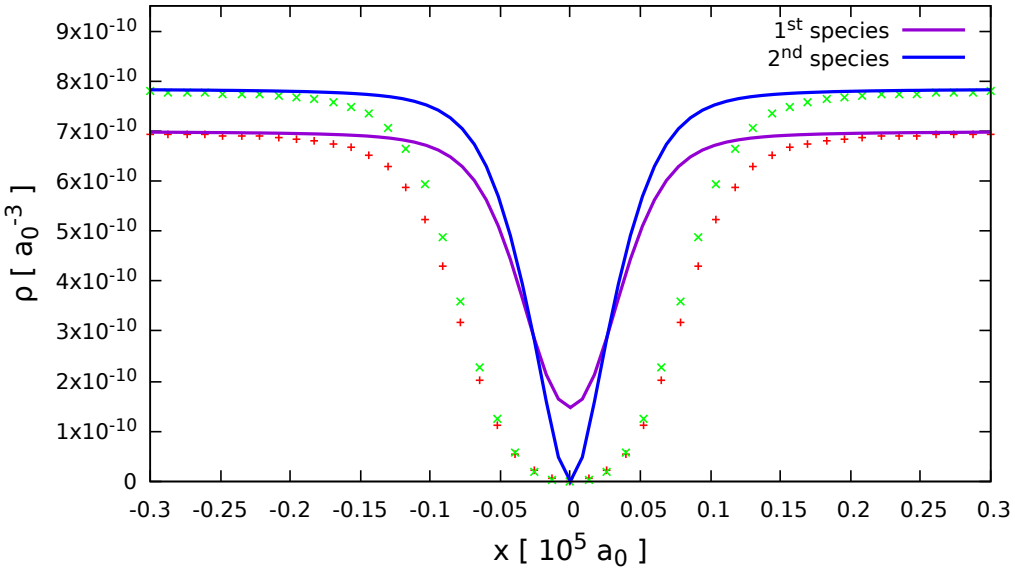

Figure 4.9: One dimensional density profiles for $a_{12} = -105\, a_0$ in the case of a vortex in each species (markers) and a vortex only in the second one (solid lines).

second species at the vortex center, denoted as $\rho_2(x = y = 0)$, is obtained. The same procedure is then applied to the configuration with one vortex in the second species, reading now the value of $\rho_1(x = y = 0)$. This analysis is carried out both in the *self-bound regime* ($a_{12} < -75.4\, a_0$) and in the *miscible* one ($a_{12} \geq -75.4\, a_0$): in the following, with a little abuse of notation, we will refer to the latter as the *uniform superfluid regime* (abbreviated with *SF*). Droplets bulk densities increase as the interspecies attraction gets stronger and Figure 4.10 shows that the same happens for the residual densities: this suggests to deal with normalized quantities (ρ_2/ρ_0, ρ_1/ρ_0) in order to get a more universal diagram. The normalization factor ρ_0 is equal to the bulk density $\rho^{(b)}$ in the *self-bound regime*, while it corresponds to the fixed density in the *SF* one.

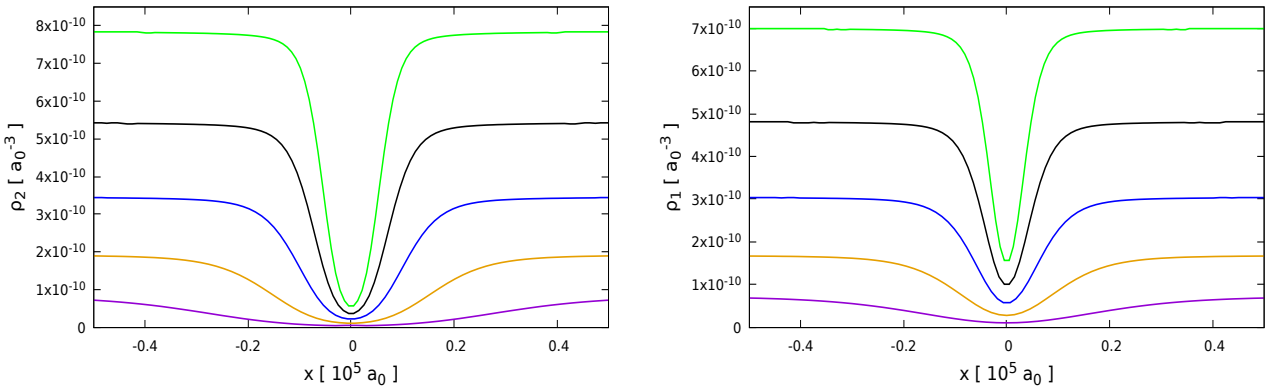

(a) Densities of the second species in the presence of a vortex in the first one.

(b) Densities of the first species in the presence of a vortex in the second one.

Figure 4.10: Density profiles of the vortex-less species when a vortex is imprinted in the other one for different values of the interspecies scattering length $a_{12}/a_0 = -85$ (purple), -90 (orange), -95 (blue), -100 (black), -105 (green).

The final values of the normalized residual densities are plotted as a function of the scattering length a_{12} in Figure 4.11. The two sets of data refer to the two configurations of vorticity in the first species (green markers) or in the second one (red markers) and they share the same behaviour: starting from the most negative value of a_{12}, the residual density decreases up to a minimum that is reached at the transition $a_{12} = a_{12,c}$, then it starts growing in the *SF* phase. Here, due to the overall repulsive

interactions, the width of vortex cores is remarkably larger with respect to the droplet phase: the increasing of the filling effect in the right part of the diagram could be a consequence of the reduction of depletion in the region of the vortex center in the *SF* phase.

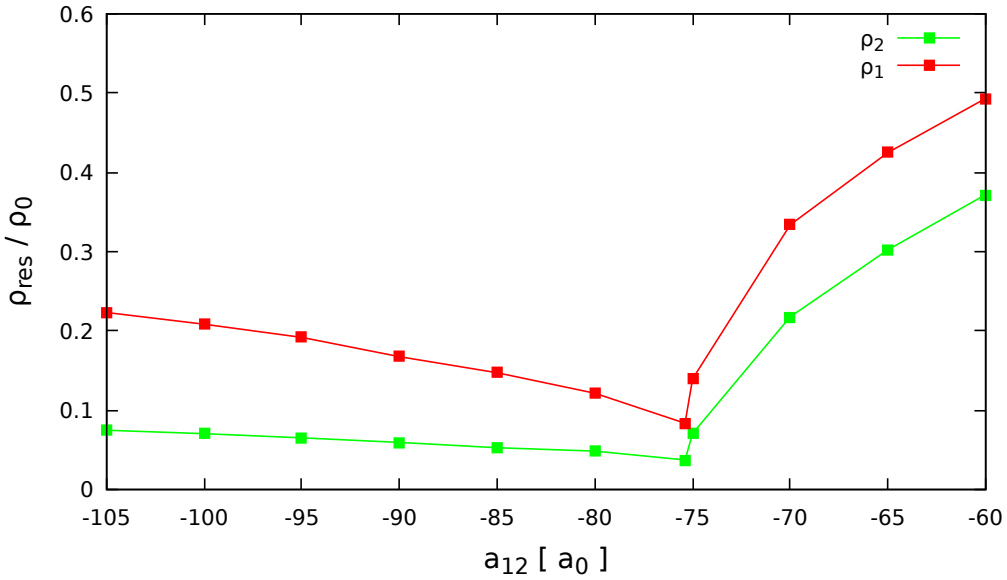

Figure 4.11: Residual densities at the vortex center normalized to the bulk value as a function of the interspecies scattering length a_{12}. Both the cases of vorticity only in the first (green data) or in the second species (red data) are reported.

4.3.3 Vortex energetics: excitation energies phase diagram

Continuing the study of vortices inside one single component, now we look for the ground state of the following four situations, with the corresponding energies per particle:

- $\left(\frac{E}{N}\right)_0$: uniform system in the absence of vortices;
- $\left(\frac{E}{N}\right)_{V_{(1+2)}}$: "double" vortex, one in each component;
- $\left(\frac{E}{N}\right)_{V_1}$: vortex in the first species alone;
- $\left(\frac{E}{N}\right)_{V_2}$: vortex in the second species alone.

We consider four possible configurations and for each of them we compute the corresponding excitation energies as:

- two isolated vortices in the first species: $2V_1$

$$\Delta\left(\frac{E}{N}\right)_{2V_1} = 2\left[\left(\frac{E}{N}\right)_{V_1} - \left(\frac{E}{N}\right)_0\right]$$

- two isolated vortices in the second species: $2V_2$

$$\Delta\left(\frac{E}{N}\right)_{2V_2} = 2\left[\left(\frac{E}{N}\right)_{V_2} - \left(\frac{E}{N}\right)_0\right]$$

- two vortices, one inside each species: V_{1+2}

$$\Delta\left(\frac{E}{N}\right)_{V_{1+2}} = \left(\frac{E}{N}\right)_{V_{1+2}} - \left(\frac{E}{N}\right)_0$$

- one vortex in the first species and one in the second one, that is far apart: $V_1 + V_2$

$$\Delta\left(\frac{E}{N}\right)_{V_1+V_2} = \left(\frac{E}{N}\right)_{V_1} + \left(\frac{E}{N}\right)_{V_2} - 2\left(\frac{E}{N}\right)_0$$

The assumption of a great distance between them allows to neglect the interaction energy.

The final results are reported as a phase diagram $\Delta(E/N)\,(a_{12})$ in Figure 4.12.
The formation of two vortices in the denser species is the most energetically favourable configuration, while two vortices in the less dense species is the least favourable one: in the middle there is the nucleation of a "double" vortex, followed by the configurations with two vortices far away. This order, valid for the droplet regime, is preserved also in the *SF* phase according to Figure 4.13: we can say this is a characteristic feature of our binary Bose mixture that is independent of the interspecies scattering length (even if the excitation energies depend on it).
Notice that our data are compatible with the presence of a discontinuity in the first derivative, suggesting that the *droplet*-to-*uniform superfluid* transition can be classified as a second order phase transition.

Some configurations with double-quantized vortices in one single species were analyzed, too, but they are located higher in energy with respect to the configurations already taken into consideration: this is consistent with the fact that the vortex kinetic energy contribution grows quadratically with the winding number, as seen in Eq. (4.10).

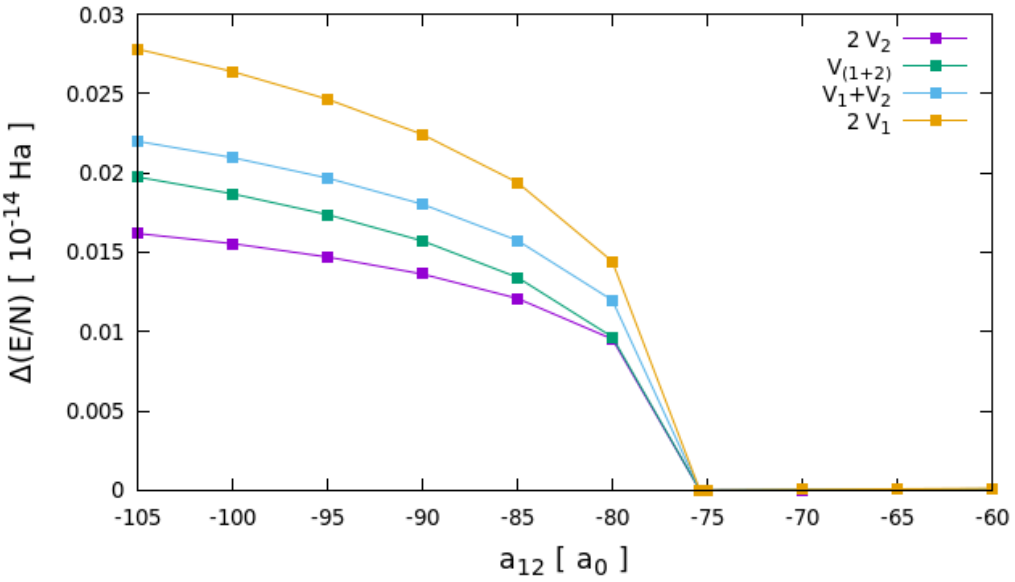

Figure 4.12: Phase diagram for the vortex excitation energies in the crossover between the *self-bound* and the *uniform superfluid* regime.

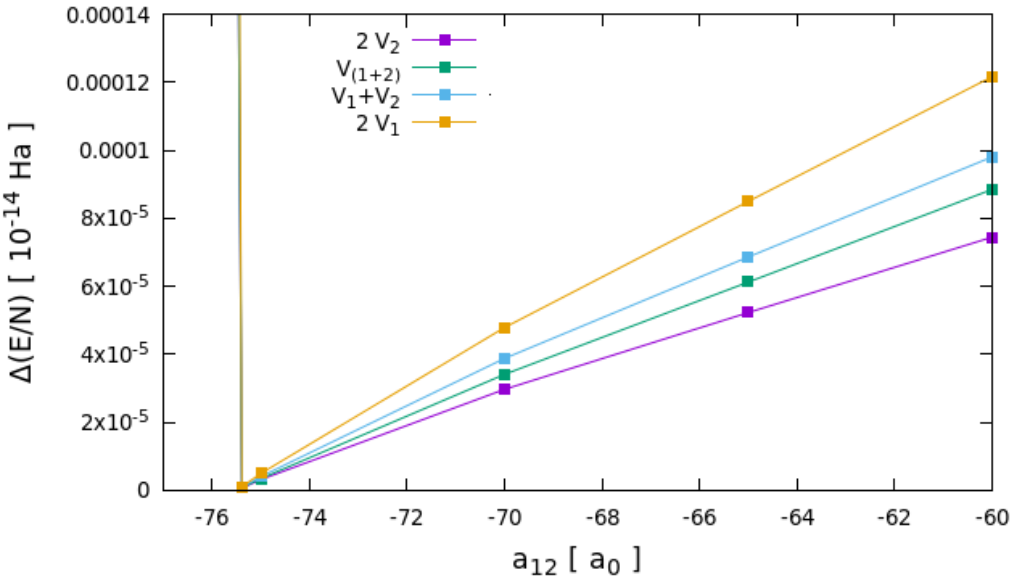

Figure 4.13: Phase diagram for the vortex excitation energies as a function of the interspecies scattering length in the *uniform superfluid* regime.

Chapter 5

Rotating quantum droplets

The results obtained from the study of rotating ^{4}He nanodroplets [4, 15] show that the angular momentum can be stored in the nucleation of quantized vortices or into capillary waves that develop in deformed configurations: the combined action of these two phenomena results in droplet shapes close to those of classical droplets rotating with the same angular velocity. This result can be directly appreciated from a phase diagram where the reduced angular velocity Ω is represented as a function of the reduced angular momentum Λ [4]. These two dimensionless quantities are connected to the angular velocity ω and the angular momentum L_z, defined as the expectation value of the angular momentum operator $\hat{L}_z$ for a rotation around the z axis, by:

$$\Omega \equiv \sqrt{\frac{m\rho_0 R^3}{8\sigma}}\,\omega \qquad\qquad \Lambda \equiv \frac{1}{\sqrt{8\sigma m\rho_0 R^7}}\,L_z \tag{5.1}$$

where m is the mass of the species forming the condensate, σ the surface tension of the liquid, ρ_0 its bulk number density and R the sharp radius of a droplet with N atoms and zero angular momentum (therefore, perfectly spherical), defined such that $4\pi R^3\rho_0/3 = N$.
The configurations of rotating superfluid droplets lie on two possible branches [54]:

- an ascending branch corresponding to oblate axisymmetric shapes that are not able to rotate around their symmetry axis since this is quantum-mechanically forbidden. The only way the angular momentum to be stored is by nucleation of quantized vortices;
- a descending branch describing prolate deformed configurations whose shapes are determined by a combination of both capillary waves and vortices.

Classical droplets undergoing a rigid body rotation (RBR) follow a universal stability diagram [10] that is represented by the red solid line in Figure 5.1: starting from the left branch and increasing Λ the droplets become more oblate, up to $\Lambda \simeq 1.2$ when they assume prolate shapes (pseudotriaxial, ellipsoids, capsules, dumbbells). The analysis of superfluid droplets rotating solely through capillary waves shows the presence of a new branch in the stability diagram, the blue solid curve in Figure 5.1, that deviates from the classical results. According to the above discussions, quantized vortices are the only way to store angular momentum in axisymmetric (oblate) superfluid droplets, while they give a combined contributions together with capillary waves in prolate superfluid droplets. It was found that the shapes of these pure quantum-mechanical systems show a surprising qualitative agreement with the shapes of classical droplets rotating with the same angular velocity. These results recently received an experimental confirmation with the study of rotating ^{4}He droplets with $N = 10^9 - 10^{11}$ atoms [15]. The measure of the angular frequency and the angular momentum of three configurations yields the black points in Figure 5.1, which fall onto the classical diagram.
Our goal is to discover if also quantum droplets made of binary Bose mixture, once set into rotation, present the same behaviour described by the universal diagram that has just been described: in this chapter we will present and discuss the results.
We will start by defining the minimal size a droplet must have in order to host at least one singly-quantized vortex in its interior. After that, a general discussion of the numerical methods necessary

to study a rotating quantum system will be provided, focusing on two kinds of simulations that allow to explore the two branches of the (Ω, Λ) phase diagram. We will present the results of the analysis of the rotation of a trapped ^{41}K-^{87}Rb mixture in the *SF* regime, highlighting analogies and differences with the very well known case of a ^{4}He rotating bucket. The last part is devoted to the discussion of the rotation of ^{41}K-^{87}Rb quantum droplets.

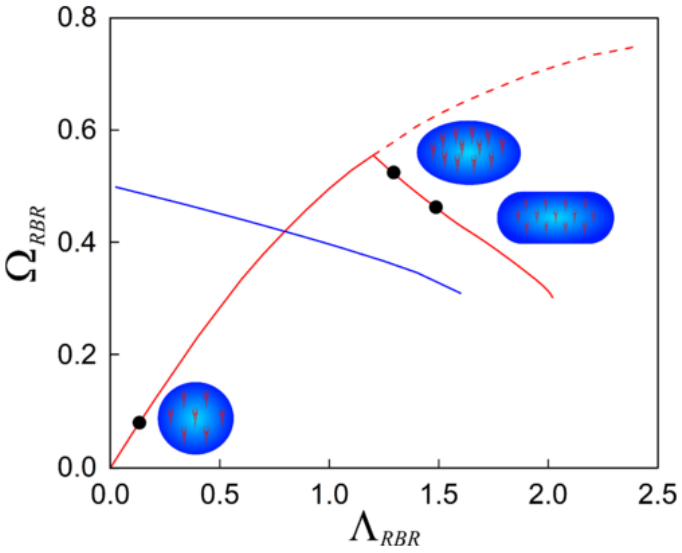

Figure 5.1: Stability diagram for droplets under rotation. Red solid lines indicate stable shapes for a given angular velocity and angular momentum: oblate axisymmetric shapes lie on the left branch, while prolate shapes on the right one. The red dashed curve represents the unstable portion of the branch. The blue line shows the Ω-Λ relation for spinning pure superfluid droplets (i.e. in the absence of vortices): they have necessary prolate shapes. Black circles show the locations of classical droplets with the same aspect ratios as the superfluid ^{4}He droplets that were experimentally studied. Figure taken from [15].

5.1 Critical sizes

In Chapter 4 we studied the presence of vortices inside a uniform ^{41}K-^{87}Rb mixture: it was realized both in the *self-bound* regime, using a cylindrical geometry, and in the *uniform superfluid* one. Now we want to focus on the analysis of vorticity inside self-bound quantum droplets made of binary Bose mixtures. A first important information, that can be very useful for experimental realizations of these systems, is related to the critical size of droplets with embedded vorticity: this is the minimum number of atoms a droplet has to be made of in order to host a given configuration of vortices and remain stable. We start with the "double" vortex configuration, the one denoted with $V_{(1+2)}$ in Chapter 4. For a fixed a_{12} and a given total number of particles $N = N_1 + N_2$, one vortex line for each species is inserted in the droplet at the center of the x-y plane, aligned along the z direction, by means of the imprinting procedure and then the system is let evolve in imaginary time in order to find the lowest energy stationary state. The analysis of the minimizations allows to identify three regions:

- **unstable region**: for a low number of particles the droplet is too small to host both the vortices, in fact they are expelled during the relaxation and the system converges to the stable droplet;

- **metastable region**: during the evolution in imaginary time the system stabilizes to a stationary configuration with the two vortices, where the total energy remains constant for a corresponding time of about 5 ms. This is not a stable solution, however, because eventually the vortices are expelled and the droplet relaxes to the vortex-free configuration. This region is a good candidate for an experimental observation;

- **stable region**: the minimization ends with the convergence of the system towards a stationary configuration with the droplet hosting the two vortex lines aligned along the z-direction and located at the origin of the x-y plane.

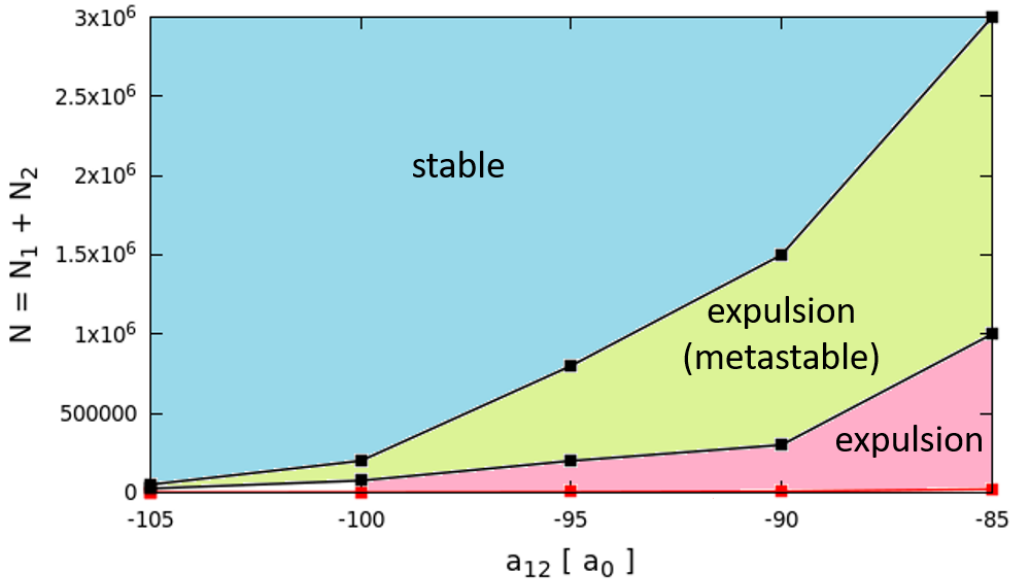

Figure 5.2: Phase diagram for the size of minimal droplets to host a vortex in each of the two species. The red curve at the bottom of the diagram represents the critical size for droplet stability in the absence of vortices.

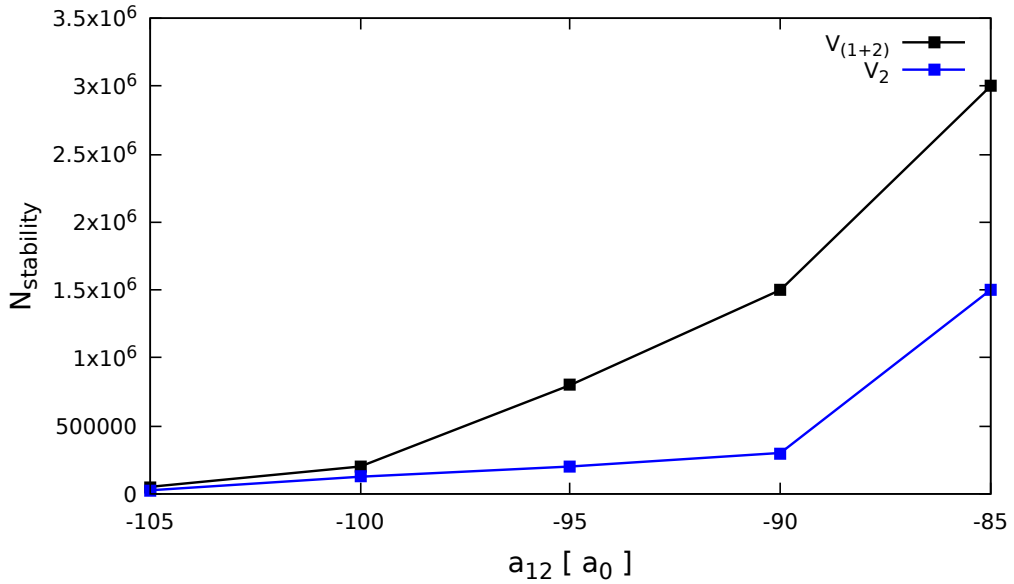

Figure 5.3: Phase diagram for the size of minimal droplets hosting a stable vortex configuration: the blue curve related to two vortices, one in each species, is compared to the black one, relative to one vortex in the second species alone.

At the end of this procedure, one obtains a phase diagram like the one shown in Figure 5.2. The two black curves correspond to the critical line for metastability (the lower one) and the critical line for stability (the upper one). The red curve at the bottom represents the critical size N_c for droplet stability against evaporation: it is almost invisible since there is a difference of about three order of magnitudes with the sizes that come into play here. This fact, together with the strongly increasing behaviour of the two critical curves as $|a_{12}|$ decreases, suggest that these self-bound systems appear "fragile" with respect to the presence of vortices, especially close to the *SF*-to-*droplet* transition value for a_{12}: the only way to host the two vortices is to sensibly increase the droplet size.

The same procedure is then repeated by imprinting only one vortex in the second species: this is the configuration denoted as V_2 in Chapter 4. The results are different in this case, in fact there is not any metastable region any more and the critical sizes are definitely smaller with respect to the previous situation. This appears evident by looking at Figure 5.3 where the critical curve of stability for the V_2 configuration remains significantly lower than the one for $V_{(1+2)}$. This result is consistent with the analysis carried out in Chapter 4 showing that the core sizes shrink when passing from two vortices to one vortex in a single species: of course, narrower vortex cores can be hosted by smaller droplets.

5.2 Numerical methods for rotations

Let's consider a quantum droplet that is rotating along the z axis with a constant angular velocity ω. To study this system it is convenient to work in the fixed-droplet reference frame, that is the corotating frame, with Hamiltonian:

$$\hat{H}' = \hat{H} - \omega \hat{L}_z \tag{5.2}$$

where $\hat{H}$ is the Hamiltonian in the laboratory frame, while $\hat{L}_z = -i\hbar \left(x \frac{\partial}{\partial y} - y \frac{\partial}{\partial x} \right)$ is the angular momentum operator in the z-direction. In the case of binary Bose mixtures, stationary configurations are obtained by solving the following set of equations for the two species

$$\begin{cases} \left\{ H_1[\rho_1, \rho_2] - \omega \hat{L}_z \right\} \psi_1(\vec{r}) &= \mu_1 \psi_1(\vec{r}) \\ \left\{ H_2[\rho_1, \rho_2] - \omega \hat{L}_z \right\} \psi_2(\vec{r}) &= \mu_2 \psi_2(\vec{r}) \end{cases} \tag{5.3}$$

where $H_i[\rho_1, \rho_2]$ $(i = 1, 2)$ are the Hamiltonians entering the GP eqs. (2.37). In the following we will keep the formalism of a one-species BEC to simplify the notation.
The minimization of the energy functional in the corotating frame can proceed through two different algorithms, depending on whether the rotational frequency or the total angular momentum is kept fixed. These two methods turn out not to be equivalent and they both have to be used in order to explore the whole (Ω, Λ) phase diagram, as we are going to explain.

5.2.1 Fixed-ω simulations

The ground state configuration in the corotating frame is obtained by performing an imaginary time evolution using the Hamiltonian in Eq. (5.2), where ω is the fixed value for the rotational angular velocity. Once at convergence, the total angular momentum of the system is computed as:

$$\langle \hat{L}_z \rangle = \langle \psi | \hat{L}_z | \psi \rangle = \int d\vec{r}\, \psi^*(\vec{r}) \hat{L}_z \psi(\vec{r}) \tag{5.4}$$

This algorithm allows to explore only the oblate branch, characterized by axisymmetric droplets with embedded vorticity. The starting wave function is obtained by means of the imprinting procedure (for N_v vortex lines parallel to the z axis) introduced in Chapter 4:

$$\psi^{ini}(\vec{r}) = \sqrt{\rho_0(\vec{r})} \prod_{k=1}^{N_v} \frac{\left(x - x_v^{(k)}\right) + i \left(y - y_v^{(k)}\right)}{\sqrt{\left(x - x_v^{(k)}\right)^2 + \left(y - y_v^{(k)}\right)^2}} \tag{5.5}$$

5.2.2 Fixed-L_z simulations

The Hamiltonian to be used in the imaginary time evolution is still the one in Eq. (5.2), but now the total angular momentum is fixed to a constant value L, while the angular velocity ω must be updated at each iteration. The starting angular velocity is set to $\omega_0 = L / I$, where I is the rigid body moment of inertia, and the rule for updating the angular velocity is

$$\omega_{\text{new}} = \omega_{\text{old}} \frac{\langle \hat{L}_z \rangle}{L} \tag{5.6}$$

where $\hat{L}_z$, given in Eq. (5.4), must be computed separately before updating ω. This method is robust but slow.

An alternative scheme is based on the **Augmented Lagrangian method** (**ALM**) [55], which consists in minimizing the energy using the Hamiltonian

$$\hat{H}' = \hat{H} - \left[\omega - \mu \left(\langle \hat{L}_z \rangle - L\right)\right] \hat{L}_z \tag{5.7}$$

and updating the angular velocity according to

$$\omega_{\text{new}} = \omega_{\text{old}} - \mu \left(\langle \hat{L}_z \rangle - L\right) \tag{5.8}$$

where μ is an arbitrary positive number which controls the rate of convergence towards the imposed value L. This method is very fast, the only problem might arise in searching for the optimal value of μ by trial-and-error.

The fixed-angular momentum algorithm allows to explore both the branches of the phase diagram, but we will apply it to the prolate one where angular momentum is stored in capillary waves and in vorticity. The effective starting wave function is a superposition of a quadrupolar small distortion and N_v vortex lines parallel to the z axis:

$$\psi^{ini}(\vec{r}) = \sqrt{\rho_0(\vec{r})}\, e^{i\,\epsilon\, xy} \prod_{k=1}^{N_v} \frac{\left(x - x_v^{(k)}\right) + i\,\left(y - y_v^{(k)}\right)}{\sqrt{\left(x - x_v^{(k)}\right)^2 + \left(y - y_v^{(k)}\right)^2}} \tag{5.9}$$

with ϵ a small parameter accounting for the degree of deformation. The velocity field computed from this kind of ansatz

$$\vec{v} = \frac{\hbar}{m} \text{Im}\left(\frac{\vec{\nabla}\psi}{\psi}\right) = \epsilon \frac{\hbar}{m} \vec{\nabla}(xy) + \sum_{k=1}^{N_v} \frac{\hbar}{m} \vec{\nabla}\theta_k \tag{5.10}$$

consists of the superposition of a first contribution from capillary waves and a second one from vorticity (θ_k is the phase associated to the k^{th} vortex) and it clearly satisfies $\vec{\nabla} \times \vec{v} = 0$.

5.3 Rotating superfluid cylinder

The study of rotating droplets requires fully 3D numerical simulations that have a high computational cost. As already discussed in Chapter 4, cylindrical geometry restricts numerical calculations to less demanding 2D configurations, while the main physics can still be caught by the model. This is why we focus here on the study of the rotation of a cylinder made of the ^{41}K-^{87}Rb mixture. The interspecies scattering length is set to

$$a_{12} = -70\ a_0 \tag{5.11}$$

so that the system is inside the miscible regime with $\delta g > 0$: we recall that in Chapter 4 we labelled it as the *uniform superfluid* (*SF*) *regime*. Since the system is in the gaseous phase, an harmonic confining potential is thus necessary to confer to it a cylindrical shape.

5.3.1 Starting configuration

The geometrical parameters of the simulation cell are chosen to be

$$x_{max} = y_{max} = 6 \times 10^5 \, a_0 \qquad z_{max} = 4 \times 10^5 \, a_0 \tag{5.12}$$

while the number of atoms for each species is

$$N_1 = 1.0000 \times 10^6 \qquad N_2 = 1.1765 \times 10^6 \tag{5.13}$$

This particular choice for the atom numbers satisfies the *MF optimal ratio* and is such that the maximum densities at the center of the cylinder are one order of magnitude smaller than the ones for $a_{12} = -80 \, a_0$, in the droplet regime. Since the system is not self-bound, we add an external harmonic confining potential along the x and y directions, while the system is not confined in the z direction. Actually there is one trapping potential acting on each species and this corresponds to add to the energy functional in Eq. (2.10) the following term:

$$\mathcal{E}_{ho}[\rho_1, \rho_2] = \frac{1}{2} m_1 \left(\omega_{1,x}^2 \, x^2 + \omega_{1,y}^2 \, y^2\right) \rho_1(\vec{r}) + \frac{1}{2} m_2 \left(\omega_{2,x}^2 \, x^2 + \omega_{2,y}^2 \, y^2\right) \rho_2(\vec{r}) \tag{5.14}$$

Usually, in the experimental procedures [40] the trapping frequencies are chosen in such a way that the two species have the same force constant along each direction, i.e.

$$m_1 \, \omega_{1,\alpha}^2 = m_2 \, \omega_{2,\alpha}^2 \qquad \alpha = x, y \tag{5.15}$$

Moreover, in prevision of a rotation around the z axis, a slight anisotropy is introduced:

$$\frac{\omega_{1,x}}{\omega_{1,y}} = \lambda = 1.1 \tag{5.16}$$

This allows to break the axial symmetry, otherwise the rotation would not have any effect on the system.
Thanks to the above constraints, one is left with only one independent confining frequency, so that the final values are:

$$(\omega_{1,x}, \, \omega_{1,y}) = 2\pi \times (6.50, \, 5.91) \text{ Hz} \qquad (\omega_{2,x}, \, \omega_{2,y}) = 2\pi \times (4.46, \, 4.06) \text{ Hz} \tag{5.17}$$

At this point, an imaginary time evolution provides the ground state of the system that corresponds to the starting configuration. The two-dimensional projection of the total density profile on the x-y plane is represented in Figure 5.4(a): the system is well confined inside the border of the cell and the section of the cylinder is slightly elliptic, as a consequence of the anisotropy of the harmonic confinement. By measuring the radial dimensions of the system in the two transversal directions, R_x, R_y, an estimate of the condensate radius is obtained by means of a geometrical average:

$$R = \sqrt{R_x \, R_y} \simeq 3.116 \times 10^5 \, a_0 \tag{5.18}$$

5.3.2 Minimization in the corotating frame

We want now to set the superfluid cylinder into rotation with a fixed angular velocity that is denoted with Ω. Since our goal is to dynamically nucleate vortices in the rotating superfluid, the angular velocity must be higher than that required to create a single vortex. We can estimate the latter quantity by using the Feynman's formula [32] for the critical value for vortex nucleation:

$$\Omega_c = \frac{\hbar}{m R^2} \ln\left(\frac{R}{d_c}\right) \tag{5.19}$$

For a uniform Bose gas, the size of the core of the vortex, d_c, is of the order of the healing length, Eq. (4.12). For a trapped gas, an estimate of the core size can be obtained from the same healing

length, but substituting for the density of the system the central value of the density in the absence of vortices. In this way, the ratio appearing inside the logarithm in Eq. (5.19) takes the form $R \,/\, d_c \simeq (R \,/\, a_{ho})^2$ [16] where $a_{ho} = \sqrt{\hbar \,/\, m\omega}$ is the harmonic length. In our specific case, considering the geometrical average of the trapping frequencies $\omega = \sqrt{\omega_x\, \omega_y}$, the following estimates for the critical angular velocities for each species are obtained:

$$\Omega_{c,1} \simeq 2.649 \times 10^{-16}\ \mathrm{Ha}/\hbar \qquad\qquad \Omega_{c,2} \simeq 1.500 \times 10^{-16}\ \mathrm{Ha}/\hbar \tag{5.20}$$

Then for our simulation we choose the value:

$$\Omega = 4.700 \times 10^{-16}\ \mathrm{Ha}/\hbar \tag{5.21}$$

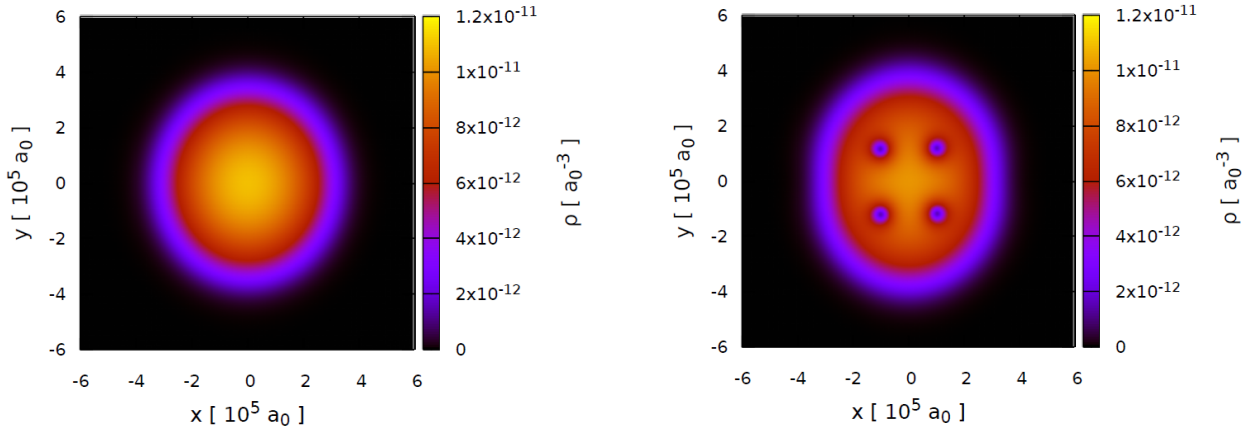

(a) Starting configuration.

(b) Final configuration.

Figure 5.4: 2D total density profiles on the xy-plane of the SF cylinder. On the left the equilibrium profile at rest is shown: it is possible to appreciate a slight quadrupolar deformation due to the anisotropic harmonic potential. The right figure shows the stationary configuration in the corotating frame with angular frequency Ω: the rotation leads to the nucleation of 4 vortices that arrange themselves forming a regular lattice.

The study of rotation is realized looking for the stationary configuration in the frame solidal to the system that is rotating at angular velocity Ω: this is obtained through an evolution in imaginary time in the corotating frame using the fixed-ω algorithm explained in the previous section. During the minimization, the cross section of the cylinder increases its quadrupolar deformation, meaning that capillary waves develop on the surface. However, the most interesting result consists of four vortex lines, parallel to the z axis, that are nucleated at the lateral surface of the cylinder and then enter the bulk region until they reach a stationary position. In the final configuration, that is shown in Figure 5.4(b), these vortex lines are located at the same distance from the rotational axis. For a higher number of vortices, one would expect the formation of a patch of the Abrikosov lattice of vortices that was discussed in Chapter 1.
The total angular momentum generated by the rotation is transferred to the two species in different ways, as one can infer by analyzing the behaviour of the phase of the wave function and the velocity field in the x-y plane for each species.
Angular momentum is stored in the first species only through a quadrupolar deformation that develops capillary waves. The superficial character of these excitations can be seen in the diagram for the phase of the macroscopic wave function $\psi_1(\vec{r})$ (Figure 5.5(a)) where the phase undergoes a weak variation only near the borders of the cylinder, remaining essentially equal to zero in the internal region. This is even more evident from the streamlines associated to the first species that are represented in Figure 5.5(b): the velocity field away from the center corresponds to the one associated to capillary waves, i.e. $\vec{v}_{cap} \propto \vec{\nabla}\,(xy)$, that ends abruptly at the lateral surface [15, 33].

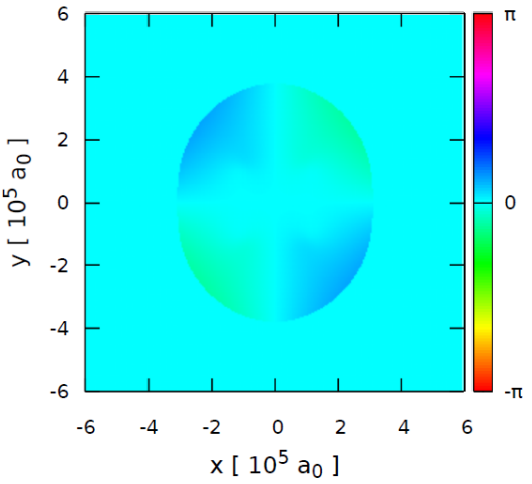

(a) Phase of the wave function $\psi_1(\vec{r})$.

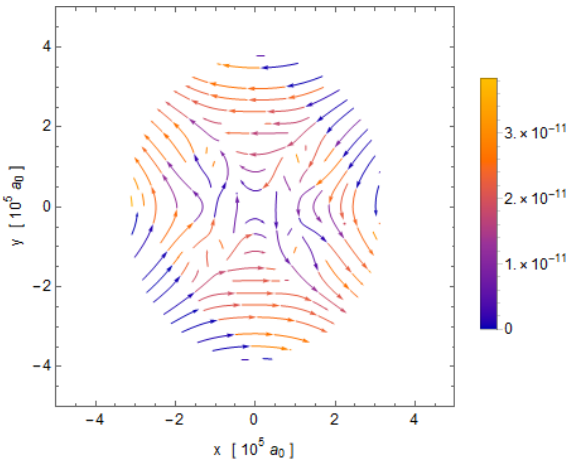

(b) Streamlines for the first species in the x-y plane.

Figure 5.5: Phase of the wave function and streamlines along the x-y plane for the first species. The velocity field is the typical one associated to capillary waves that have a tiny effect on the variation of the phase. The values in the legend of the right plot are expressed in atomic units for velocity.

A change of scenery takes place as far as the second species is concerned: the angular momentum is stored via both capillary waves and vorticity, in fact all the 4 vortex lines nucleated during the rotation belong to this species. The diagram for the phase of the macroscopic wave function $\psi_2(\vec{r})$ (Figure 5.6(a)) is consistent with the phenomenology of a superfluid: for each closed loop around a vortex line the phase changes by 2π, while around a path containing the 4 vortices the phase changes by $4 \times 2\pi$. The presence of the four vortices is highlighted also by the streamlines in Figure 5.6(b) where the velocity field wraps around the whirls: the circulation of the superfluid velocity around a closed path enclosing the four topological defects is exactly equal to 4 (in units of $\hbar/m_2$), while for the first species the same computation yields zero. A comparison with Figure 5.5 shows that, in this second case, the contribution from vorticity is predominant over the one from capillary waves.

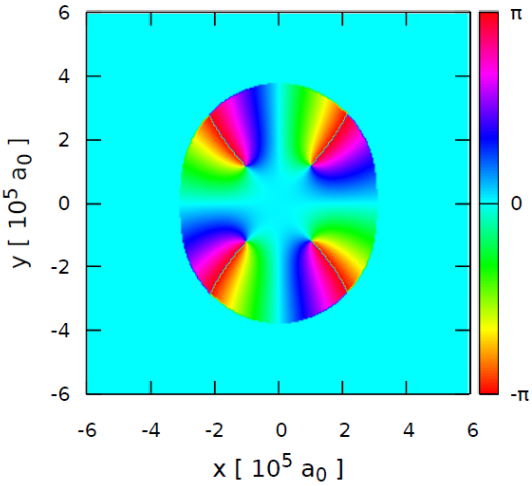

(a) Phase of the wave function $\psi_2(\vec{r})$.

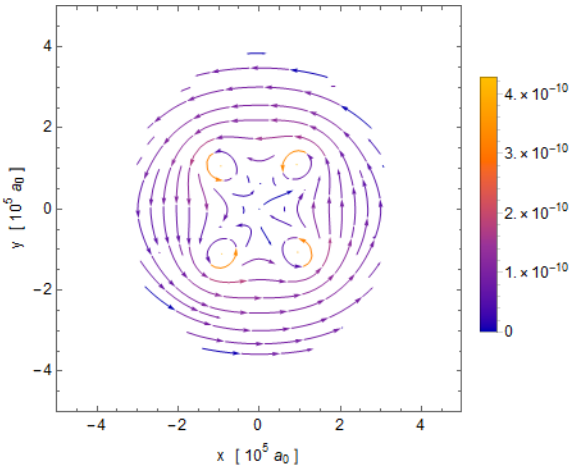

(b) Streamlines for the second species in the x-y plane.

Figure 5.6: Phase of the wave function and streamlines along the x-y plane for the second species. In this case, the most dominant contribution is provided by the four vortex lines, while the one from capillary waves is less relevant. The values in the legend of the right plot are expressed in atomic units for velocity.

5.3.3 Capillary waves contribution to the angular momentum

It can be useful to know, at least approximately, how angular momentum is shared between vortices and capillary waves. Separating the contribution of capillary waves and vortices in the velocity field is not possible in general: the superfluid velocity field, in fact, is proportional to the gradient of the phase of the effective wave function where the two contributions are entangled. Studying the coexistence of one single vortex and a quadrupolar irrotational flow in an elliptic cylinder [33], Fetter was able to determine how the angular momentum is shared between the vortex and the quadrupolar deformation by decomposing the phase of the wave function into the sum of a term arising from the vortex line and another from the quadrupolar flow. Following this idea, we extend the guess we made in Eq. (5.10) (that was valid only for the initial wave function) and we try to estimate the angular momentum associated to capillary waves, L_{cap}: two approaches are followed.

The first method is based on the numerical results from the DFT code. Denoting with d_i, $(i = 1, 2, 3, 4)$ the distance of each vortex line from the rotational axis, the contribution to angular momentum from vorticity can be obtained from [56] as:

$$L_{vort} \;=\; \hbar\, N_2 \sum_{i=1}^{4} \left(1 - \frac{d_i^2}{R^2}\right) \tag{5.22}$$

with R given in Eq. (5.18). L_{cap} can then be found from the total angular momentum $\langle \hat{L}_z \rangle$:

$$L_{cap} \;=\; \langle \hat{L}_z \rangle \;-\; L_{vort} \tag{5.23}$$

The second method corresponds to the theoretical prevision, described in Section 1.5, according to which the angular momentum associated to surface capillary waves [16] is

$$L_{cap} \;=\; \Theta_{\rm irr}\, \Omega \;=\; \Theta_{\rm rig}\, \varepsilon^2\, \Omega \tag{5.24}$$

The explicit expressions for the rigid body moment of inertia, $\Theta_{\rm rig}$, and the deformation parameter, ε, are given by Eqs. (1.71, 1.74).
The generalization to a binary Bose mixture implies that Eq. (5.24) is valid for each species and then the total value of L_{cap} is given by the sum of the two contributions.

The estimates for the angular momentum per atom using the above two methods are compared in Table 5.1: considering the approximations employed in this analysis, the numerical results are consistent with the theoretical previsions. Moreover, they confirm that the contribution from vorticity is the predominant one.

	$L_{cap,1}/N_1 \quad [\hbar]$	$L_{vort,1}/N_1 \quad [\hbar]$	$L_{cap,2}/N_2 \quad [\hbar]$	$L_{vort,2}/N_2 \quad [\hbar]$
DFT numerical results	7.6767×10^{-2}	0	1.8153×10^{-1}	3.4940
theoretical previsions	6.8699×10^{-2}	0	1.5087×10^{-1}	3.0004

Table 5.1: Contributions to the angular momentum per particle from capillary waves and vorticity for both species. The numerical estimates are compared to the theoretical approximations, as explained in the text.

5.3.4 Real-time dynamics

The stationary configuration in the corotating frame is then taken as the sarting one for a dynamics in real time with $\Omega = 0$. This corresponds to put ourselves in the laboratory frame, therefore we expect the system to rotate with constant angular velocity Ω. This is verified, in fact the cylinder comes back to the starting point after a period

$$\tau \;=\; 2\pi/\Omega \;\simeq\; 323.37 \text{ ms} \tag{5.25}$$

However, the two mixtures alone do not rotate *à la* rigid body and the total angular momentum is not perfectly conserved. In the laboratory the harmonic trap is rotating with frequency Ω and, due to its anisotropy, exerts a torque on the condensate inducing the velocity field typical of capillary waves. This torque is responsible for the oscillation of the total angular momentum during the dynamics.
If the condensate were stable even in the absence of the trap, after the confinement is switched off one would observe the ellipsoid (with this term we mean a *cylinder* with an elliptic cross section) rotating around the z axis like a rigid body. Notice, however, that this is a misleading *apparent* rotation in the sense that the velocity field is strictly irrotational, while the vorticity for a rigid body is $\vec{\nabla} \times \vec{v} = 2\vec{\Omega}$. The motion of a fluid is a combination of translation, rotation and deformation of the fluid elements, and only when the vorticity is non zero, one may speak of a true rotation, being important to distinguish between rotation and motion of the fluid elements along a curved path, e.g., around a vortex core.
This macroscopic rotation has a qualitative explanation in the fact that the capillary waves streamlines are normal to the lateral surface: the flow of these streamlines corresponds to a rotation of the ellipsoid.
This situation is deeply different from the one where angular momentum is conserved only through the nucleation of vortices: in this latter case only the lattice of vortices is rotating and the vorticity tends to the classical value $\vec{\nabla} \times \vec{v} = 2\vec{\Omega}$, as it was shown by Feynman [32].

5.4 Rotating droplets phase diagram

For a Bose mixture made of two species we can define the total mass density as $\rho_m = m_1\rho_1 + m_2\rho_2$, where ρ_1, ρ_2 are the single-species bulk number densities. The sharp radius is

$$R = \left[\frac{3\,(N_1 + N_2)}{4\,\pi\,(\rho_1 + \rho_2)}\right]^{1/3} \tag{5.26}$$

and the conversions to dimensionless angular momentum and frequency, given in Eq. (5.1), have the explicit form

$$\Omega \equiv \sqrt{\frac{(m_1\rho_1 + m_2\rho_2)R^3}{8\sigma}}\,\omega \qquad\qquad \Lambda \equiv \frac{1}{\sqrt{8\sigma(m_1\rho_1 + m_2\rho_2)R^7}}\,L_z \tag{5.27}$$

where the surface tension σ contains the curvature correction, as discussed in Chapter 3.

Focusing on the ^{41}K-^{87}Rb mixture, we fix the interspecies scattering lenght to

$$a_{12} = -105\ a_0$$

and we study rotating droplets with different geometries and number of vortices

$$N_v = 0,\ 1,\ 2,\ 3$$

imprinted only in the second species. These choices are justified by the results found in Chapter 4: core sizes are smaller in this configuration, therefore one can deal with droplets with a reasonable number of atoms $N = N_1 + N_2$. Clearly, the higher the number of vortices, the larger the droplet size. In particular, it is chosen $N = 100\,000$ for $N_v = 0, 1$ and $N = 1\,500\,000$ for $N_v = 2, 3$: this difference in the atom number should not affect the results of the stability diagram, since the rescaled quantities are introduced in order to get rid of dimensional effects. We recall that the numbers of atoms for each species (N_1, N_2) satisfy the *MF optimal ratio*.
We look for the stationary states of these droplets in the rotating frame, therefore we make use of the numerical methods described in Section 5.2. The vortex-free configurations are entirely explored by means of the ALM algorithm, consistently with the fact that they are expected to assume prolate shapes associated to capillary waves. For the remaining $N_v \neq 0$ configurations, instead, both the

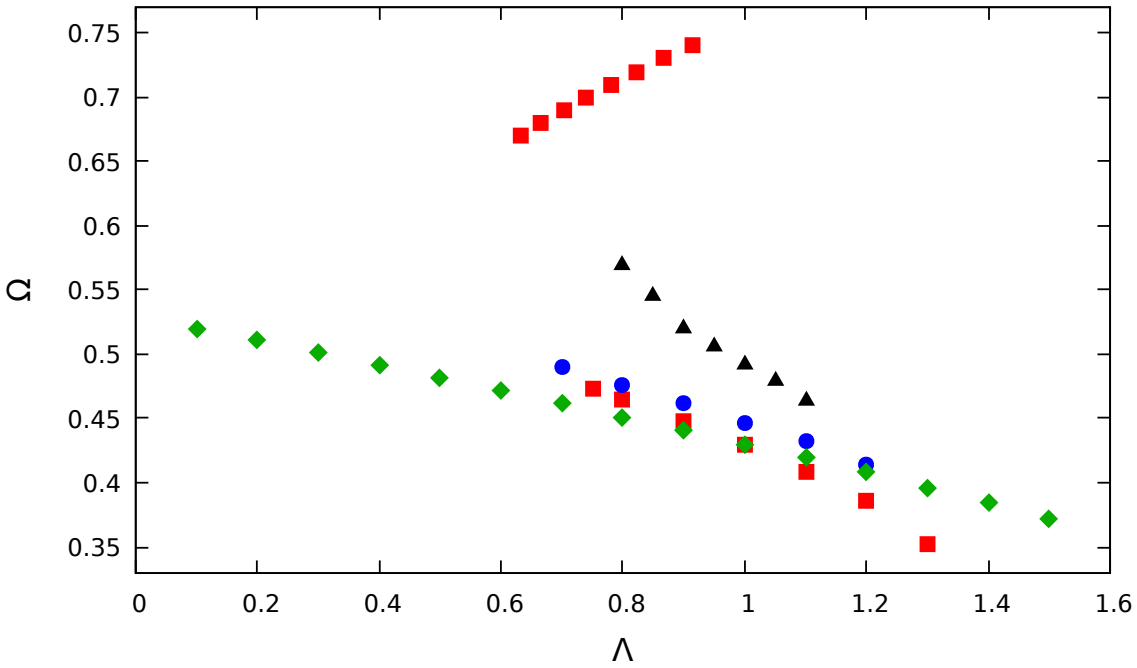

Figure 5.7: Rescaled angular velocity Ω *vs.* rescaled angular momentum Λ. Green diamonds: vortex-free configurations. Red squares: 1-vortex configurations. Blue dots: 2-vortices configurations. Black triangles: 3-vortices configurations.

oblate and prolate branches are investigated with their suitable algorithms.

The results of this analysis are collected in the phase diagram of Figure 5.7, where the dimensionless angular velocity Ω is plotted as a function of the dimensionless angular momentum Λ.
Green diamonds refer to droplets without vortices: they form a branch that starts from very low values of Λ and is compatible with the blue curve in Figure 5.1. As expected, they assume prolate shapes with corresponding capillary waves: the 2D density profiles on the x-y and x-z symmetry planes for $\Lambda = 0.5$ are shown in Figure 5.8.
The red squares correspond to configurations with $N_v = 1$ that present two distinct branches. The ascending one is formed by oblate axysimmetric droplets (as it is shown in Figure 5.9), while prolate drops (Figure 5.10) give rise to the descending one. The origin of the oblate branch is not clear, yet: one would expect, in fact, the total angular momentum to be independent of the angular velocity, remaining fixed at the value $\langle \hat{L}_z \rangle = N_2 \hbar$.
Blue points and black triangles are associated to prolate droplets with, respectively, $N_v = 2$ and $N_v = 3$ vortices: the vortex lines form a linear array in the x-y plane, as one can see in Figures 5.11-5.12.
Actually, during the minimization procedure a certain degree of instability is displayed by each of the states analyzed above: in practice it is difficult to achieve a true convergence in the total energy and in the angular velocity. Such an instability is probably due to the fact that the center of mass of these droplets is not fixed and it may wander through the simulation cell during the relaxation. Even if, strictly speaking, we have to talk about "metastable" states, for the moment we believe the derived results to be consistent.
Moreover, the analysis of the oblate branch for $N_v = 2, 3$ configurations does not yield any stationary state since droplets are subjected to fragmentation. Differently from the above considerations, this situation corresponds to a true instability related to a droplet size that is too small for the vortical patterns we want to study. Such an instability is then in agreement with some previous studies that analyzed the creation of self-trapped vortex rings inside a 3D superfluid droplet with embedded topological charges m_1, m_2 of the two components [57]. The main result was the discovery of broad stability regions for vortex droplets with $m_1 = m_2 = 1$ and narrower ones for $m_1 = m_2 = 2$ (i.e.

double quantized vortices in each species): configurations with 2 and 3 vortices off-axis, thus, are not expected to be stable. An external confining potential should be introduced to stabilize the droplets and better understand their rotational properties.
Let's focus for a moment on the three prolate branches in Figure 5.7. For a given value of Λ, the more the number of vortices, the higher the corresponding angular velocity Ω. Making a comparison with Figure 5.1, by increasing N_v the prolate branches get closer to the stability diagram for classical viscous droplets: this is perfectly consistent with the picture proposed by Feynman (described in Section 1.4) and, more important, with the results for rotating ^{4}He nanodroplets.

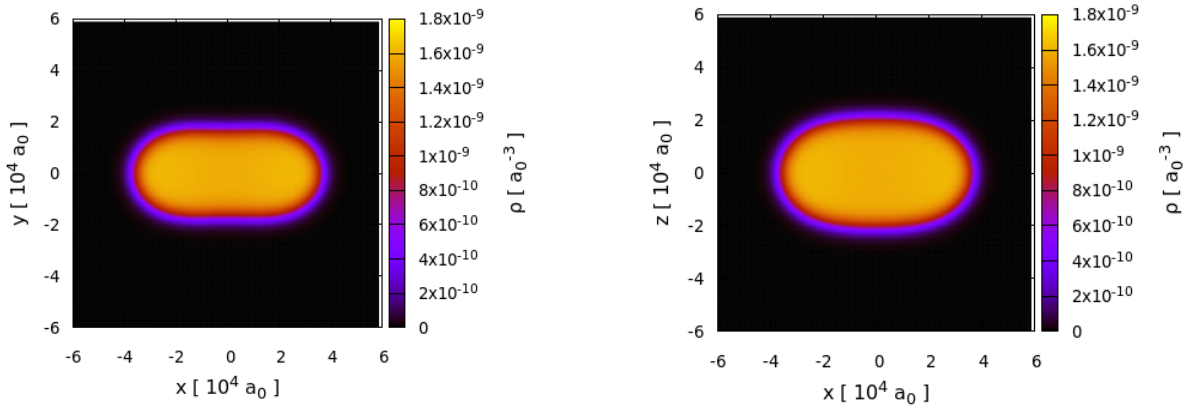

(a) x-y symmetry plane.

(b) x-z symmetry plane.

Figure 5.8: Two-dimensional projections of the total density for the $N = 100\,000$ droplet hosting $N_v = 0$ vortices at $\Lambda = 0.5$. Angular momentum is stored only by means of capillary waves associated to quadrupolar deformations.

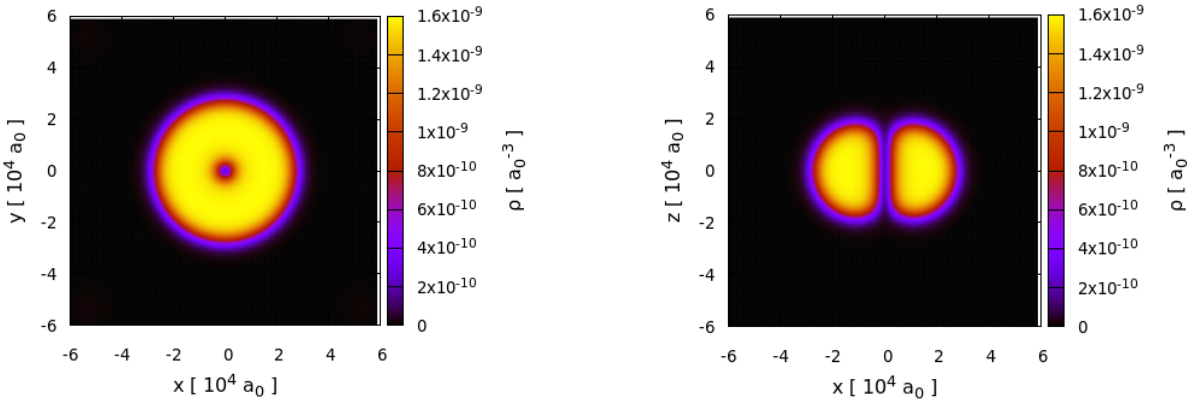

(a) x-y symmetry plane.

(b) x-z symmetry plane.

Figure 5.9: Two-dimensional projections of the total density for the oblate axisymmetric configuration of a $N = 100\,000$ droplet hosting $N_v = 1$ vortices at $\Lambda = 0.7$.

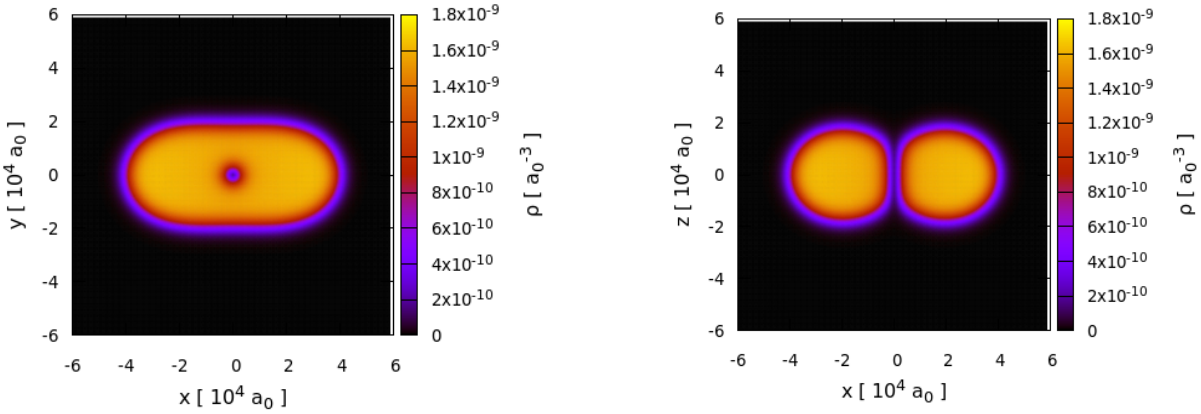

(a) x-y symmetry plane.

(b) x-z symmetry plane.

Figure 5.10: Two-dimensional projections of the total density for the prolate configuration of a $N = 100\,000$ droplet hosting $N_v = 1$ vortices at $\Lambda = 1.0$.

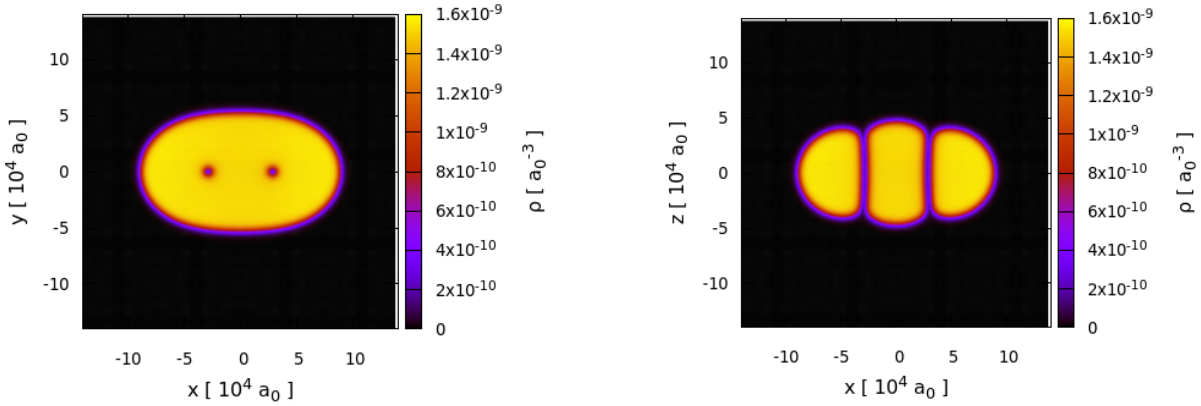

(a) x-y symmetry plane.

(b) x-z symmetry plane.

Figure 5.11: Two-dimensional projections of the total density for the prolate configuration of a $N = 1\,500\,000$ droplet hosting $N_v = 2$ vortices at $\Lambda = 0.8$.

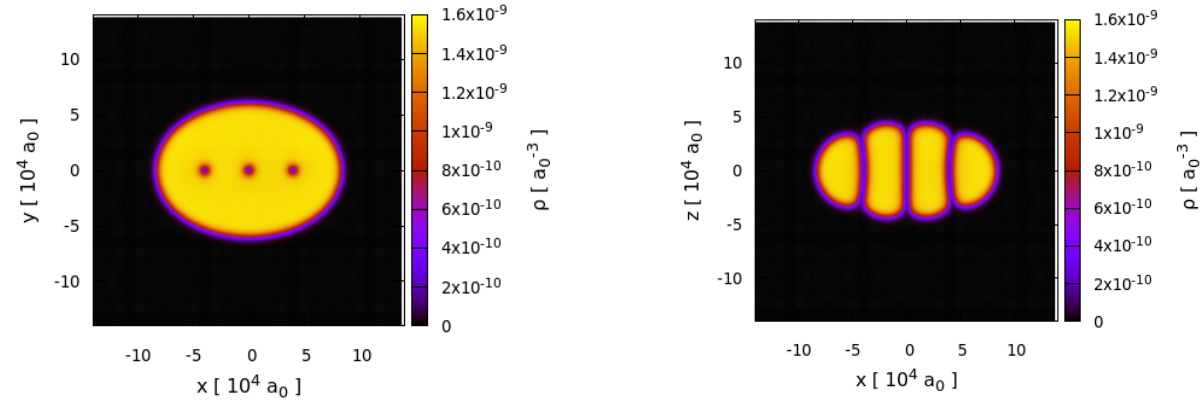

(a) x-y symmetry plane.

(b) x-z symmetry plane.

Figure 5.12: Two-dimensional projections of the total density for the prolate configuration of a $N = 1\,500\,000$ droplet hosting $N_v = 3$ vortices at $\Lambda = 0.8$.

Summary and conclusions

In this thesis work we considered a bosonic ^{41}K-^{87}Rb mixture of Bose-Einstein condensates with tunable interspecies interaction in the self-bound regime by means of numerical simulations based on the Density Functional Theory. The competition between the attractive mean field term and the repulsive beyond mean field Lee-Huang-Yang correction leads to the formation of self-bound droplets with extremely low densities compared to any other existing liquid.
We found that the surface properties of self-bound droplets in free space are related to the total number of atoms N they are made of: both the curvature correction to the surface tension and the stability of droplets against evaporation depend on it.
We studied the development of vorticity inside the ^{41}K-^{87}Rb mixture in the self-bound regime, starting with the uniform system where a cylindrical geometry was employed to reduce to less demanding 2D computations. We observed that the vortex kinetic energy deviates from the hydrodynamic approximation in the region of the core, noticing how the core sizes reduce as the interspecies interaction becomes more attractive. Different vortical configurations were analyzed and, as far as the vortex excitation energies are concerned, we showed that the configurations with vortices inside the denser species is the most energetically favourable. It is worth mentioning that, in the presence of a vortex line in one component alone, the density of the vortex-free species forms a sort of "fake" core on top of the "real" vortical one.
The results for the uniform system provided a good starting point for the exploration of the rotational properties of a self-bound droplet. First, a stability analysis revealed that the configuration with one vortex in the second species is the easiest one to be hosted by a droplet. This was also confirmed by the study of the rotation of a trapped mixture in the *SF* regime, where we were able to highlight analogies and differences with the very well known case of a rotating superfluid ^{4}He bucket.
Finally, the (Ω, Λ) phase diagram seems to be compatible with the one for rotating superfluid ^{4}He nanodroplets as far as vortex-free and prolate droplets with embedded vorticity are concerned. At the same time, however, oblate axisymmetric droplets with 2 and 3 vortices are unstable under fission.

This work could open new possibilities, both under a theoretical and experimental point of view.
On the one hand, these last results for spinning droplets can be refined by introducing a constraint on the center of mass position, while an external confinement could allow to study oblate axisymmetric configurations with 2 and 3 vortices. As a future perspective, more accurate first-principle quantum Monte Carlo (QMC) algorithms, like the ones in [58], could be used to study these issues.
On the other hand, we believe that this study could be helpful for the interpretation of the results coming from possible future experiments on rotating droplets. In particular, an experimental realization of droplets with finite angular momentum (and, in case, vortices) could proceed as follows: at the beginning the mixture in the *SF* regime is set into rotation by means, for instance, of a slightly elliptic external trap; after that, a quench into the *droplet* regime is realized together with the releasing of the trapping potential.

Appendix A

Low-energy collisions and scattering length

In this Appendix we will recall some basic features of the theory of elastic scattering of slow particles following the discussion in [16]: a detailed analysis of the scattering problems, specifically for ultra-cold gases, can be found in Refs. [22-24].
Assuming that the two-body interaction can be described by a spherically-symmetric potential $V(r)$, the scattering problem for two non-relativistic particles consist in finding the solution of the Schroedinger equation

$$\left(-\frac{\hbar^2}{2m}\vec{\nabla}^2 + V(r)\right)\psi(\vec{r}) = E\,\psi(\vec{r}) \tag{A.1}$$

for the relative motion with positive energy ($E > 0$). Here $\vec{r} = \vec{r}_1 - \vec{r}_2$ and $m = m_1 m_2/(m_1 + m_2)$ is the reduced mass of the two atoms. Being r_0 the range of the potential, in the asymptotic region $r \gg r_0$ the solution can be written as

$$\psi(\vec{r}) = e^{ikz} + f(\theta)\,\frac{e^{ikr}}{r} \tag{A.2}$$

where $k = \sqrt{\frac{2mE}{\hbar^2}}$ and θ is the angle between the direction of $\vec{r}$ and the z-axis. The function $f(\theta)$ is called the *scattering amplitude* and it depends, in general, on the scattering energy E; however, in the low energy limit, it becomes a constant independent of both E and θ:

$$\lim_{E\to 0} f(\theta) = -a \tag{A.3}$$

a is called the *s-wave scattering length*, it is determined by the interatomic potential $V(r)$ and it is a crucial quantity in the scattering processes at low energies. In the case of fully polarized bosons, with an even total spin, the scattering amplitude determines the scattering cross-section according to

$$d\sigma = |f(\theta) + f(\pi-\theta)|^2\, d\Omega \qquad\qquad 0 \le \theta \le \pi/2 \tag{A.4}$$

This means that in the low energy limit $E \to 0$ the total cross section will approach the value

$$\sigma = 8\pi a^2 \tag{A.5}$$

The scattering amplitude can be calculated expanding the wave function with respect to the values of the angular momentum l

$$\psi(\vec{r}) = \sum_{l=0}^{\infty} P_l(\cos\theta)\,\frac{\chi_{kl}(r)}{kr} \tag{A.6}$$

where P_l are the Legendre polynomials and the radial functions $\chi_{kl}(r)$ satisfy the equation

$$\frac{d^2\chi_{kl}}{dr^2} - \frac{l(l+1)}{r^2}\chi_{kl} + \frac{2m}{\hbar^2}\left(E - V(r)\right)\chi_{kl} = 0 \tag{A.7}$$

In the large distances limit $r \gg r_0$, they take the general form

$$\chi_{kl}(r) \;=\; A_l \,\sin\left(kr \,-\, \frac{\pi l}{2} \,+\, \delta_l\right) \tag{A.8}$$

where $\delta_l(k)$ is the so-called phase shift. Using the expansion of the exponent e^{ikz} in terms of Legendre polynomials and choosing $A_l \;=\; (2l+1)i^l e^{i\delta_l}$, one easily obtains

$$f(\theta) \;=\; \frac{1}{2ik}\sum_{l=0}^{\infty}(2l+1)\,P_l(\cos\theta)\,\left(e^{2i\delta_l}-1\right) \tag{A.9}$$

The phase shift δ_l can be explicitly computed solving Eq. (A.7) and the situation is simple for low-energy solutions satisfying the condition $kr_0 \;\ll\; 1$. For distances $r \;\ll\; 1/k$ one can set $E \;=\; 0$ and restrict to the $l \;=\; 0$ case, so that the reduced equation becomes

$$\frac{d^2\chi_{k0}}{dr^2} \;-\; \frac{2m}{\hbar^2}V(r)\chi_{k0} \;=\; 0 \tag{A.10}$$

The solution of Eq. (A.10) should be matched with the asymptotic form Eq. (A.2) in the region

$$r_0 \;\ll\; r \;\ll\; \frac{1}{k} \tag{A.11}$$

In the region $r \;\gg\; r_0$ the interaction term can be neglected and the solution takes the linear form

$$\chi_{k0} \;=\; c_0\,(1 \,-\, \kappa r) \tag{A.12}$$

where κ depends on the choice of $V(r)$. Then, if $kr \;\ll\; 1$, Eq. (A.2) can be expanded yielding the same form of Eq. (A.12) with $c_0 = e^{i\delta_0}\sin\delta_0$ and

$$\kappa \;=\; -k\,\cot\delta_0 \tag{A.13}$$

As $k \to 0$, Eq. (A.13) yields the linear law

$$\delta_0 \;=\; -\frac{k}{\kappa} \tag{A.14}$$

At higher values of l the phase shift behaves like $\delta_l \;\propto\; k^{2l+1}$; this means that, if $k \to 0$, only the $l = 0$ term survives and the scattering length can be identified through the relation

$$a \;=\; -\frac{\delta_0}{k} \;=\; \frac{1}{\kappa} \tag{A.15}$$

Consequently, the wave function in the region of Eq. (A.11) has the form

$$\psi_{k0} \;=\; c_0\,\left(\frac{1}{r} \,-\, \frac{1}{a}\right) \tag{A.16}$$

Notice that the above considerations can be presented replacing the real two-body potential $V(r)$ with a "pseudopotential" that describes a regularized contact interaction:

$$\hat{V}_{ps}(r) \;=\; g\,\delta(\vec{r})\,\frac{d}{dr}r \tag{A.17}$$

The wave function in Eq. (A.16) has to satisfy Eq. (A.1) with $E = 0$

$$\begin{aligned} 0 \;\stackrel{!}{=}\; \left(-\frac{\hbar^2}{2m}\vec{\nabla}^2 \,+\, \hat{V}_{ps}(r)\right)\psi_{k0}(\vec{r}) \;&=\; -\frac{\hbar^2}{2m}c_0\underbrace{\vec{\nabla}^2\left(\frac{1}{r}\right)}_{-4\pi\delta(\vec{r})} + g\,\delta(\vec{r})\,c_0\,\left(\frac{1}{r} \,-\, \frac{1}{a} \,-\, \frac{1}{r}\right) \\ &=\; \delta(\vec{r})\,c_0\,\left(\frac{2\pi\hbar^2}{m} \,-\, \frac{g}{a}\right) \end{aligned} \tag{A.18}$$

This fixes a condition on the coupling constant that is directly related to the s-wave scattering length:

$$g = \frac{2\pi\hbar^2}{m}a \tag{A.19}$$

This is the justification for the shape of the two-body potential for a weakly interacting Bose gas in Chapter 1, where we have seen that the scattering length is the crucial interaction parameter of the theory. The value of a is available using several experimental techniques and it can span a very wide range of values. It can be positive or negative, and in some cases it can also be tuned by means of Feshbach resonances: this gives the possibilities for manipulating the interaction between atoms.

Appendix B

Numerical methods

The Gross-Pitaevskii equations coming out from the energy functional that describes binary Bose mixtures are solved by means of numerical methods: this Appendix is devoted to the explanation of the main tools characterizing the numerical codes that are employed.

B.1 Simulation domain

GP Eqs. (2.37, 2.39) are solved by mapping the whole system on a discrete three-dimensional Cartesian mesh. In particular, the simulation domain consists of a box with the center located in the origin of the Cartesian system: it is uniquely specified by the values x_{max}, y_{max}, z_{max} and by the number of points n_x, n_y, n_z along the three directions (the total number of points of the grid is, clearly, $n_x \cdot n_y \cdot n_z$). The spatial steps are obtained from:

$$\Delta x = \frac{2\,x_{max}}{n_x} \qquad \Delta y = \frac{2\,y_{max}}{n_y} \qquad \Delta z = \frac{2\,z_{max}}{n_z}$$

The discretization of differential operators requires to fix the boundary conditions: in all the computations periodic boundary conditions (PBC) are employed. Calling i, j, k the spatial indices labelling the points of the mesh, the correct implementation of PBC has as a result the exclusion of the extrema x_{max}, y_{max}, z_{max} :

$$\begin{array}{lll} x(i) = -x_{max} + (i-1)\,\Delta x & y(j) = -y_{max} + (j-1)\,\Delta y & z(k) = -z_{max} + (k-1)\,\Delta z \\ i \in [1, n_x] & j \in [1, n_y] & k \in [1, n_z] \end{array}$$

The two different sets of GP equations are solved with two different methods: for the stationary GP equation (2.37) one uses an imaginary time evolution, while the time dependent equation (2.39) requires a dynamics in real time. The development of the details of these two methods is the subject of the next sections.

B.2 Ground state energy

The ground state of the system is obtained through a steepest descent algorithm that, starting from an initial configuration, moves towards the minimum of the total energy: formally, this corresponds to solve stationary GP equations.
Let's consider a GP equation for a single order parameter of the form:

$$i\hbar \frac{\partial}{\partial t}\psi(\vec{r}, t) = H\,\psi(\vec{r}, t) \tag{B.1}$$

where the Hamiltonian, obtained from a minimization of the total energy, contains the non-linear interaction potential $V(\rho = |\psi|^2)$ with both the MF and LHY terms

$$H = \frac{\delta E}{\delta \rho} = -\frac{\hbar^2}{2m}\vec{\nabla}^2 + V(\rho) \tag{B.2}$$

The corresponding eigenvalue problem for the Hamiltonian is

$$H\,\varphi(\vec{r}) \;=\; \mu\,\varphi(\vec{r}) \tag{B.3}$$

where the lowest energy state can be labeled by $\{\varphi_0(\vec{r}),\, \mu_0\}$. We are allowed to perform a simple shift in the chemical potential, rewriting:

$$H\,\varphi(\vec{r}) \;=\; \mu\,\varphi(\vec{r}) \qquad \longmapsto \qquad (H \,-\, \mu_0)\,\varphi(\vec{r}) \;=\; \mu\,\varphi(\vec{r}) \tag{B.4}$$

The time-dependent wave function is obtained applying the time-evolution operator to a state at any arbitrary initial time:

$$\psi(\vec{r},t) \;=\; e^{-\frac{i}{\hbar}\,(H-\mu_0)\,t}\,\psi(\vec{r},0) \tag{B.5}$$

This starting wave function can always be written as a linear combination of eigenfunctions $\varphi(\vec{r})$ of the Hamiltonian:

$$\psi(\vec{r},0) \;=\; c_0\,\varphi_0(\vec{r}) \,+\, \sum_{i=1}^{\infty} c_i\,\varphi_i(\vec{r}) \quad \Rightarrow \quad \psi(\vec{r},t) \;=\; e^{-\frac{i}{\hbar}\,(H-\mu_0)\,t}\,\left[\,c_0\,\varphi_0(\vec{r}) \,+\, c_1\,\varphi_1(\vec{r}) \,+\, c_2\,\varphi_2(\vec{r}) \,+\, ...\,\right] \tag{B.6}$$

At this point it is convenient to switch to the imaginary time formalism, that is defined performing a Wick rotation of the real time

$$t \qquad \longmapsto \qquad \tau \;=\; i\,t \tag{B.7}$$

so that the expansion of the wave function becomes:

$$\begin{aligned}\psi(\vec{r},\tau) \;&=\; e^{-\,\frac{H-\mu_0}{\hbar}\,\tau}\,\left[\,c_0\,\varphi_0(\vec{r}) \,+\, c_1\,\varphi_1(\vec{r}) \,+\, c_2\,\varphi_2(\vec{r}) \,+\, ...\,\right] = \\ &= e^{-\,\frac{\mu_0-\mu_0}{\hbar}\,\tau}\,c_0\,\varphi_0(\vec{r}) \,+\, e^{-\,\frac{\mu_1-\mu_0}{\hbar}\,\tau}\,c_1\,\varphi_1(\vec{r}) \,+\, e^{-\,\frac{\mu_2-\mu_0}{\hbar}\,\tau}\,c_2\,\varphi_2(\vec{r}) \,+\, ... = \\ &= c_0\,\varphi_0(\vec{r}) \,+\, e^{-\,\alpha_1\,\frac{\tau}{\hbar}}\,c_1\,\varphi_1(\vec{r}) \,+\, e^{-\,\alpha_2\,\frac{\tau}{\hbar}}\,c_2\,\varphi_2(\vec{r}) \,+\, ...\end{aligned} \tag{B.8}$$

The imaginary exponentials are now replaced by real ones and, being μ_0 the eigenenergy associated to the ground state eigenfunction, all the excited states are subjected to an exponential suppression:

$$\alpha_i \;\equiv\; \mu_i \,-\, \mu_0 \;>\; 0 \qquad \forall\, i \geq 1 \qquad \Rightarrow \qquad \lim_{\tau\to\infty} \psi(\vec{r},\tau) \;=\; c_0\,\varphi_0(\vec{r}) \tag{B.9}$$

The idea is to start from an initial trial wave function and propagate it in imaginary time up to the formal limit "$\tau \to \infty$": at the end of this procedure all the excited states are filtered out and the initial state relaxes towards the exact ground state eigenfunction (apart from a constant prefactor).

Let's pause for a moment on the choice of the starting trial wave function (i.e., the initial density): in fact, the better the starting assumption, the faster the code will converge to the ground state solution. For systems of quantum droplets there are two possible choices for the starting ansatz:

- the density profile can be described by a sigmoid function. A first good choice can be a Fermi distribution function (also known as logistic function) like:

$$\rho(r) \;=\; \frac{\rho_0}{1+\exp\left(\frac{r-r_0}{d}\right)} \tag{B.10}$$

  ρ_0 stands for the equilibrium bulk density (i.e. the density of the uniform system) and it is fixed from the properties of the mixture. The two parameters are the distance r_0, where the density reaches the value $\rho_0/2$, and d, that is related to the surface width. In particular, if one defines as Δ the width over which the density decreases from 90% to 10% of the bulk density: the parameter d corresponds to:

$$\Delta \;=\; r\big|_{\rho=0.9\rho_0} \,-\, r\big|_{\rho=0.1\rho_0} \;=\; 2\,\ln(9)\,d \;\simeq\; 4.4\,d \tag{B.11}$$

The "midpoint" r_0 can be taken equal to the radius R of the droplet that can be in turn obtained from the total number of particles $N = N_1 + N_2$ making up the Bose mixture:

$$R \simeq \left(\frac{3N}{4\pi\rho_0}\right)^{1/3} \tag{B.12}$$

The width Δ has to be chosen as a good compromise between two extrema: if it is too large the droplet would be too broadened, but if it is too small then one is left with a step function that could have problems with numerical differentiation. For low values of Δ, the density profile can be parametrized by another sigmoid function, this time related to the hyperbolic tangent:

$$\rho(r) = \frac{\rho_0}{2}\left[1 - \tanh\left(\frac{r - r_0}{\Delta}\right)\right] \tag{B.13}$$

In this case, the relationship between d and Δ reads:

$$\Delta = r\big|_{\rho=0.9\rho_0} - r\big|_{\rho=0.1\rho_0} = 2\tanh^{-1}\left(\frac{4}{5}\right) d \simeq 2.2\, d \tag{B.14}$$

Both Eqs. (B.10, B.13) represent a density profile, schematically drawn in Figure B.1 (a), that is almost constant inside the bulk and rapidly goes to zero through the liquid-vacuum interface. Such a profile is peculiar of droplets with a number of particles higher than the critical number N_c (below which evaporation breaks the self-bound regime) where the surface effects are risible compared to its bulk properties:

$$N \gg N_c \qquad\qquad \frac{\Delta}{R} \ll 1 \tag{B.15}$$

- one can assume a gaussian density profile, such as

$$\rho(r) = \mathcal{N} e^{-\frac{r^2}{2\Delta^2}} \tag{B.16}$$

$\mathcal{N}$ is a normalization constant fixed by the condition on the total number of particles N:

$$\int d\vec{r}\,\rho(r) = N$$

Δ is the standard deviation that gives an idea of the width of the gaussian function and it can be estimated as the radius of the droplet. This situation, represented in Figure B.1 (b), is the opposite with respect to the previous one, in fact surface properties are dominant over bulk ones. Such profile is typical of systems, denoted as "all-surface" droplets, with a total number of particles that is comparable with the critical one:

$$N \simeq N_c \qquad\qquad \frac{\Delta}{R} \simeq 1 \tag{B.17}$$

We mention here that the numerical codes can be adapted, by suitable adjustments, to systems characterized by a planar geometry where the density varies along the z direction while it is uniform over the x-y plane. This type of configuration is often used in surface tension calculations and it implies a planar interface that separates the liquid phase in the bulk of the droplet from the outside region, defined as "vacuum". Slab geometry simulations require less computational cost since the 3D mesh reduces to a 1D grid along the z direction, however one has to introduce vacuum regions that are wide enough to avoid every possible interaction between a given density and its periodically repeated images: Figure B.2 shows a schematic picture of this simulation domain.

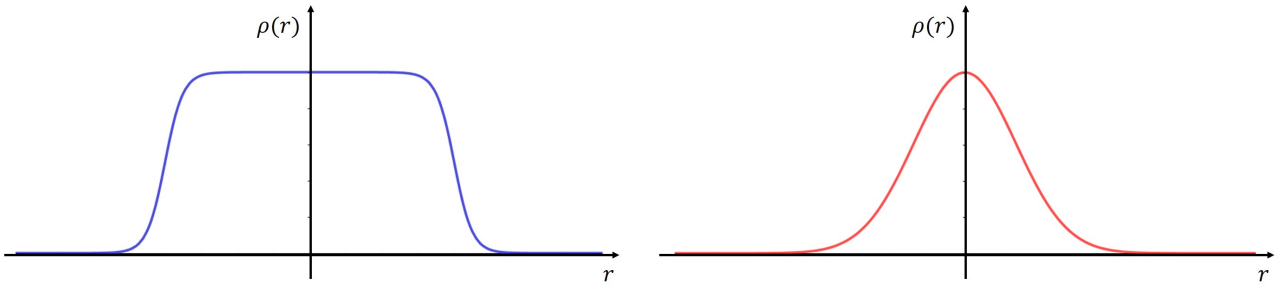

(a) Sigmoid ansatz.

(b) Gaussian ansatz.

Figure B.1: Different guesses for the starting trial density: one where bulk properties prevail (left), the other one for an "all-surface" droplet (right). The radial coordinate, which actually takes non-negative values, is here extended to a real variable in order to provide a clearer idea of the shape of the droplets in the 3D space.

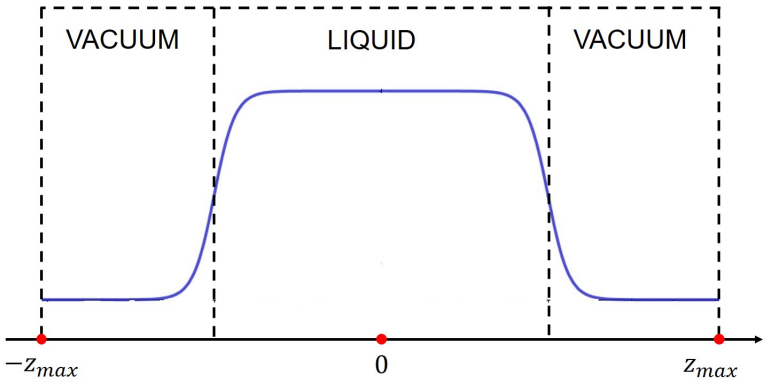

Figure B.2: Schematic representation of the simulation domain for a slab geometry computation. Notice that the 3D mesh reduces to a 1D grid (the z direction is chosen in this figure).

After the determination of the initial state, the relaxation towards the ground state is performed in practice by solving the time-dependent GP equation in imaginary time. This procedure is now generalized to a binary Bose mixture, like the ^{41}K-^{87}Rb one that we studied in this thesis project. The uniform system is described by the energy functional $\mathcal{E}(\rho_1, \rho_2)$ given by Eq. (2.24) and the two order parameters ψ_1, ψ_2 obey the following GP equations in imaginary time:

$$\begin{cases} -\hbar \frac{\partial}{\partial \tau} \psi_1(\vec{r}, \tau) &= (H_1 - \mu_1)\, \psi_1(\vec{r}, \tau) \qquad \text{with} \quad H_1 = \frac{\delta E}{\delta \rho_1} = -\frac{\hbar^2}{2m_1}\vec{\nabla}^2 + \frac{\partial \mathcal{E}}{\partial \rho_1} + U \\ -\hbar \frac{\partial}{\partial \tau} \psi_2(\vec{r}, \tau) &= (H_2 - \mu_2)\, \psi_2(\vec{r}, \tau) \qquad \text{with} \quad H_2 = \frac{\delta E}{\delta \rho_2} = -\frac{\hbar^2}{2m_2}\vec{\nabla}^2 + \frac{\partial \mathcal{E}}{\partial \rho_2} + U \end{cases} \tag{B.18}$$

where the energy shift with respect to the chemical potentials has already been performed and we assume the presence of an external potential U acting on both the species. Notice that the two order parameters are independent one from the other (they are not forced to obey the *MF optimal ratio*) and they are normalized to the number of atoms of theri respective species.
Let's restrict for the moment to a one-dimensional system, so that the 3D mesh reduces to a 1D grid along the x direction. The solution of Eq. (B.18) implies a discretization also in time, therefore we introduce a time-step $\Delta\tau$ and an index n that labels the discrete instants of time: n runs from 1 to a maximum value $\mathrm{n_{max}}$ that is determined by trial and error looking at the convergence towards the ground state. By denoting with j the label for the points in the x-direction, the wave function at each instant of time (i.e., for a fixed n) becomes a vector with $\mathrm{n_x}$ components:

$$\psi_i(\mathrm{x}, \tau) \qquad \longmapsto \qquad \psi_i(\mathrm{j}, \mathrm{n}) = (\psi_i(1, \mathrm{n}), \ldots, \psi_i(\mathrm{n_x}, \mathrm{n})) \qquad i = 1, 2$$

In general the time-step Δt is related to the spatial step Δx through a relation that can be qualitatively derived from the Heisenberg uncertainty principle:

$$\Delta E\, \Delta t \geq \frac{\hbar}{2} \tag{B.19}$$

The energy fluctuation can be estimated as a kinetic contribution where the modulus of the wave vector $\vec{k}$ is related to the inverse of the spatial step:

$$\Delta E \simeq \frac{\hbar^2 k^2}{2m} \simeq \frac{\hbar^2}{2m} \frac{1}{\Delta x^2} \tag{B.20}$$

Finally, substituting in Eq. (B.19):

$$\Delta t \gtrsim \frac{m}{\hbar} \Delta x^2 \qquad \Rightarrow \qquad \Delta t \simeq \mathcal{T} \frac{m_2}{\hbar} \Delta x^2 \tag{B.21}$$

where, in the last step, the mass of the heavier species was considered (in order to have an upper bound) and the constant prefactor $\mathcal{T}$ was introduced, with typical values $\mathcal{T} \in [0.01, 0.1]$.
This same rule of thumb can be applied also to evolutions in imaginary time.

At this point we can summarize the whole procedure that lays at the basis of a steepest descent algorithm using a relaxation in imaginary time.

1. Start from initial trial wave functions $\psi_1^{(0)}(x)$, $\psi_2^{(0)}(x)$ for both species following, for instance, the examples that were explained in detail before. It is convenient to choose two initial density profiles and the number of particles that satisfy the MF optimal ratio:

$$\frac{\rho_2^{(0)}}{\rho_1^{(0)}} = \frac{|\psi_2^{(0)}|^2}{|\psi_1^{(0)}|^2} = \frac{N_2}{N_1} = \sqrt{\frac{g_{11}}{g_{22}}}$$

   From these guesses one has to compute the initial values of the chemical potentials that, in the Dirac formalism, are:

$$\mu_i^{(0)} = \frac{\left\langle \psi_i^{(0)} \right| H_i^{(0)} \left| \psi_i^{(0)} \right\rangle}{\left\langle \psi_i^{(0)} \middle| \psi_i^{(0)} \right\rangle} \qquad i = 1, 2, \ldots$$

   Integrals can be numerically computed by means of the trapezoidal rule, the advantage of PBC is that it is no more necessary to give a half weight to the starting and the final points, that is:

$$\int dx\, \rho(x) = \sum_{j=1}^{n_x} \rho(j)\, \Delta x \qquad \text{with} \quad \rho(j) \equiv \rho(x(j))$$

   Also the effective potentials $\frac{\partial \mathcal{E}}{\partial \rho_i}$ appearing in Eq. (B.18) have to be explicitly computed using the starting densities.

2. Solve the system of coupled equations (B.18) after a proper discretization. In order to speed up the convergence, four auxiliary wave functions (two for each species) $\varphi_i^{(1)}$, $\varphi_i^{(2)}$ are introduced: they enter the time evolution as a sort of "velocity term" and they are initialized as

$$\varphi_i^{(1)} = \psi_i^{(0)} \qquad \varphi_i^{(2)} = \psi_i^{(0)}$$

   At each time step n, the update rule for the wave functions is the following (let's drop the spatial index for simplicity):

$$\begin{aligned} \psi_i(n+1) &= \psi_i(n) - \frac{\Delta\tau}{\hbar} \left[H_i(n) - \mu_i(n) \right] \psi_i(n) + \\ &\quad + \Delta_1 \left[\psi_i(n) - \varphi_i^{(1)}(n) \right] + \Delta_2 \left[\varphi_i^{(1)}(n) - \varphi_i^{(2)}(n) \right] \\ \varphi_i^{(2)}(n+1) &= \varphi_i^{(1)}(n) \\ \varphi_i^{(1)}(n+1) &= \psi_i(n) \end{aligned} \tag{B.22}$$

The two parameters appearing in the auxiliary terms are approximately:

$$\Delta_1 \simeq 0.7 \qquad\qquad \Delta_2 \simeq 0.2 \tag{B.23}$$

The new wave functions must be properly normalized and then used to compute the new effective potentials and to update the chemical potentials to be inserted in the next iteration:

$$\langle\psi_i(\mathrm{n}+1)|\psi_i(\mathrm{n}+1)\rangle \stackrel{!}{=} N_i \qquad\qquad \mu_i(\mathrm{n}+1) = \frac{\langle\psi_i(\mathrm{n}+1)|\ H_i(\mathrm{n}+1)\ |\psi_i(\mathrm{n}+1)\rangle}{\langle\psi_i(\mathrm{n}+1)|\psi_i(\mathrm{n}+1)\rangle}$$

3. Compute the total energy of the system at the time-step n+1, that is given by performing the integral in Eq. (2.9) over the whole simulation box (in the 3D case) of the energy functional of Eq. (2.10) with the densities $\rho_1(\mathrm{n}+1)$, $\rho_2(\mathrm{n}+1)$.

4. Compare the total energy at step n+1 with the one at the previous step with a reasonably small convergence threshold ε:

   - $|E(\mathrm{n}+1) - E(\mathrm{n})| > \varepsilon$: go back to point 2. and continue the relaxation process;
   - $|E(\mathrm{n}+1) - E(\mathrm{n})| < \varepsilon$: the numerical code has converged towards the lowest energy state and the output yields the density profiles and the ground state energy.

B.3 Real time dynamics

The dynamics in real time is based on a more accurate algorithm than the simple Euler method that is employed in the update rule of Eq. (B.22). In particular, the numerical method used to solve the GP equations is the Hamming's **predictor-modifier-corrector** method for the solution of ordinary differential equations [59].
Let's consider a given differential equation

$$\frac{dy}{dx} = f(x, y) \tag{B.24}$$

that is discretized using the following symbols:

$$y_i = y(x_i) \qquad\qquad y'_i = \left.\frac{dy}{dx}\right|_{x=x_i} \qquad\qquad i = 0,\ 1,\ \ldots \tag{B.25}$$

where x_i is the value of x at the i^{th} step in the integration and $x_{i+1} - x_i = h$ (h is usually a constant, but it can be changed run-time if necessary). In general, when high accuracy is required in a solution of ordinary differential equations, an iterative formula is used because it has much smaller error terms than their analogous forward integration formulas. A possible iterative technique is represented by predictor-corrector algorithms that perform the following steps:

1. predict the value of y at $x = x_{n+1}$ and call it $\bar{y}_{n+1}$ (prediction);
2. calculate $\bar{y}'_{n+1} = f(x_{n+1}, \bar{y}_{n+1})$ using the differential equation (B.24);
3. calculate again a new y_{n+1} by means of an iterative formula (correction);
4. repeat steps 2. and 3. until the difference between successive values of y_{n+1} is within some predetermined limit.

Iterative methods require successive recalculations of $f(x, y)$ at each step until the process converges: this can be a serious disadvantage, since a large number of equations implies a large total machine time. A possible way to avoid iterations is to accept as y_{n+1} the first value of the corrector and this is implemented inside a more sophisticated method: the predictor-modifier-corrector algorithm. In the version developed by Hamming, it consists of the following steps:

- the value of y_{n+1} is predicted with

$$p_{n+1} = y_{n-3} + \frac{4h}{3}\left(2y'_n - y'_{n-1} + 2y'_{n-2}\right) \tag{B.26}$$

- the predictor is modified by

$$\begin{aligned} m_{n+1} &= p_{n+1} - \frac{112}{121}\left(p_n - c_n\right) \\ m'_{n+1} &= f(x_{n+1}, m_{n+1}) \end{aligned} \tag{B.27}$$

- the corrector is computed as

$$c_{n+1} = \frac{1}{8}\left[9y_n - y_{n-2} + 3h\left(m'_{n+1} + 2y'_n - y'_{n-1}\right)\right] \tag{B.28}$$

- the final value of y_{n+1} is

$$y_{n+1} = c_{n+1} + \frac{9}{121}\left(p_{n+1} - c_{n+1}\right) \tag{B.29}$$

This method has the great advantages of being stable and to reduce the computational cost: in fact, due to the absence of iterations, only two values of $f(x, y)$ must be computed at each step.
It is clear that the above formulas defining Hamming's method are not self-starting, meaning that each step of the integration requires the knowledge of past values of the solution which are not available at the start of the integration itself. It is important that the starting values of y_n are provided with an accuracy that is at least as high as the one of the numerical integration procedure. The specific Hamming's method used here is initiated by a **fourth order Runge-Kutta-Gill algorithm** that requires only the initial condition $y_0 = y(x_0)$ to provide the starting functions:

$$\begin{aligned} k_1 &= h\,f(x_0, y_0) & y_1 &= y_0 + \frac{1}{2}\left(k_1 - 2q_0\right) \\ k_2 &= h\,f(x_0 + \frac{h}{2}, y_1) & y_2 &= y_1 + \left(1 - \frac{1}{\sqrt{2}}\right)\left(k_2 - q_1\right) \\ k_3 &= h\,f(x_0 + \frac{h}{2}, y_2) & y_3 &= y_2 + \left(1 + \frac{1}{\sqrt{2}}\right)\left(k_3 - q_2\right) \\ k_4 &= h\,f(x_0 + h, y_3) & y_4 &= y_3 + \frac{1}{6}\left(k_4 - 2q_3\right) \end{aligned} \tag{B.30}$$

where the coefficients q are given by

$$\begin{aligned} q_1 &= q_0 + 3\left[\frac{1}{2}(k_1 - 2q_0)\right] - \frac{1}{2}k_1 \\ q_2 &= q_1 + 3\left[\left(1 - \frac{1}{\sqrt{2}}\right)\left(k_2 - q_1\right)\right] - \left(1 - \frac{1}{\sqrt{2}}\right)k_2 \\ q_3 &= q_2 + 3\left[\left(1 + \frac{1}{\sqrt{2}}\right)\left(k_3 - q_2\right)\right] - \left(1 + \frac{1}{\sqrt{2}}\right)k_3 \\ q_4 &= q_3 + 3\left[\frac{1}{6}(k_4 - 2q_3)\right] - \frac{1}{2}k_4 \end{aligned} \tag{B.31}$$

with q_0 that is initially zero and q_3 that is used as q_4 for the next step.

Appendix C

Density profile of a quantum droplet

From the variational principle, the density describing the ground state of the systems is the one that minimizes the total energy

$$\frac{\delta E}{\delta \rho_1} = 0 \qquad \text{with} \qquad \int d\vec{r}\, \rho_1 = N_1 \qquad \left(\text{and} \quad N_2 = N_1 \sqrt{\frac{g_{11}}{g_{22}}}\right) \tag{C.1}$$

where we have assumed the densities to satisfy the MF optimal ratio and N_i ($i = 1, 2$) are the total number of particles of the i-th species.
Since it is a minimization problem subject to a constraint, the chemical potential μ is introduced as a Lagrange multiplier and the problem reads

$$\frac{\delta}{\delta \rho_1}\left[E - \mu N_1\right] = 0 \qquad \Longrightarrow \qquad \frac{\delta E}{\delta \rho_1} - \mu = 0 \tag{C.2}$$

which admits as a solution the well known Euler-Lagrange equations:

$$\frac{\partial \mathcal{E}}{\partial \rho_1} - \vec{\nabla} \cdot \left(\frac{\partial \mathcal{E}}{\partial (\vec{\nabla}\rho_1)}\right) - \mu = 0 \tag{C.3}$$

The minimization procedure applied to the functional given by Eq. (2.22) yields:

$$\alpha \left(\frac{\vec{\nabla}\rho_1}{\rho_1}\right)^2 - 2\alpha \frac{\vec{\nabla}^2 \rho_1}{\rho_1} + 2\beta\rho_1 + \frac{5}{2}\gamma\rho_1^{3/2} - \mu = 0 \tag{C.4}$$

It is convenient to reduce to the one-dimensional case that is appropriate for surface tension calculations, as the ones carried out in Chapter 3. Assuming that the density profiles vary only along the z direction ($\rho_1' = {}^{d\rho_1}/_{dz}$, $\rho_1'' = {}^{d^2\rho_1}/_{dz^2}$), the 1D version of the E.L. equations is:

$$\alpha \left(\frac{\rho_1'^2}{\rho_1^2} - 2\frac{\rho_1''}{\rho_1}\right) + 2\beta\,\rho_1 + \frac{5}{2}\gamma\,\rho_1^{3/2} - \mu = 0 \tag{C.5}$$

Multiplying both sides of Eq. (C.5) by ρ_1' and noticing that

$$-\frac{d}{dz}\left(\frac{\rho_1'^2}{\rho_1}\right) = \left(\frac{\rho_1'^2}{\rho_1^2} - 2\frac{\rho_1''}{\rho_1}\right)\rho_1'$$

one obtains:

$$\begin{aligned} &\frac{d}{dz}\left[-\alpha\,\frac{\rho_1'^2}{\rho_1} + \beta\,\rho_1^2 + \gamma\,\rho_1^{5/2} - \mu\,\rho_1\right] = 0 \\ \Longrightarrow\; &-\alpha\,\frac{\rho_1'^2}{\rho_1} + \beta\,\rho_1^2 + \gamma\,\rho_1^{5/2} - \mu\,\rho_1 = \mathcal{C} \end{aligned} \tag{C.6}$$

$\mathcal{C}$ is a constant whose value is set by analyzing the particular geometry of the system. Focusing on the droplet, it is possible to distinguish two different regions, that are separated by its surface: the inner part, known as the "bulk", and the outer one, that is the "vacuum". Far from the interface, in the vacuum side, the density is expected to vanish, together with its derivatives, implying that:

$$\mathcal{C} = 0 \tag{C.7}$$

On the opposite side, inside the bulk region, the droplet is expected to form a uniform system, so that the value of the density is constant to the bulk density $\rho_1^{(0)}$. This assumption, valid for a liquid system in equilibrium with the vacuum, allows to fix the value of the chemical potential:

$$\rho_1{}^{(0)\prime} = 0 \qquad \Rightarrow \qquad \rho_1{}^{(0)} \left(\beta \rho_1{}^{(0)} + \gamma \rho_1{}^{(0)3/2} - \mu \right) = 0 \qquad \Rightarrow \qquad \mu = \mu_0 = \beta \rho_1{}^{(0)} + \gamma \rho_1{}^{(0)3/2} \tag{C.8}$$

Putting everything together, the interface of the quantum droplet is thus governed by the following differential equation:

$$-\alpha \frac{\rho_1'^2}{\rho_1} + \beta \rho_1^2 + \gamma \rho_1^{5/2} - \mu_0 \rho_1 = 0 \tag{C.9}$$

It can be made explicit:

$$\begin{aligned} \rho_1'^2 &= \frac{\rho_1}{\alpha} \left(\beta \rho_1^2 + \gamma \rho_1^{5/2} - \mu_0 \rho_1 \right) \\ \Rightarrow \frac{d\rho_1}{dz} &= -\sqrt{\frac{\rho_1}{\alpha}} \left(\beta \rho_1^2 + \gamma \rho_1^{5/2} - \mu_0 \rho_1 \right)^{1/2} \equiv h(\rho_1) \end{aligned} \tag{C.10}$$

where the minus sign comes out from the fact that the derivative at the interface is negative.
Eq. (C.10) can be inverted to obtain:

$$dz = \frac{d\rho_1}{h(\rho_1)} \qquad \Rightarrow \qquad z = z_0 + \int_{\rho_1^{(0)}/2}^{\rho_1} \frac{d\rho}{h(\rho)} \tag{C.11}$$

where z_0 is the position where the value of the density is exactly one half of the equilibrium one. From the solution of Eq. (C.11), $z(\rho_1)$, one can reconstruct the whole profile of the interface.

Bibliography

[1] A. N. Bohr and B. R. Mottelson. *Nuclear Structure (Vol. 1)*. World Scientific Publishing Company, 1998.

[2] R. J. Donnelly. *Quantized vortices in helium II*. Vol. 2. Cambridge University Press, 1991.

[3] J. P. Toennies and A. F. Vilesov. "Superfluid Helium Droplets: A Uniquely Cold Nanomatrix for Molecules and Molecular Complexes". In: *Angewandte Chemie International Edition* 43.20 (2004), pp. 2622–2648. DOI: https://doi.org/10.1002/anie.200300611. eprint: https://onlinelibrary.wiley.com/doi/pdf/10.1002/anie.200300611. URL: https://onlinelibrary.wiley.com/doi/abs/10.1002/anie.200300611.

[4] F. Ancilotto, M. Barranco, and M. Pi. "Spinning superfluid ^{4}He nanodroplets". In: *Physical Review B* 97.18 (May 2018). ISSN: 2469-9969. DOI: 10.1103/physrevb.97.184515. URL: http://dx.doi.org/10.1103/PhysRevB.97.184515.

[5] D. S. Petrov. "Quantum Mechanical Stabilization of a Collapsing Bose-Bose Mixture". In: *Phys. Rev. Lett.* 115 (15 Oct. 2015), p. 155302. DOI: 10.1103/PhysRevLett.115.155302. URL: https://link.aps.org/doi/10.1103/PhysRevLett.115.155302.

[6] C. R. Cabrera et al. "Quantum liquid droplets in a mixture of Bose-Einstein condensates". In: *Science* 359.6373 (Dec. 2017), pp. 301–304. ISSN: 1095-9203. DOI: 10.1126/science.aao5686. URL: http://dx.doi.org/10.1126/science.aao5686.

[7] G. Semeghini et al. "Self-Bound Quantum Droplets of Atomic Mixtures in Free Space". In: *Physical Review Letters* 120.23 (June 2018). ISSN: 1079-7114. DOI: 10.1103/physrevlett.120.235301. URL: http://dx.doi.org/10.1103/PhysRevLett.120.235301.

[8] C. D'Errico et al. "Observation of quantum droplets in a heteronuclear bosonic mixture". In: *Phys. Rev. Research* 1 (3 Dec. 2019), p. 033155. DOI: 10.1103/PhysRevResearch.1.033155. URL: https://link.aps.org/doi/10.1103/PhysRevResearch.1.033155.

[9] T. D. Lee, K. Huang, and C. N. Yang. "Eigenvalues and Eigenfunctions of a Bose System of Hard Spheres and Its Low-Temperature Properties". In: *Phys. Rev.* 106 (6 June 1957), pp. 1135–1145. DOI: 10.1103/PhysRev.106.1135. URL: https://link.aps.org/doi/10.1103/PhysRev.106.1135.

[10] R. A. Brown and L. E. Scriven. "The shape and stability of rotating liquid drops". In: *Proceedings of the Royal Society of London. A. Mathematical and Physical Sciences* 371.1746 (1980), pp. 331–357.

[11] L. F. Gomez et al. "Shapes and vorticities of superfluid helium nanodroplets". In: *Science* 345.6199 (2014), pp. 906–909. ISSN: 0036-8075. DOI: 10.1126/science.1252395. eprint: https://science.sciencemag.org/content/345/6199/906.pdf. URL: https://science.sciencemag.org/content/345/6199/906.

[12] D. Rupp et al. "Coherent diffractive imaging of single helium nanodroplets with a high harmonic generation source". In: *Nature Communications* 8.1 (Sept. 2017). ISSN: 2041-1723. DOI: 10.1038/s41467-017-00287-z. URL: http://dx.doi.org/10.1038/s41467-017-00287-z.

[13] B. Langbehn et al. "Three-Dimensional Shapes of Spinning Helium Nanodroplets". In: *Phys. Rev. Lett.* 121 (25 Dec. 2018), p. 255301. DOI: 10.1103/PhysRevLett.121.255301. URL: https://link.aps.org/doi/10.1103/PhysRevLett.121.255301.

[14] F. Ancilotto, M. Pi, and M. Barranco. "Vortex arrays in nanoscopic superfluid helium droplets". In: *Phys. Rev. B* 91 (10 Mar. 2015), p. 100503. DOI: 10.1103/PhysRevB.91.100503. URL: https://link.aps.org/doi/10.1103/PhysRevB.91.100503.

[15] S. M. O. O'Connell et al. "Angular Momentum in Rotating Superfluid Droplets". In: *Physical Review Letters* 124.21 (May 2020). ISSN: 1079-7114. DOI: 10.1103/physrevlett.124.215301. URL: http://dx.doi.org/10.1103/PhysRevLett.124.215301.

[16] L. Pitaevskii and S. Stringari. *Bose-Einstein condensation and superfluidity*. Vol. 164. Oxford University Press, 2016.

[17] A. Altland and B. D. Simons. *Condensed matter field theory*. Cambridge University Press, 2010.

[18] S. N. Bose. "Planck's law and the light quantum hypothesis". In: *Journal of Astrophysics and Astronomy* 15 (1994), p. 3.

[19] K. Huang. *Statistical Mechanics*. 2nd ed. John Wiley & Sons, 1987.

[20] M. H. Anderson et al. "Observation of Bose-Einstein Condensation in a Dilute Atomic Vapor". In: *Science* 269.5221 (1995), pp. 198–201. ISSN: 0036-8075. DOI: 10.1126/science.269.5221.198. eprint: https://science.sciencemag.org/content/269/5221/198.full.pdf. URL: https://science.sciencemag.org/content/269/5221/198.

[21] K. B. Davis et al. "Bose-Einstein Condensation in a Gas of Sodium Atoms". In: *Phys. Rev. Lett.* 75 (22 Nov. 1995), pp. 3969–3973. DOI: 10.1103/PhysRevLett.75.3969. URL: https://link.aps.org/doi/10.1103/PhysRevLett.75.3969.

[22] L. D. Landau and E. M. Lifshitz. *Quantum mechanics: non-relativistic theory*. Vol. 3. Elsevier, 2013.

[23] J. R. Taylor. *Scattering theory: the quantum theory of nonrelativistic collisions*. Courier Corporation, 2006.

[24] R. G. Newton. *Scattering theory of waves and particles*. Springer Science & Business Media, 2013.

[25] J. W. Negele and H. Orland. *Quantum many-particle systems (Advanced Book classics)*. Westview Press, 1998.

[26] N. Nagaosa. *Quantum field theory in condensed matter physics*. Springer Science & Business Media, 1999.

[27] N. Bogoliubov. "On the theory of superfluidity". In: *J. Phys* 11.1 (1947), p. 23.

[28] L. Landau. "Theory of the Superfluidity of Helium II". In: *Phys. Rev.* 60 (4 Aug. 1941), pp. 356–358. DOI: 10.1103/PhysRev.60.356. URL: https://link.aps.org/doi/10.1103/PhysRev.60.356.

[29] H. E. Hall and W. F. Vinen. "The rotation of liquid helium II *II*. The theory of mutual friction in uniformly rotating helium II". In: *Proceedings of the Royal Society of London. Series A. Mathematical and Physical Sciences* 238.1213 (1956), pp. 215–234.

[30] O. V. Lounasmaa and E. Thuneberg. "Vortices in rotating superfluid ^{3}He". In: *Proceedings of the National Academy of Sciences* 96.14 (1999), pp. 7760–7767. ISSN: 0027-8424. DOI: 10.1073/pnas.96.14.7760. eprint: https://www.pnas.org/content/96/14/7760.full.pdf. URL: https://www.pnas.org/content/96/14/7760.

[31] A. A. Abrikosov. "The magnetic properties of superconducting alloys". In: *Journal of Physics and Chemistry of Solids* 2.3 (1957), pp. 199–208. ISSN: 0022-3697. DOI: https://doi.org/10.1016/0022-3697(57)90083-5. URL: https://www.sciencedirect.com/science/article/pii/0022369757900835.

[32] R. P. Feynman. "Application of Quantum Mechanics to Liquid Helium". In: *Progress in Low Temperature Physics* 1 (1955). Ed. by C.J. Gorter, pp. 17–53. ISSN: 0079-6417. DOI: https://doi.org/10.1016/S0079-6417(08)60077-3. URL: https://www.sciencedirect.com/science/article/pii/S0079641708600773.

[33] A. L. Fetter. "Vortex nucleation in deformed rotating cylinders". In: *Journal of Low Temperature Physics* 16.5 (1974), pp. 533–555.

[34] I. Ferrier-Barbut. "Ultradilute quantum droplets". In: *Physics Today* 72.4 (2019), pp. 46–52.

[35] H. Kadau et al. "Observing the Rosensweig instability of a quantum ferrofluid". In: *Nature* 530.7589 (2016), pp. 194–197.

[36] L. Chomaz et al. "Quantum-Fluctuation-Driven Crossover from a Dilute Bose-Einstein Condensate to a Macrodroplet in a Dipolar Quantum Fluid". In: *Phys. Rev. X* 6 (4 Nov. 2016), p. 041039. DOI: 10.1103/PhysRevX.6.041039. URL: https://link.aps.org/doi/10.1103/PhysRevX.6.041039.

[37] A. Burchianti et al. "A Dual-Species Bose-Einstein Condensate with Attractive Interspecies Interactions". In: *Condensed Matter* 5.1 (2020). ISSN: 2410-3896. DOI: 10.3390/condmat5010021. URL: https://www.mdpi.com/2410-3896/5/1/21.

[38] D. M. Larsen. "Binary mixtures of dilute bose gases with repulsive interactions at low temperature". In: *Annals of Physics (New York)(US)* 24 (1963).

[39] F. Ancilotto et al. "Self-bound ultradilute Bose mixtures within local density approximation". In: *Phys. Rev. A* 98 (5 Nov. 2018), p. 053623. DOI: 10.1103/PhysRevA.98.053623. URL: https://link.aps.org/doi/10.1103/PhysRevA.98.053623.

[40] C. Fort and M. Modugno. "Self-Evaporation Dynamics of Quantum Droplets in a ^{41}K-^{87}Rb Mixture". In: *Applied Sciences* 11.2 (2021). ISSN: 2076-3417. DOI: 10.3390/app11020866. URL: https://www.mdpi.com/2076-3417/11/2/866.

[41] R. C. Tolman. "The Effect of Droplet Size on Surface Tension". In: *The Journal of Chemical Physics* 17.3 (1949), pp. 333–337. DOI: 10.1063/1.1747247. eprint: https://doi.org/10.1063/1.1747247. URL: https://doi.org/10.1063/1.1747247.

[42] Y. A. Lei et al. "The Tolman Length: Is It Positive or Negative?" In: *Journal of the American Chemical Society* 127.44 (2005). PMID: 16262379, pp. 15346–15347. DOI: 10.1021/ja054297i. eprint: https://doi.org/10.1021/ja054297i. URL: https://doi.org/10.1021/ja054297i.

[43] L. S. Bartell. "Tolman's δ, Surface Curvature, Compressibility Effects, and the Free Energy of Drops". In: *The Journal of Physical Chemistry B* 105.47 (2001), pp. 11615–11618. DOI: 10.1021/jp011028f. eprint: https://doi.org/10.1021/jp011028f. URL: https://doi.org/10.1021/jp011028f.

[44] E. M. Blokhuis and J. Kuipers. "Thermodynamic expressions for the Tolman length". In: *The Journal of Chemical Physics* 124.7 (2006), p. 074701. DOI: 10.1063/1.2167642. eprint: https://doi.org/10.1063/1.2167642. URL: https://doi.org/10.1063/1.2167642.

[45] S. W. Mayer. "A molecular parameter relationship between surface tension and liquid compressibility". In: *The Journal of Physical Chemistry* 67.10 (1963), pp. 2160–2164. DOI: 10.1021/j100804a046. eprint: https://doi.org/10.1021/j100804a046. URL: https://doi.org/10.1021/j100804a046.

[46] W. Helfrich. "Elastic Properties of Lipid Bilayers: Theory and Possible Experiments". In: *Zeitschrift für Naturforschung C* 28.11-12 (1973), pp. 693–703. DOI: doi:10.1515/znc-1973-11-1209. URL: https://doi.org/10.1515/znc-1973-11-1209.

[47] S. Fisk and B. Widom. "Structure and Free Energy of the Interface between Fluid Phases in Equilibrium near the Critical Point". In: *The Journal of Chemical Physics* 50.8 (1969), pp. 3219–3227. DOI: 10.1063/1.1671544. eprint: https://doi.org/10.1063/1.1671544. URL: https://doi.org/10.1063/1.1671544.

[48] P. A. Egelstaff and B. Widom. "Liquid Surface Tension near the Triple Point". In: *The Journal of Chemical Physics* 53.7 (1970), pp. 2667–2669. DOI: 10.1063/1.1674388. eprint: https://doi.org/10.1063/1.1674388. URL: https://doi.org/10.1063/1.1674388.

[49] K. K. Mon and D. Stroud. "Surface widths of simple liquids and an empirical law of freezing". In: *The Journal of Chemical Physics* 74.3 (1981), pp. 2078–2080. DOI: 10.1063/1.441257. eprint: https://doi.org/10.1063/1.441257. URL: https://doi.org/10.1063/1.441257.

[50] M. Schmitt et al. "Self-bound droplets of a dilute magnetic quantum liquid". In: *Nature* 539.7628 (Nov. 2016), pp. 259–262. ISSN: 1476-4687. DOI: 10.1038/nature20126. URL: http://dx.doi.org/10.1038/nature20126.

[51] F. Ancilotto et al. "Density functional theory of doped superfluid liquid helium and nanodroplets". In: *International Reviews in Physical Chemistry* 36.4 (2017), pp. 621–707. DOI: 10.1080/0144235X.2017.1351672. URL: https://doi.org/10.1080/0144235X.2017.1351672.

[52] F. Ancilotto et al. "Vortex properties in the extended supersolid phase of dipolar Bose-Einstein condensates". In: *Phys. Rev. A* 103 (3 Mar. 2021), p. 033314. DOI: 10.1103/PhysRevA.103.033314. URL: https://link.aps.org/doi/10.1103/PhysRevA.103.033314.

[53] A. L Fetter and A. A. Svidzinsky. "Vortices in a trapped dilute Bose-Einstein condensate". In: *Journal of Physics: Condensed Matter* 13.12 (Mar. 2001), R135–R194. ISSN: 1361-648X. DOI: 10.1088/0953-8984/13/12/201. URL: http://dx.doi.org/10.1088/0953-8984/13/12/201.

[54] M. Pi et al. "Coexistence of vortex arrays and surface capillary waves in spinning prolate superfluid He-4 nanodroplets". In: (2021). arXiv: 2104.06712 [cond-mat.mes-hall].

[55] Julien G., Jin D., and Antti J. N. "Timecrystalline vorticity and anyonic exchange in a cold atom Bose-Einstein condensate". In: (2021). arXiv: 2010.04549 [cond-mat.quant-gas].

[56] G. B. Hess. "Angular Momentum of Superfluid Helium in a Rotating Cylinder". In: *Phys. Rev.* 161 (1 Sept. 1967), pp. 189–193. DOI: 10.1103/PhysRev.161.189. URL: https://link.aps.org/doi/10.1103/PhysRev.161.189.

[57] Y. V. Kartashov et al. "Three-dimensional droplets of swirling superfluids". In: *Physical Review A* 98.1 (2018), p. 013612.

[58] V. Cikojević, L. Vranješ Markić, and J. Boronat. "Finite-range effects in ultradilute quantum drops". In: *New Journal of Physics* 22.5 (May 2020), p. 053045. DOI: 10.1088/1367-2630/ab867a. URL: https://doi.org/10.1088/1367-2630/ab867a.

[59] A. Ralston and H. S. Wilf. *Mathematical Methods for Digital Computers*. Wiley, New York, 1960.